An integrative framework for computational modelling of cardiac electromechanics in the mouse

Sander Land

Wolfson College
University of Oxford

Supervised by Professor Nic Smith

A thesis submitted in fulfilment of the requirements for the degree of Doctor of Philosophy

2013

Abstract

An integrative framework for computational modelling of cardiac electromechanics in the mouse

Sander Land, Wolfson College

This thesis describes the development of a framework for computational modelling of electromechanics in the mouse, with the purpose of being able to integrate cellular and tissue scale observations in the mouse and investigate physiological hypotheses. Specifically, the framework is applied to interpret electromechanical coupling mechanisms and the progression of heart failure in genetically modified mice.

Chapter 1 introduces the field of computational biology and provides context for the topics to be investigated.

Chapter 2 reviews the biological background and mathematical bases for electromechanical models, as well as their limitations.

In Chapter 3, a set of efficient computational methods for coupled cardiac electromechanics was developed. Among these are a modified Newton method combined with a solution predictor which achieves a 98% reduction in computational time for mechanics problems.

In Chapter 4, this computational framework is extended to a multiscale electromechanical model of the mouse. This electromechanical model includes our novel cardiac cellular contraction model for mice, which is able to reproduce murine contraction dynamics at body temperature and high pacing frequencies, and provides a novel explanation for the biphasic force-calcium relation seen in cardiac myocytes. Furthermore, our electromechanical model of the left ventricle of the mouse makes novel predictions on the importance of strong velocity-dependent coupling mechanisms in generating a plateau phase of ventricular pressure transients during ejection.

In Chapter 5, the framework was applied to investigate the progression of heart failure in genetically modified 'Serca2 knockout' mice, which have a major disruption in mechanisms governing calcium regulation in cardiac myocytes. Our modelling framework was instrumental in showing for the first time the incompatibility between previously measured cellular calcium transients and ventricular ejection. We were then able to integrate new experimental data collected in response to these observations to show the importance of β-adrenergic stimulation in the progression of heart failure in these knockout mice.

Chapter 6 presents the conclusions and discusses possibilities for future work.

Acknowledgements

This work would not have been possible without the support and collaboration of many.

Firstly, I would like to thank our experimental collaborators Bill Louch, Magnus Aronsen, Emil Espe, Ivar Sjaastad and Ole Sejersted in Oslo for providing most of the experimental data. Their trust in sharing their data, willingness to do additional experiments on the basis of model results, and clear communication throughout our collaboration were key in obtaining the results described in this thesis.

Funding for this research was provided by a studentship from the Medical Research Council, with additional support from Wolfson College and the department of Computer Science at Oxford and the department of Biomedical Engineering at King's College London.

I would also like to thank my colleagues at both Oxford and King's College London for their collaboration, and in particular to Jiahe Xi for close collaboration during the early phase of this research, Pablo Lamata for generating the computational meshes, and Liren Li for assistance in using her cell models. The combination of support from friends at Wolfson College as well as from my family did much to alleviate the stress of research during the past three years. In het bijzonder dank aan opa Piet en oma Jannie voor de talloze ansichtkaarten, and thanks to Grace for proofreading this thesis and her continued support during the process of writing it.

Most importantly, I owe much to my supervisor Nic Smith. His positive way of providing frequent critical feedback, while allowing me the freedom to explore ideas, was instrumental in shaping me as an academic. Steven Niederer was a co-supervisor in all but name during this process. Both his perspective on academic issues and in-depth practical knowledge of electromechanical modelling were very helpful in completing this work, and I look forward to our continued collaboration.

Contents

Chapter 1

Introduction

Heart disease continues to be a major concern as a leading cause of death in the western world. In general, heart failure is defined as the the heart having insufficient pump function to distribute blood flow and meet the circulation needs of the body. This mechanical pump function is derived from the synchronous contraction of many cardiac cells, regulated by a variety of feedback and control mechanisms.

There are many ways by which the disruption of normal cellular function and tension generation can cause heart failure. For example, in healthy hearts, mechanical deformation of the heart influences cellular function. As blood fills the heart chamber and muscle cells are stretched, these cells generate more force to produce a more powerful contraction. This feedback is key in ensuring the heart's contractile capacity matches the inflow of blood, and disruption of these mechanisms can have serious consequences.

Another potential cause of heart failure is dysregulation of the sympathetic nervous system of the heart. The 'β-adrenergic' response increases both the force generated by heart cells as well as the heart rate, and is adaptive in situations of injury with blood loss. However, continuous low blood pressure can also trigger this response, leading to chronic hypertension. Thus, this response can exacerbate heart failure and is therefore commonly prevented by the use of β-blockers (Frishman and Saunders, 2011).

Thirdly, calcium signalling is a key component of muscle contraction, as it connects the electrical and mechanical response of heart cells. This makes diseases which affect calcium dynamics another potential cause of heart failure. For example, failure of the intracellular calcium concentration to decrease quickly enough can lead to the heart failing to relax, resulting in diastolic heart failure.

Despite the importance of these cellular processes involved in cardiac contraction, many aspects of their molecular and genetic mechanisms are still poorly understood. Whereas the basic steps by which an increase in intracellular calcium concentration initiates contraction have been known for some time, many important aspects remain controversial. These include the steep relation between calcium and force (Sun and Irving, 2010), how crossbridges in muscle cells move to generate force (Huxley, 2000), and the length- and velocity dependencies of tension generation (Campbell, 2011).

These complex subcellular mechanisms which determine the behaviour of the heart

are increasingly being investigated in experimental models which exploit the opportunities provided by genetic manipulation (Andersson et al., 2009b; Lee et al., 2010). The mouse is the most commonly used species in such research; hundreds of inbred or genetically engineered strains have been specifically developed to elucidate aspects of biochemistry and physiology across a range of functions in both normal and disease models (Skarnes et al., 2011).

Mathematical and computational models are also increasingly used to investigate complex biological systems. These techniques aid in the move towards more quantitative, consistent models in biology, enable *in-silico* experiments that are either too expensive or unethical, and can provide detailed information about the internal dynamics of biological systems that otherwise may be difficult to measure. Motivated by an insufficient understanding of cardiac biology and the causes of heart failure, models of the heart have become one of the most researched areas in computational biology, and have been an important part in building our understanding of cardiac electrophysiology (Noble and Rudy, 2001). More recently this field has further expanded from its initial focus, and now includes models of various aspects of heart function including the electrical and mechanical activity of both cardiac myocytes and myocardium, and blood flow to and from the heart (Smith et al., 2004). Multi-physics models, in which several of these aspects are coupled together, are increasingly being used to investigate the interactions between these functions (Nordsletten et al., 2011). Within this class, electromechanical models are among the more complex examples, in which the coupling between the electrical and mechanical activity of the heart, at both the cellular and tissue level, is included.

However, even though electromechanical models have been used to investigate the mechanisms of cardiac contraction in a variety of animals (Niederer and Smith, 2009; Kerckhoffs et al., 2010; Keldermann et al., 2010; Campbell et al., 2008b), a model of a mouse heart with the ability to incorporate and interpret the growing amount of experimental data from mice does not yet exist. Furthermore, existing electrophysiological and contraction models are often based on data obtained across a range of species and temperatures. These heterogeneous sources of data underpinning the parameter sets of many electromechanical models creates significant limitations in the move towards the application of models in both wet-lab and clinical settings (Niederer et al., 2009a). The lack of species and body temperature consistent models is indicative of challenges in identifying model parameters from only cell measurement data. This difficulty is in part due to the fact that experimental preparations and measurements are often focused on proving the existence of particular mechanisms, rather than quantifying their exact magnitude as needed for parametrizing a computational model. An electromechanical model of the mouse thus provides an important opportunity in moving beyond these limitations, integrating data which is increasingly becoming available in both normal and transgenic animals, and using it towards a better quantitative understanding of cardiac function, both specifically in this common experimental model, and ultimately in other species.

Previous work in this area has already made progress in this area by developing data-driven electrophysiology models of murine cardiomyocytes (Li et al., 2011, 2012). These

models were driven by research in a strain of genetic knockout mice, in which the function of the SERCA pump, an important part of calcium regulation in cardiac cells, was impaired (Andersson et al., 2009b). These mice developed moderate heart failure over several weeks. However, they did stay healthier than was initially expected from such a severe disruption of cellular function (Andersson et al., 2009a; Louch et al., 2010). Further analysis revealed several mechanisms by which other parts of the cell compensate for the loss of SERCA function (Li et al., 2012; Louch et al., 2010; Swift et al., 2012). However, it was still not clear whether these mechanisms are sufficient to maintain cardiac function, as calcium dynamics remain severely impaired. Furthermore, as of yet no quantitative link has been made between data collected in isolated cardiac cells from these mice, and the decrease in heart function observed in vivo over several weeks.

This thesis describes the development of an electromechanical model for the mouse heart, and its use in investigating the progression of heart failure in this strain of genetic knockout mice. This allows us to connect models and experiments at the cellular scale with the whole-organ function measured, and better explain the progression of heart failure in these animals.

The thesis is organized as follows: Chapter 2 expands on the necessary background in cardiac biology and the mathematical modelling, and reviews the previous work done in electromechanical modelling. Chapter 3 describes our computational framework and implementation on which the rest of the work is based. In Chapter 4 we describe both a novel contraction model developed to represent the function of mouse cardiac muscle cells at physiological temperatures and pacing rates, as well as the extension of this to an electromechanical model and investigation of electromechanical coupling mechanisms. Finally, in Chapter 5, we apply this model to investigate heart failure progression in Serca2 knockout mice, and explain the observations previously made in these mice. Chapter 6 summarizes the conclusions and discusses opportunities for future work.

Chapter 2

Background

Cardiac electromechanics integrates work from several extensively developed fields. These include research into the biology, modelling and computational methods of cardiac electrophysiology and mechanics at both the cellular and tissue level. This chapter aims to provide the necessary background information and references to place the work described in this thesis in context, Some of the topics will be dealt with only briefly; the main focus will be those most relevant to electromechanics research. Furthermore, this chapter deals only with biology and mathematical modelling, leaving computational methods for the following chapter. The chapter is organized as follows: after a brief introduction to cardiac anatomy and cardiac cellular biology, we discuss several important concepts for cardiac modelling in general, that have particular relevance to the work outlined in this thesis. Next, section 2.3 explains the continuum modelling of tissue-level electrical and mechanical properties. Finally, we give an overview of electromechanics, which combines electrophysiology and contraction at both cellular and tissue scales.

2.1 Cardiac anatomy

The heart is responsible for continuously pumping blood to the lungs and rest of the body. The organ consists of two atria which receive blood, and two ventricles which pump it back to the rest of the body, as shown in Figure 2.1. Whereas the right ventricle only pumps blood from the heart to the lungs, the left ventricle is responsible for blood flow to the rest of the body, making it a primary focus for disease research and modelling.

The pump function of the left ventricle ventricle can be divided into phases, depending on which of its two valves are open. In diastole the ventricle is filled with blood, starting with rapid filling after the mitral valve opens, slowing down, and ending with another period of rapid filling as the atrium contracts. After the mitral valve closes, the fact that both valves are closed keeps volume constant, leading to the isovolumetric contraction phase. In this phase pressure rises rapidly to exceed the aortic pressure, which opens the aortic valve and starts ejection. At the end of ejection, both valves are once again closed, leading to isovolumetric relaxation. This phase ends when the pressure in the atrium

exceeds that of the ventricle, which opens the mitral valve, starting diastole once again.

Rapid electrical activation ensures the heart contracts synchronously. Electrical activation starts at the sinoatrial node, initiated by pacemaker cells which spontaneously activate. The atria are activated first, and electrical activation proceeds via the atrioventricular node, as the valve plane separating the atria from the ventricles is non-conductive. The specialized conduction system, which ends on a large portion of the endocardial surface, ensures synchronous activation of the ventricles.

For more details on cardiac physiology, see the standard textbooks by Katz (2005) and Opie (2003).

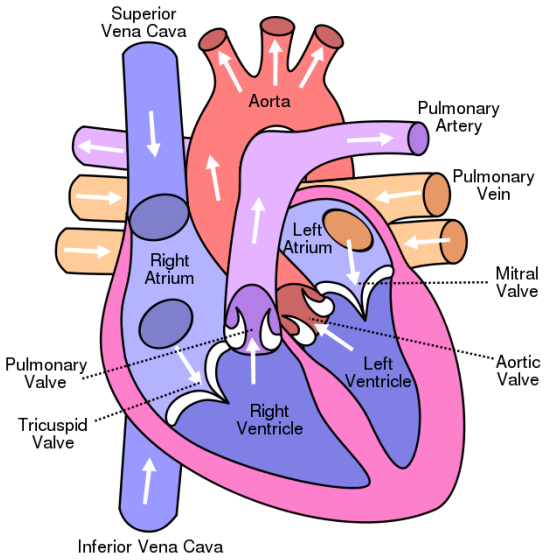

Figure 2.1: Schematic illustration of human cardiac anatomy. (See Appendix C for source)

2.2 Cellular biology and modelling

The heart consists predominantly of cardiac *myocytes*, the muscle cells that generate force. These cardiac cells are roughly cylindrical, about 100 µm long and $10 - 20$ µm in diameter. Underlying the mechanical activity of these cells is the regular electrical activation, which both regulates the calcium necessary for initiating contraction and is responsible for the spread of activation throughout tissue. Due to the complexity of both the electrical and mechanical activity of the cell, computational modelling studies have tended to parallel experimental studies by focusing primarily on one of these aspects. The sections below reflect this by discussing both the biology and modelling of electrophysiology and contraction separately.

2.2.1 Electrophysiology

At the basis of the efficient mechanical activity of the heart, is the fast and synchronous electrical activation of cardiac cells. This electrical activity is driven by ion channels, exchangers, and pumps present in cardiac cells, which allow ions to cross the membrane and generate an *action potential*. A cardiac cell at rest has a large transmembrane potential of -80 to −90 mV. When the cell is stimulated and reaches a threshold potential of around −40 mV, an action potential is generated. Example action potentials for human ventricular cells are shown in Figure 2.2. The upstroke which causes the fast electrical activation of a cell, is driven by the fast inward sodium current. At the resulting higher transmembrane potential, L-type calcium channels open and calcium ions enter the cell, causing a clear plateau phase in human cells. The resulting local increase in calcium ions near the membrane activates a process known as calcium-induced calcium release (CICR). During this process a large amount of calcium is released from the intracellular calcium store, the sarcoplasmic reticulum (SR), by means of the ryanodine receptors. At the end of the cardiac cycle, calcium is pumped back into the SR by the SERCA2 pump*. As the SR release and SERCA uptake are the primary source of variation in intracellular calcium (Bers, 2000), and this transient drives the contraction of the cell, SERCA is a crucial component in the cardiac cell, and reduced SERCA function can lead to serious illness associated with contraction and heart failure (Kranias and Bers, 2007). Figure 2.3 shows a schematic of the these calcium fluxes in the cell.

Repolarization back to the resting membrane potential is driven mainly by potassium currents. There are also several ion exchangers and pumps which restore concentrations back to their original levels, most notably the sodium-calcium exchanger (NCX), the sodium-potassium pump (Na^+/K^+-ATPase), and an ATP-driven calcium pump (PMCA, plasma membrane Ca^{2+}ATPase).

2.2.2 Electrophysiological models

Electrophysiological models represent the electrical activation and calcium dynamics in the cell described in the previous section in a mathematically precise way.

The field of electrophysiological modelling can be traced back to Hodgkin and Huxley's original model of the giant squid axon (Hodgkin and Huxley, 1952), which resulted in a Nobel Prize in Physiology or Medicine. The first solutions to this early model were calculated over three weeks using a mechanical calculator (Schwiening, 2012). This computation was necessary, as due to the complexity of biological models that represent parts of a cell, they rarely have analytical solutions. Thus, it is no coincidence that the rise in popularity and complexity of cardiac models has tracked the increase in available computer technology. Mathematical and computational models inspired by the Hodgkin and Huxley model played an important part in the investigation of cardiac cellular electrophysiology. By integrating experimental observations in a mathematical model, both emergent results

*SERCA2, sarco/endoplasmic reticulum Ca^{2+}-ATPase 2

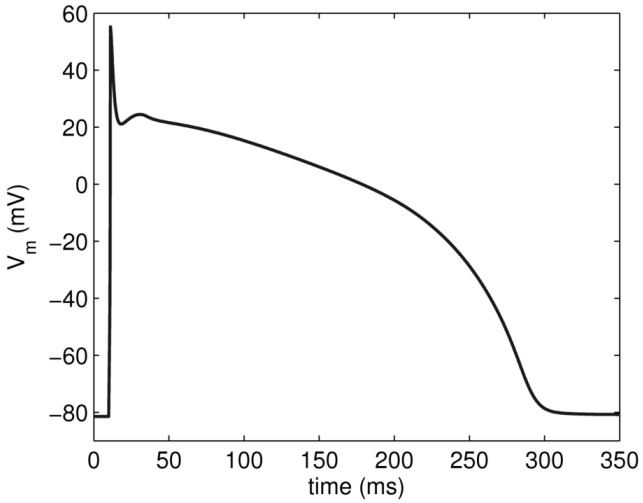

Figure 2.2: Action potentials for human ventricular myocytes. From the model by Grandi et al. (2010)

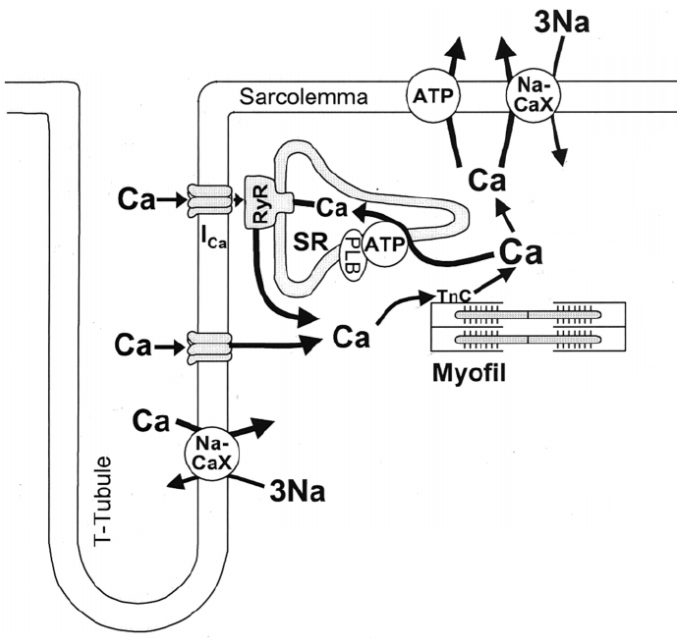

Figure 2.3: Calcium fluxes in the cell. This schematic shows is a single T-Tubule, a deep invagination in the cell membrane contains the L-type calcium channels. Calcium enters the cell through these, activates the ryanodine receptors (RyR), causing SR calcium release. Intracellular calcium then activates the contractile proteins ('TnC', 'Myofil', both described later), and is eventually removed by NCX ('NaCaX'), PMCA ('ATP' pump on the cell membrane), and SERCA (indicated by the ATP pump on the SR). Figure reproduced from with permission from "D. Bers. Calcium Fluxes Involved in Control of Cardiac Myocyte Contraction. Circ. Res. 2000;87;p276" (Bers, 2000)

and remaining differences in predictions can inform novel experiments, leading to iterative improvements of both mathematical models and experimental results (Noble and Rudy, 2001).

Noble (1962) modified the Hodgkin-Huxley model to reproduce the action potentials of Purkinje cells. As the calcium current had not yet been discovered, the sodium current was modified to account for all inward fluxes. Similarly, the early contraction model of Huxley (1957) was created before the discovery of the calcium current, and proposes that the membrane potential directly influences contraction. Both of these models were incomplete, yet contributed greatly by generating new testable hypotheses. After the invention of patch-clamping techniques, the L-type calcium current was quickly discovered, and integrated into newer generations of mathematical models. The availability of this experimental data enabled modellers to create an accurate representation of the most important currents led to the model of Beeler and Reuter (1977) for the ventricular action potential. Further advances in understanding the function of pumps and exchangers in the cell to maintain the gradient in ion concentrations resulted in the model of DiFrancesco and Noble (1985), which included the Na-K pump and Na-Ca exchanger, and modelled intracellular events such as calcium release from the sarcoplasmic reticulum. Additional improvements in experimental techniques in the 90's provided data for the Luo-Rudy models for mammalian action potentials (Luo and Rudy, 1991, 1994a,b), which are still the basis for many more recent models. A more detailed history of key developments of electrophysiological models over the last 60 years is given in the recent overview by Noble et al. (2012). The increase in computational power over the past 60 years has also made it possible to investigate the emergent effect of cardiac cellular properties on whole-organ behaviour using multiscale models, which will be described later in this chapter.

Although there are also phenomenological electrophysiological models which capture action potential morphology without any detailed model of ion channels (Bueno-Orovio et al., 2008; Fenton and Karma, 1998), these do not include the calcium dynamics necessary for biophysically based coupling to a contraction model, and are therefore less useful for electromechanical simulations in this thesis.

In the last two decades, a large number of detailed cardiac models have been published which include the detailed calcium dynamics, including models for guinea pig (Noble et al., 1998), mouse (Bondarenko et al., 2004; Li et al., 2010, 2011, 2012) human (Iyer et al., 2004; Grandi et al., 2010; O'Hara et al., 2011) and many others. However, there are still large differences in model parameters between similar electrophysiology models representing the same species, as well as a large range of species and temperatures for the sources of experimental data (Niederer et al., 2009a).

2.2.3 Mathematical and computational models

Electromechanical models of the heart integrate several different kinds of mathematical models components within a single heart modelling framework. Among these, models of the cellular electrophysiology have a rich history, as briefly reviewed in the previous section. In this section, we use this historical context to introduce several important concepts in

the field of mathematical modelling in general, which will be important in the rest of this thesis.

The first concept we cover is the rationale of using mathematical and computational models in biology. Mathematical models are a very explicit and quantitative way to represent biological knowledge. Aside from merely representing such biological mechanisms, they can also be used as tools that can be used to investigate or suggest specific hypotheses. Initial model hypotheses are often focussed on investigating basic consistency between different experimental measurements. The ability of a model to replicate emergent behaviour of a system from more basic measurements provides evidence for a degree of completeness in our conceptual understanding. An example of this is the reproduction of action potentials from measuring and modelling ion channel properties, such as in the pioneering work by Hodgkin and Huxley (1952). Electrophysiology models can also be used to gain better understanding of a complex physical system, where the role of the different components on the emergent behaviour of the whole may not be immediately obvious, or be used to perform experiments by perturbing the system in ways that are too expensive and/or unethical. Recent examples from electrophysiology modelling which use models to test more advanced hypotheses or make predictions of cardiac function include assessing the effect of blocking ion channels on changes in action potential morphology and risk of side-effects from drugs (Mirams et al., 2011) and investigating the cause of atrial arrhythmias in patients (McDowell et al., 2012).

The second concept is that of model limitations. All mathematical models are necessarily simplified, as their purpose is partly to function as a more understandable version of reality. Thus, despite the advances outlined above, this remains especially true of mathematical models of biological systems such as a cell, as these models represent a large number of closely interacting proteins, with both significant complexity and uncertainty in their interactions. As a result of both limited measurements and knowledge of a system to be modelled, as well as conscious choices to omit or simplify specific components, models are limited in what physiological questions they can be used to investigate. The limitations of a model can be in part derived from the choices made in simplifying, and from knowledge on the effect of simplifications.

Firstly, limiting the complexity of a model leads to hypotheses that clearly can not be tested using the model. For example, models of cardiac cellular electrophysiology generally do not include a model of the contractile function of the cell, and often abstract this component as nothing more than a calcium buffer. This makes them unsuitable for testing a variety of hypotheses, including those related to understanding mechanical influence on the electrophysiology. Secondly, the accuracy of the model can be affected by the simplifications. As in the previous example, even when the amount of force generated by a cell is not directly relevant to the hypothesis under investigation using an electrophysiological cell model, the force generated has some influence on calcium dynamics. Thus, omitting this component limits model accuracy. Similarly, many regulatory pathways in the cell including those related to metabolism, the influence of the nervous system on cardiac cells, and gene transcription are usually not included in models of cardiac electrophysiology. All

of these omissions are likely to affect the accuracy of models in minor ways, and limit the ways the models can be applied to study more extreme perturbations of their environment. The effects of modelling choices on the accuracy of model predictions tend to be discovered as the field progresses and different choices are investigated. Model limitations become apparent as they fail to match existing or new experimental measurements, or when different models of the same system make significantly different predictions. Although some of them are likely known in the model development process, such as those resulting from choices between complexity and accuracy, the impact of other model limitations can go undiscovered for years. For example, in the model by Noble (1962), the lack of a calcium current makes the model unable to replicate action potentials without large changes in the behaviour of the sodium current. This created several potential hypotheses for the mechanisms underlying the action potential of Purkinje cells: either there are large differences in the properties of neural and cardiac sodium channels, or there are other inward currents which cause the plateau phase. Although we now know that the second of these hypotheses is correct, at the time the extent of the model's limitations were unknown. From this example we can also see that even severely limited models can be useful, as by integrating and quantifying biological knowledge, they can reveal gaps in our understanding and inspire further experiments.

This overview shows that there are major challenges in choosing what model components and level of detail to include or exclude from an electromechanical model of the heart, which includes models of the electrical and mechanical activity at both the cellular and tissue level. Section 2.2.5 below describes our approach to balancing model complexity and model limitations.

2.2.4 Animal models

As we have seen in the section describing the history of electrophysiological models, there are a variety of animal species that have been represented using models. Mathematical model development tends to follow experimental developments, and as the availability of healthy human tissue and cells for experiments is extremely limited, a variety of animals models has been used in investigations of cardiac biology. Similarly to the mathematical models described in the previous section, this practice comes with a number of limitations, and the impact of these depends on both the animal used, and the hypotheses under investigation.

Larger animals such as pigs, sheep, and dogs are generally though to be more similar to humans, but are expensive to breed and maintain. Smaller animals such as rats, mice, ferrets and guinea pigs are easier to maintain Mice and rats are especially popular in biological research due to their small size and short gestation period. Monkeys and apes are the only mammals closely related to humans but are rarely used in cardiac biology experiments. Most other mammals are far more distantly related, sharing a common ancestor over 80 million years ago (Springer et al., 2011). This creates a complex relationship between animal size and similarity to humans. Some animals have become standard experimental models in different fields, depending on their suitability, cost, and

historical factors. Guinea pigs have action potentials more similar to larger mammals, due to their similar levels of expression of the potassium channels (Noble et al., 1991), which has made them a popular target for experiments and modelling cardiac electrophysiology. Other examples of popular animal models are the use of rodents in ageing research (Foster et al., 2012), zebrafish in developmental biology (Mayden et al., 2007), and rabbits in investigating ventricular arrhythmias (Panfilov, 2006).

In the past decade, mouse models have become increasingly common, due to the relative ease of genetic manipulation in these animals: it was the first mammal to have its genome sequenced (Waterston et al., 2002), and for some time the only species in which germline transmission was possible (Mullins and Mullins, 1996). This has led to significantly more mouse data being available, both from healthy control as well as disease models. The increasing use of mice has resulted in extensive knowledge of their limitations for understanding human biology and disease, as well as further development of technology to overcome them. For example, although the small heart size limits some of the measurements that can be performed in these animals, the rise of smaller devices such as miniature catheters over the last decade makes these experimental measurements less problematic. However, the small heart size can still limit studies of regional biochemical and physiological analysis (Walsh, 2001).

At first sight the mouse heart appear appears to a scaled model of a human heart in many aspects (Tranquillo and Sunkara, 2007), with similar fiber organization and conduction velocity, and calcium and ventricular pressure transients are very similar to humans after adjusting for a heart rate that is approximately 10 times higher. However, the differences in underlying gene expression between mice and human can be substantially larger (Mullins and Mullins, 1996). With respect to electrophysiological function, there are large differences between the action potentials of rats and mice, compared to humans, as can be seen in detail in Figure 2.4. Although most ion channels are conserved across species, there are significant differences in the potassium currents involved in repolarization between mouse and human ventricular myocytes (Nerbonne, 2004). Specifically, although the upstroke is similar in both species, the repolarization phase shows clear differences even after taking into account the disparity in heart rates. In humans, the upstroke is followed by transient repolarization and a plateau phase, whereas in mice no plateau is visible and repolarization is rapid. Regardless of theses larger differences in ion channel expression, more electrophysiological studies are being done in mice, often with transgenic changes to potassium channels. Interpreting these results requires detailed knowledge of the limitations of the mouse as a model animal to infer the applicability of any results to humans and other animals (Nerbonne, 2004).

Contraction dynamics appear more similar between humans and mice, giving rise to the aforementioned similarities in pressure transients. However, there are also some notable differences, such as the dependence on heart rate of the force generated by cardiac cells (force-frequency relationship), which is less pronounced in mice and rats compared to larger mammals (Janssen, 2010). Furthermore, there are differences in myosin isoform expression, with mice expressing mostly α myosin heavy chain, and humans mostly β

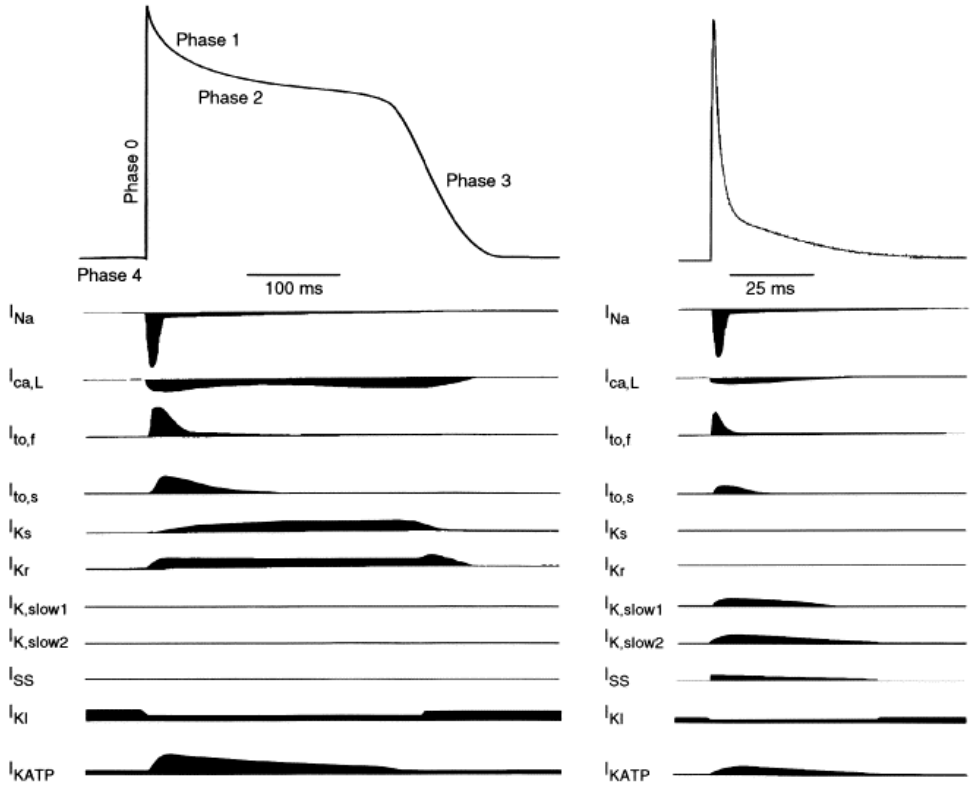

Figure 2.4: Ventricular action potentials for human and mouse. Human action potential and currents shown on the left, and mouse action potential and currents shown on the right. Details of ion channel currents making up the action potential and their respective timing. (See Appendix C for source.)

myosin heavy chain. This can be especially relevant when investigating disease phenotypes related to changes in these isoforms, such as changes in the ratio of myosin heavy chain isoforms induced by hypertrophy (Walsh, 2001). Another example especially relevant to this thesis is that although the calcium transients of humans and mice are similar after adjusting for differences in heart rate, mice rely more on intracellular calcium cycling through SR release and SERCA uptake. Thus, perturbations to calcium regulation using a genetic knockout in the mouse is likely to have different quantitative effects compared to similar changes in humans.

From this overview it is clear that there are significant limitations to using the mouse as a model for human disease in biological research. Nevertheless, the use of the mouse as an experimental animal has been very successful over the past decade, and the mouse is likely to remain popular as an animal model, which has motivated the topic of this thesis.

2.2.5 Our approach

This section describes our approach to modelling and interpreting animal data in light of the issues presented in the last two sections.

With respect to model complexity and limitations, our choices are driven by a combination of the available data to characterize specific model components and the hypotheses that we wish to test. To provide a specific example relevant to this thesis, we model only the left ventricle, even though the heart consists of four chambers, is connected to the circulatory system, receives input from the nervous system and interacts with the chest cavity. This is likely to have some effect on the predictions our model makes, as mechanical interaction between the left ventricle and the atria, right ventricle, and the chest cavity are likely to have some influence on pump function. This choice is in part driven by our available data, which consists of measurements of pressure, volume, and geometry of the left ventricle. Furthermore, the hypotheses we wish to test relate to reproducing such characteristics of the left ventricle, which is the primary focus of disease research. We also model the cells in the ventricle as behaving similarly throughout the tissue, even though there is evidence of some spatial variation in the behaviour of cells (Dilly et al., 2006; Bondarenko et al., 2004). Again, the existing electrophysiology models and the data they are based on, as well as later measurements of cellular properties do not include this level of detail, and our hypotheses are generally related to the bulk properties of the myocardium. The choices made throughout building an electromechanical model of the heart can influence the accuracy of our predictions. Thus, we discuss the potential limitations that result from our modelling choices in more detail at the end of Chapters 4 and 5.

Lack of accurate knowledge of model parameters can also be investigated using a parameter sensitivity study. By varying model parameters and observing the effects on simulation results, the impact of uncertainty on simulation results can be estimated. We use this technique extensively in Chapter 4 to determine the most influential parameters in both our cellular and whole-organ model of the mouse.

With respect to the limitations of animal models, our main goal in this thesis is to

develop a model of the mouse primarily for understanding murine physiology and biology. We discuss the potential applicability of our results to other species only briefly in the relevant discussion sections.

In this thesis there is no major electrophysiological model development, as we used published models with only occasional minor changes. However, it is important to note that we do use recent models which have been developed with both parametrizability and species- and temperature consistency in mind. Furthermore, we discuss potential limitations of the models we use, especially when they have not been previously described.

The most important novel cellular model development will be presented in Chapter 4, in the form of a model of cellular contraction. This field comes with relatively more uncertainty than models of electrophysiology, especially with respect to the influence of mechanical deformation on the tension generated by cells. The next sections describe the biological background, mathematical modelling and these controversies in detail.

2.2.6 Cellular contraction

Cardiac muscle cells are striated: organized into many contractile sub-units called *sarcomeres*, each approximately 2 μm long. As shown in Figure 2.5, each of these units consists of thin and thick filaments. The thick filaments contain myosin crossbridges which bind to the thin 'actin' filament to generate force.

This process is started by electrical activation and the resulting increase in cytosolic calcium. Calcium binding to the regulatory calcium binding site on troponin C* then starts the contractile activation process.

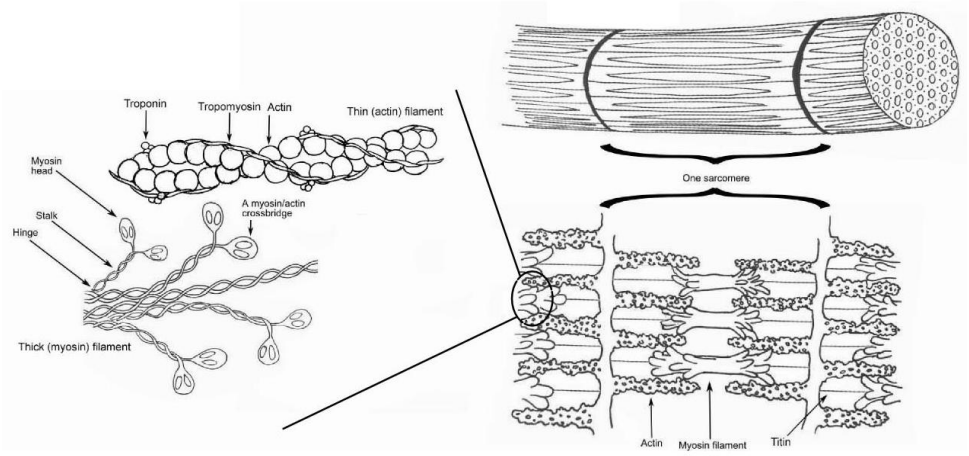

Figure 2.5: Schematic of a sarcomere. Cardiac muscle is striated, consisting of many sarcomeres. Each sarcomere contains actin and myosin filaments, which generate tension. (See Appendix C for source)

Within the sarcomeres, binding of calcium to troponin C causes a conformational change in its associated tropomyosin complex, unblocking the actin sites for myosin cross-

*often abbreviated TnC and denoted by TnC or TRPN in equations

bridge cycling. Tension is generated by the combined effect of many crossbridges, each generating a force of a few piconewton. The action of crossbridges is often described in terms of a cycle, shown in figure Figure 2.6. In this cycle, a myosin crossbridge on the thick filament repeatedly attaches to the actin thin filament, performs a power stroke to generate force, and then detaches using ATP (Geeves and Holmes, 2005). Some detailed measurements of crossbridges suggests that crossbridges make multiple small steps during one ATP turnover event, and can move in a biased Brownian fashion along the thin filament (Marcucci and Yanagida, 2012; Takano et al., 2010; Yanagida et al., 2000). How exactly these components of Brownian motion and power stroke interact is still unknown, as are other aspects of contraction such as the amount of force generated by a single crossbridge (Huxley, 2000). However, evidence from other types of actin-myosin motors in the cell suggests that both components may interact to generate larger step sizes per cycle, with Brownian motion playing a role in the weakly bound state (Spudich and Sivaramakrishnan, 2010).

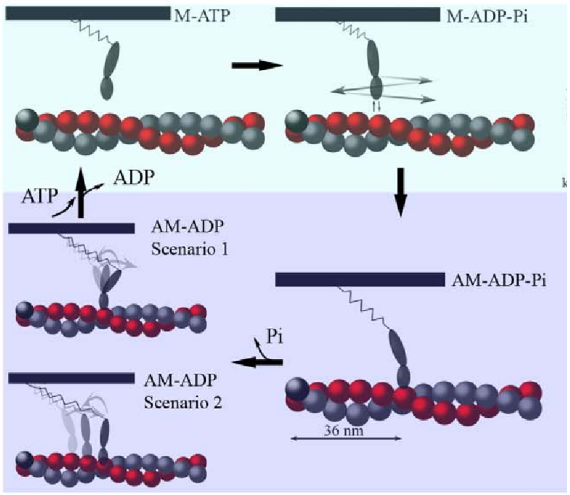

Figure 2.6: Crossbridge cycling models. Myosin crossbridges generate force using ATP in the Lymn-Taylor cycle. First, myosin-ATP is hydrolized to myosin-ADP-P_i. In this configuration, the complex finds a binding site on the actin filament to form actin-myosin-ADP-P_i, also known as the 'weakly bound state'. In the lever-arm model, crossbridges make relatively large forward steps after release of P_i to form the strongly bound state. In biased Brownian ratchet models, crossbridges make many small steps, some of which are backwards. In both cases, binding of ATP detaches myosin from actin, and restarts the cycle. (See Appendix C for source)

Another important aspect of force development are the nonlinearities in the response of force to calcium, or *cooperativity*. Peak calcium concentrations are generally 2-10 times the minimum levels, whereas peak tension can be over 50× resting levels. This cooperativity has been well known from measurements of the sigmoidal response of force to calcium in isolated myocytes. Figure 2.7 shows an example of this response from the literature, fitted using Hill curves:

$$F = \frac{[\mathrm{Ca}^{2+}]_\mathrm{i}^n}{[\mathrm{Ca}^{2+}]_{50}^n + [\mathrm{Ca}^{2+}]_\mathrm{i}^n}, \tag{2.1}$$

where n is the 'Hill coefficient', F is the force generated, $[Ca^{2+}]_i$ is the intracellular calcium concentration, and $[Ca^{2+}]_{50}$ is the calcium concentration at which the generated force is half-maximal. Such a curve can be derived from a basic model of n-stage cooperative binding (Keener and Sneyd, 1998). However, the response of cardiac muscle deviates consistently from a perfect Hill curve, with measurements below the best fitted curve, which indicated a biphasic response with a higher degree of cooperativity for lower calcium concentrations (Rice and de Tombe, 2004).

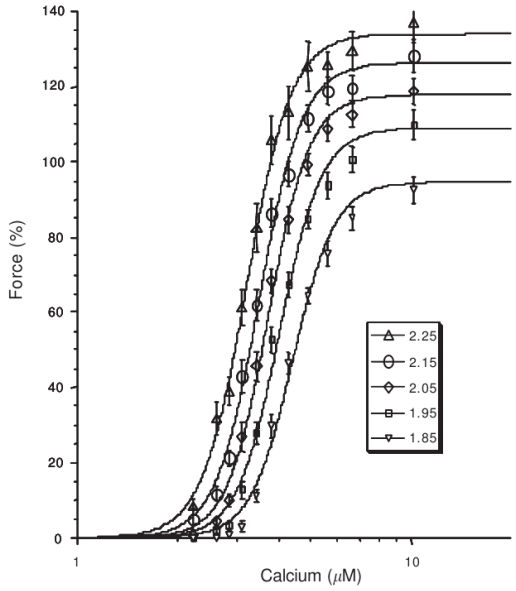

Figure 2.7: Force-Calcium relationship at different sarcomere lengths. At higher sarcomere length maximum force increases and the half-activation point shifts towards lower calcium concentrations. This figure also shows some of the changes induced in cells by experimental techniques, as most measurements of peak cytosolic calcium are $< 1\mu M$ in vivo, which would result in no tension generation. Figure reproduced from (Dobesh et al., 2002).

The biological mechanisms that result in the observed cooperativity are yet to be fully uncovered (Sun and Irving, 2010; Solaro, 2009). There is evidence that calcium binding to troponin C is cooperative within thin filaments, but not when isolated (Davis et al., 2007; Kreutziger et al., 2011). There is also evidence of end-to-end interactions of tropomyosin, allowing tropomyosin to shift to allow crossbridge binding without the need for TnC at all regulatory units (Tobacman, 2008; Rao et al., 2009). Finally, crossbridge binding has been implicated in several ways, including helping to bring filaments closer together, and keeping tropomyosin from blocking actin sites in the absence of TnC (Farman et al., 2010; Smith et al., 2009). A major difficulty in measuring these effects is the large effect of membrane permeabilization ('skinning') on measurements. This procedure makes it easy to vary the intracellular calcium concentration, but is also known to affect measurements of calcium sensitivity, Hill coefficient, and peak tension (Bers, 2002).

Overall, even though the basic steps and components of cardiac contraction have been known for some time, the details of how they interact to generate tension, and how they

are regulated, are far from agreed upon. For more on cardiac muscle contraction, see the books by Bers (2002) and Opie (2003), as well as recent reviews (Solaro, 2010; Stehle and Iorga, 2010).

2.2.7 Coupling mechanisms and mechanoelectric feedback

The process by which myocytes generate force was presented in the previous section as a simple chain of events only influenced by the calcium concentration. However, there are many other factors which can influence this process. Among these are the multiple feedback loops that enable tissue level mechanical deformation to influence both electrophysiology and tension generation at the cellular level. These feedback mechanisms include the strong influence that sarcomere length has on tension (Gordon et al., 1966), velocity dependent crossbridge kinetics (Daniels et al., 1984) and stretch-activated channels (Kohl and Sachs, 2001). As with cooperativity, both the details of the underlying mechanisms and the relative importance of each of these processes for whole-organ function is currently still poorly understood. The next sections describe some of these processes in more detail.

2.2.7.1 Length-dependence and the Frank-Starling mechanism

One of the most important feedback mechanisms is the influence of the muscle's length on the tension it generates. As cardiac muscle is stretched, it generates significantly more force.

At the whole organ level this response is known as the Frank-Starling law of the heart, named after pioneers Frank (1895) and Starling (1918) who performed experiments on isolated hearts. Their main observation was that the heart itself can regulate the force it generates to ensure outflow is balanced with inflow, without the need for external feedback. This mechanism by which force increases with blood volume, now known as the 'Frank-Starling mechanism', ensures that any difference between venous return and ejection is quickly corrected, before the heart is damaged or blood flow to the rest of the body is impaired.

For isolated cells this response is simply described as tension increasing with sarcomere length. Several potential mechanisms have been implicated in this length-dependent response of tension (Campbell, 2011). Firstly, the overlap fraction of thin and thick filaments changes with sarcomere length, which allows more crossbridges to bind (Gordon et al., 1966). However, this effect alone is much smaller than the observed length dependence in cardiac muscle (Allen and Kentish, 1985).

Another aspect of length dependence is the increased sensitivity of the muscle to calcium, known as length-dependent activation (LDA). In force-calcium measurements, the typical Hill curve shifts leftwards towards lower calcium concentrations, at greater sarcomere lengths, and maximum force increases. This shows that internal processes are more sensitive to either calcium or troponin C at higher sarcomere length, which is a major factor in the change of isometric tension and whole heart function. However, the suggested mechanisms for this 'length dependent activation' are controversial.

One of the suggested mechanisms is change in interfilament spacing: as muscle cells are stretched, the filaments are expected to become closer together, increasing the rate of crossbridge binding (Moss and Fitzsimons, 2002). Experiments have shown changes in length dependence properties when using osmotic compression techniques: inserting molecules of high molecular weight to change interfilament spacing independent of sarcomere length. However, more detailed studies that were able to distinguish effects of sarcomere length, muscle diameter, and interfilament spacing independently suggest that this mechanism is most likely not a major factor (Konhilas et al., 2002; de Tombe et al., 2010). More recent evidence from the de Tombe group analyzing their x-ray diffraction data from these studies suggests myosin head orientation as a dominant mechanism for LDA instead (Farman et al., 2011).

Length dependence can also be related to effects caused by tension, as the limited effect from sarcomere overlap could be enhanced by further feedback on tension generation or calcium to TnC binding. There is a significant effect of myosin binding on the unbinding rate of TnC to calcium under rigor conditions (Davis et al., 2007). However, this would result in significant differences in force-pCa curves when calcium is decreased compared to when calcium is increased, and such hysteresis is not observed in experiments (Rice et al., 2008b). Moreover, length dependence is unaltered in experiments where tension generation is prevented using blebbistatin (Farman et al., 2010). Conversely, similar experiments using sodium vanadate to inhibit force generation do show this mechanism as significant (Smith et al., 2009). Sun et al. (2009) suggest that there is a limited effect, but that this is not a major component and often not detectable to statistically significant levels.

The affinity of TnC for calcium was originally thought to change with sarcomere length, since length dependence changed when substituting cardiac TnC for skeletal TnC in skeletal muscle (Babu et al., 1988; Gulati et al., 1991). This mechanism is now considered unlikely as later measurements could not reproduce the results and showed no change in Hill coefficient (Fukuda et al., 2009; Moss et al., 1991). However, it is clear that troponin plays a key role in length dependence. (Terui et al., 2008) show that replacement of cardiac TnC with its skeletal counterpart changes the length dependence to be similar to skeletal muscle. This result is consistent with the observations of Farman et al. (2010), who show that replacement of cardiac TnC with a variant that does not bind Ca^{2+}, produces length-dependent changes in force-pCa relations. They suggest that LDA arises upstream of cross-bridge binding by length-dependent changes in Ca^{2+} cooperativity.

More recently, titin has been suggested as a main length sensor, with length-dependence being determined through passive force rather than length alone (Patel et al., 2012; Lee et al., 2010; Fukuda et al., 2009; Fukuda and Granzier, 2006; Cazorla et al., 2001). Titin may also be involved in changing interfilament spacing as well as influencing other myofilament properties.

Overall, although significant progress has been made in the past 20 years, the mechanisms that govern length dependence of cardiac muscle remain unclear. For more discussion on the length-dependence of cardiac muscle, see these recent reviews (Solaro, 2007; Hanft et al., 2008; de Tombe et al., 2010; Campbell, 2011).

2.2.7.2 Velocity dependence

Cardiac myocytes are also sensitive to the rate at which they are stretched, giving an immediate response to fast shortening or lengthening that counteracts the change in length. The force generated increases when lengthening the cell, and decreases during shortening.

Research in this area is sparse, making the biophysical mechanisms even more elusive than other aspects of muscle contraction. Much work in this area is related to the pioneering work by Hill (1938), who measured the heat released by skeletal muscle when shortening, and related it to the energetics of the muscle. This formula is still used as it provides a simple and accurate fit to force-velocity data. There is ongoing active research on the velocity-dependent properties of cardiac muscle with similar protocols, by using the unloaded shortening velocity as a main indicator. These experiments can give insight into dependencies such as sarcomere length and calcium concentration of this response (de Tombe and ter Keurs, 1992). However, for developing models of cardiac muscle more detailed data on the velocity-dependent response is often required. Kawai and Brandt (1980) have contributed to providing this by significantly improving the technique known as *sinusoidal analysis* . In this method, the properties of muscle are analyzed by by inducing a sinusoidal stretch, which leads to a sinusoidal change in force generated by the cell. The shift in phase and amplitude then provides information about the cell's biophysical properties. Specifically, for cardiac muscle the result is fitted to the function (Kawai et al., 1993):

$$y(f) = H - \frac{Bif}{b+if} + \frac{Cif}{c+if} + \frac{Dif}{d+if} \tag{2.2}$$

In this equation, y is the ratio of stress change to strain change, expressed in the frequency domain. Where H derives from passive tension, the 'C process' is the main short-term effect, a quick stretch will generate force opposing it. The 'B process' is a slower effect, that causes the opposite reaction on a slightly longer time scale. The 'D process' is an even slower process, with controversial relevance in cardiac muscle (Campbell et al., 2001). For these processes, the uppercase symbols B, C, D represent their magnitude, and the lowercase symbols b, c, d their characteristic frequency.

More recent work using this technique uses (Palmer et al., 2007):

$$y(f) = \overbrace{A(2\pi i/f)^k}^{\text{passive term}} - \frac{Bif}{b+if} + \frac{Cif}{c+if} \tag{2.3}$$

Here, the 'D process' is dropped, and a more detailed fit to passive tension is used (Dickinson et al., 1997).

The response to sinusoidal perturbations and quick step changes in length are reasonably well characterized from experiments, but the cellular mechanisms remain poorly understood. In recent research Yadid and Landesberg (2010) show experimental evidence for the C process appearing as a result of a decrease in the transition of strongly bound to weakly bound crossbridges when a muscle lengthens. However, their model does not predict a 'B process'. This change in crossbridge transition rate only appears under lengthening, while when shortening the force per crossbridge decreases instead. (de Tombe and

ter Keurs, 1992). Mathematical modelling by Palmer et al. (2007) suggests the C process does not require any addition and appears naturally from crossbridge cycling. Furthermore this author explains the B process as a frequency-dependent *increase* in the myosin off-rate (Palmer, 2010).

Titin has also been implicated in the velocity-dependence, possibly functioning as a contractile reserve in a tension- and velocity-dependent manner (Nishikawa et al., 2012) or adding elastic recoil (Opitz et al., 2003).

2.2.8 Contraction models

Even though the heart's primary function is as a pump, models of contraction for cardiac cells are still far less developed than models of electrophysiology. A review by Rice and de Tombe (2004) gives an overview of contraction modelling and discusses some of the difficulties behind the slow development of contraction models. These are mainly related to the fact that downstream contractile elements are more difficult to measure, components of the contractile framework interact tightly and are difficult to study in isolation.

Since, as outlined above, there are significant controversies that exist over the basic mechanisms of contraction, there are still different conceptual models for most subsystems in muscle contraction, such as the different crossbridge models explained above. Research has often focussed on distinguishing between such conceptual models rather than precisely quantifying their details. Nevertheless, models have been an important part of investigating muscle contraction for a long time, going back to Hill's model of released heat, force, and velocity during contraction (Hill, 1938). A differential equation based model was developed by Huxley (1957), which is still the reference model for much research today, despite some of its limitations derived in part from the fact that the role of calcium in contraction was yet undiscovered.

The processes leading to tension generation described in the previous section are described in a wide range of mathematical models. They vary widely as such models balance complexity, knowledge of biophysical mechanisms, and available experimental data. The choices in prioritizing these aspects will depend on the purpose of the model. The mathematical models vary from the very simple, which relate time since activation, or calcium potential directly to force through a formula (Kerckhoffs et al., 2003a), to detailed models of parts of the sarcomere created to explore a specific mechanistically based hypothesis (Campbell et al., 2011). Many important conceptual models of contraction include a detailed model of tropomyosin kinetics and the crossbridge cycle, including several sub-states depending on the attachment of ATP and position of crossbridges. An important example is the six-state model of McKillop and Geeves (1993). It describes tropomyosin and crossbridge dynamics using a blocked, closed and open state of tropomyosin along with weakly, strongly or unbound crossbridges. While both the open and closed states allow for weak binding of myosin crossbridges, only the open state allows for transition to the force-generating strongly bound state.

For whole-organ simulations, where the force generated is more important than details of the underlying biophysical processes, a different type of model is more common. This

class of models, developed to enable whole organ simulations, typically do not include as many sub-states, but do include enough detail to allow linking parameters to biological data and the exploration of different hypotheses. They also include length- and velocity dependent effects as such feedback is important for whole-organ function. The two models most relevant for this thesis are described in the next two sections. Both of these are relatively simple models used previously in whole-organ electromechanical models.

2.2.8.1 Niederer, Hunter & Smith, 2006

The model developed by Niederer, Hunter, and Smith (2006) was based on the model by Hunter, McCulloch, and Ter Keurs (1998) which reproduces many experimental results on isolated myocytes and was developed specifically for organ-scale simulations. It models calcium dynamics, active tension and its length and velocity dependence. The model was developed to be species and temperature specific, using the large amount of data available from rats at 25°C.

In this framework, calcium/TnC dynamics are modelled by a simple molecular binding model:

$$\frac{\mathrm{d}[\mathrm{Ca}^{2+}]_{\mathrm{Trpn}}}{\mathrm{d}t} = k_{\mathrm{on}}[\mathrm{Ca}^{2+}]_{\mathrm{i}}\left([\mathrm{Ca}^{2+}]_{\mathrm{TrpnMax}} - [\mathrm{Ca}^{2+}]_{\mathrm{Trpn}}\right) - k_{\mathrm{off}}[\mathrm{Ca}^{2+}]_{\mathrm{Trpn}} \tag{2.4}$$

Where $[\mathrm{Ca}^{2+}]_{\mathrm{TrpnMax}}$ is the total TnC concentration, and the unbinding rate k_{off} is tension dependent.

Tropomyosin/crossbridge dynamics are modelled by representing the transient changes in the proportion of available actin sites z:

$$\frac{\mathrm{d}z}{\mathrm{d}t} = \alpha_0\left(\frac{[\mathrm{Ca}^{2+}]_{\mathrm{Trpn}}}{[\mathrm{Ca}^{2+}]_{\mathrm{Trpn50}}}\right)^n(1-z) - \alpha_{\mathrm{r1}}z - \alpha_{\mathrm{r2}}\frac{z^{n_r}}{z^{n_r} + K_z^{n_r}} \tag{2.5}$$

Where the sensitivity $[\mathrm{Ca}^{2+}]_{\mathrm{Trpn50}}$ is length-dependent.

Whereas length dependence can often be represented by a modification to binding rates or scaling of force, the complex response to shortening velocity requires a more detailed model. One of these is the so-called fading memory model (FMM) (Bergel and Hunter, 1979; Hunter et al., 1998),which represents the velocity response as a several strain-rate dependent variables which all decay with time, making them predominantly dependent on a the window of most recent deformation.

The FMM model was used in the contraction model by Hunter, McCulloch and ter Keurs, and was further adapted in the NHS model to better represent both shortening and lengthening of muscle. An advantage of this model is that it is independent of the contraction model, as it can be added as an addition after modelling isometric tension and length-dependence. Furthermore, many of its parameters can be directly linked to the sinusoidal analysis techniques described previously. As such, it does have the assumption that the velocity response is independent of tension generated, or the current length of

the sarcomere.

The fading memory model introduces several equations of the form:

$$\frac{\mathrm{d}Q_i}{\mathrm{d}t} = A_i \frac{\mathrm{d}\lambda}{\mathrm{d}t} - \alpha_i Q_i. \tag{2.6}$$

The A_i parameters are directly related to the viscous and elastic moduli, and α_i to the frequencies. $2\pi b, 2\pi c, 2\pi d$, i.e. parameters α_1, A_1 are related to the slower 'B process', α_2, A_2 to the faster 'C process', and α_3, A_3 to the 'D process'. Depending on whether experimental data shows a clear 'D process', the third equation can be omitted or not.

The effect on tension $g(Q)$ is given by an equation derived from the Hill force-velocity curve (Bergel and Hunter, 1979), extended to model stretch and shortening in a symmetric way (Niederer et al., 2006):

$$g(Q) = \begin{cases} \frac{aQ+1}{1-Q} & Q \leq 0 \\ \frac{1+(a+2)Q}{1+Q} & Q > 0 \end{cases} \quad \text{where } Q = \sum_{i=1}^{2} Q_i \tag{2.7}$$

Where a is the slope of Hill force-velocity equation.

Finally, active tension is determined by the available actin sites, an additional length-dependent factor, and the maximal 'reference' isometric tension T_{ref} at saturated calcium and resting sarcomere length:

$$T_a = T_{\mathrm{ref}} \cdot g(Q) \cdot \left(1 + \beta_0 \left(\lambda - 1\right)\right) \cdot \frac{z}{z_{\mathrm{Max}}} \tag{2.8}$$

2.2.8.2 Rice, Wang, Bers & de Tombe, 2008

The Rice et al. (2008a) model is a more complex model of crossbridge dynamics and contraction. It includes two TnC buffers, with a length-dependent term determining the effective TnC concentration. Instead of two states describing tropomyosin/crossbridge dynamics, it has a more detailed 4 state Markov model which includes non-permissive, permissive, pre-powerstroke and post-powerstroke states. The most important of these is the transition from the non-permissive N state to the permissive P state which is part of the cross-bridge cycle. Transition rates between these two states are given by:

$$k_{n\_pT} = k_{n\_p} \cdot \mathrm{permtot} \tag{2.9}$$

$$k_{p\_nT} = k_{p\_n} \,/\, \mathrm{permtot} \tag{2.10}$$

$$\mathrm{permtot} = \sqrt{\frac{1}{1 + \left(\frac{\mathrm{perm}_{50}}{\mathrm{Trop}_{\mathrm{Regulatory}}}\right)^{n_{\mathrm{perm}}}}} \tag{2.11}$$

Where $\mathrm{Trop}_{\mathrm{Regulatory}}$ is the effective regulatory troponin concentration, perm_{50} related to the calcium sensitivity, and n_{perm} is related to the degree of cooperativity. The cross-bridge cycle consists of the states P, $\mathrm{XB}_{\mathrm{PostR}}$ and $\mathrm{XB}_{\mathrm{PreR}}$ corresponding to the fraction

of crossbridges in a permissive, pre-powerstroke and post-powerstroke state.

The Rice et al. model uses a velocity dependence based on work by Razumova et al. (1999). In this model the post and pre-force states of crossbridges are multiplied with an average distortion state, which models the temporary distortion of crossbridges from shortening and lengthening.

$$\frac{\mathrm{dxXB_{PreR}}}{\mathrm{d}t} = c_1 \frac{\mathrm{d}\lambda}{\mathrm{d}t} - c_2 \mathrm{xXB_{PreR}} + c_3 \left(\mathrm{xXB_{PostR}} - x_0\right) \tag{2.12}$$

$$\frac{\mathrm{dxXB_{PostR}}}{\mathrm{d}t} = c_1 \frac{\mathrm{d}\lambda}{\mathrm{d}t} + c_4 \mathrm{xXB_{PreR}} - c_4 \left(\mathrm{xXB_{PostR}} - x_0\right) \tag{2.13}$$

The model also includes several effects of these variables on crossbridge transition rates. The biological basis of this model is the idea that during crossbridge cycling, the myosin head can be characterized as weakly bound or strongly bound depending on its orientation. Length changes briefly distort the orientation of the myosin heads, thereby influencing the generation of tension. This biophysical basis is controversial (Yadid and Landesberg, 2010), as is the description of crossbridge dynamics in general. Nevertheless, the model reproduces experimental data well and is relatively simple.

Active tension is determined by the number of crossbridges effectively in the post-powerstroke state, after taking into account distortion.

$$T_a = T_{\mathrm{ref}} \cdot \mathrm{SOVF_{thick}}(\lambda) \cdot \frac{\mathrm{xXB_{PreR}} \cdot \mathrm{XB_{PreR}} + \mathrm{xXB_{PostR}} \cdot \mathrm{XB_{PostR}}}{x_0 \cdot \mathrm{XB}^{\mathrm{Max}}_{\mathrm{PostR}}} \tag{2.14}$$

Where $\mathrm{SOVF_{thick}}(\lambda)$ is a function modelling filament overlap, which is equivalent to the $\left(1 + \beta_0 \left(\lambda - 1\right)\right)$ term with $\beta_0 = 1.65$ in the NHS model when near resting sarcomere length.

2.3 Tissue-scale physiology and modelling

To achieve efficient pump function, heart cells are organized into a specific tissue microstructure. This tissue microstructure is important for both electrical and mechanical properties of cardiac tissue. The elongated shape of cardiac cells define a consistent 'fiber direction' in tissue. This is the direction in which cells are stiffest, contract along, and are most conductive. There are also clear sheet structures along which cells are more tightly bound together. For more details see the detailed histological measurements along with mathematical modelling of the tissue microstructure by LeGrice et al. (1995); Legrice et al. (1997), and the recent review by Anderson et al. (2009).

Currently, these measurements are becoming more common due to diffusion tensor MRI technology, which allows for non-invasive measurement of the tissue microstructure (Healy et al., 2011). Recent research by Gilbert et al. (2012) has shown this technique to not only detect fiber directions, but also yields comparable measurements for sheet directions.

2.3.1 Electrophysiology

The tissue microstructure is important in defining the electrical properties of cardiac tissue. Cells in tissue are electrically coupled through gap junctions along the fiber direction, and through the extracellular medium. With each beat, a coordinated reaction-diffusion process driven by a high conductivity, fast upstroke and long recovery time of action potentials quickly activates all the cells to ensure synchronous contraction. For the electromechanical models in this research, the tissue electrophysiology is used mainly to define an activation pattern for contraction.

2.3.2 Electrophysiological modelling

In modelling cardiac tissue, the starting point is a continuum assumption, which ignores the individual cells and describes an average, homogeneous, region in tissue. This avoids the computational cost of modelling all of the approximately 5 billion cells in a human heart. Even in smaller animals where the number of cells is not a computational barrier, it avoids having to acquire detailed data about cell type and connectivity, in favour of using more general bulk properties of cardiac tissue.

Models of tissue electrophysiology are almost exclusively based on the bidomain formulation, which models tissue as two interleaving continuous spaces, the intracellular and extracellular spaces. Associated with these spaces are the intracellular potential ϕ_i and extracellular potential ϕ_e. A good introduction, which derives the equations in more detail is given in Keener and Sneyd (1998). The bidomain equations are usually given in terms of the intracellular potential and the transmembrane potential $V_m = \phi_i - \phi_e$.

$$\frac{\partial V_m}{\partial t} = \nabla \cdot \left(\frac{\boldsymbol{\sigma_i}}{\chi C_m} \nabla \phi_i \right) - \frac{1}{C_m}(I_{\text{ion}} + I_{\text{stim}}) \tag{2.15}$$

$$\nabla \cdot ((\boldsymbol{\sigma_i} + \boldsymbol{\sigma_e}) \nabla \phi_e) = -\nabla \cdot (\boldsymbol{\sigma_i} \nabla V_m) - I_{\text{stim}} \tag{2.16}$$

Where χ is the surface to volume ratio of cells, C_m the membrane capacitance, and $\boldsymbol{\sigma_i}, \boldsymbol{\sigma_e}$ the intracellular and extracellular conductances. The first of these equations describes the current across the membrane and the second, equivalent to $\nabla \cdot (\boldsymbol{\sigma_i} \phi_i + \boldsymbol{\sigma_e} \phi_e) = 0$, enforces conservation of charge between the two spaces.

When the conductivities are equally anisotropic, or the extracellular domain is highly conductive, the bidomain equations reduce to the monodomain equations:

$$\frac{\partial V_m}{\partial t} = \nabla \cdot (\boldsymbol{D} \nabla V_m) - \frac{1}{C_m} (I_{\text{ion}} + I_{\text{stim}}) \tag{2.17}$$

Where $\boldsymbol{D} = \frac{\boldsymbol{\sigma_i}(\boldsymbol{\sigma_i} + \boldsymbol{\sigma_e})^{-1} \boldsymbol{\sigma_e}}{\chi C_m}$.

Even in cases where anisotropy is not strictly equal, like in cardiac tissue, the monodomain model can still be suitable in situations where the extracellular potential is not important. For example, in simulations of an isolated heart under normal sinus rhythm. In this case it can be considered a relaxed version of the bidomain model (Colli Franzone et al., 2005). The monodomain model can be an order of magnitude more computation-

ally efficient and is sufficient to reproduce many of the observations of wave propagation. However, in simulations where current is injected in the extracellular space, for example to simulate defibrilation, the full bidomain model is required to match phenomena observed experimentally (Clayton and Panfilov, 2008).

For both models, the values of the conductivities $\boldsymbol{\sigma_i}, \boldsymbol{\sigma_e}, \boldsymbol{\sigma}$ are not easy to determine using experiments, since they do not directly correspond to physical quantities. Some experiments have tried to find measure equivalent physiological quantities, but no useful experimental data is available (Roth, 1997; Clayton and Panfilov, 2008). Therefore, they are usually chosen in such a way that accurate numerical simulations will match observed wave propagation speed (also known as conduction velocity) and anisotropy ratio. There is also some debate as to whether conductivity of cardiac tissue is transversely isotropic or orthotropic (Hooks et al., 2002), although the former choice is still more common.

Changes in cell length and curvature also potentially have effects on the conductivity. This has previously been modelled by changing conductivity tensors as the tissue deforms in the monodomain equations (Nash and Panfilov, 2004; Whiteley et al., 2007):

$$\frac{\partial V_m}{\partial t} = \frac{1}{\det \boldsymbol{F}} \nabla_X \cdot \left(\det \boldsymbol{F} \boldsymbol{D} \boldsymbol{C}^{-1} \nabla_X V_m \right) - \frac{1}{C_m} \left(I_{\text{ion}} + I_{\text{stim}} \right) \tag{2.18}$$

Where $\mathbf{X}, \boldsymbol{F}, \boldsymbol{C}$ are the original position, deformation gradient, and strain tensor further explained in the section on mechanics modelling, which follows below.

The importance of mechanical deformation on the electrical properties is a topic of debate. Although the monodomain and bidomain equations suggest the term is important, actual conductivities are dominated by gap junctions between cells which to a first order approximation do not change when the tissue is deforming. However, experimental data and modelling analysis suggest that membrane capacitance and intercellular resistance are involved in conduction slowing (Mills et al., 2008). All of these effects are minor, since the electrical activation of the heart finishes before any large mechanical deformation starts. Without the deformation terms, the calculation is more efficient, as the same matrix can be used in each time step.

Research on the monodomain and bidomain equations is still a very active field, and doing these simulations on a realistic geometry is a challenging computational problem. Recent overviews are given by Linge et al. (2009) who focus on the bidomain equations, and Clayton et al. (2011) who provide an overview of techniques and open questions for electrophysiology simulations. The next chapter deals with the computational implementation of the monodomain equations in more detail.

2.3.3 Mechanics modelling

For the modelling of the mechanical properties of cardiac tissue we use nonlinear solid mechanics. This is the same mathematical framework commonly used for modelling many other materials. The mathematical theory is introduced only briefly here. More in-depth

treatment can be found in standard textbooks such as Bonet and Wood (2008).

In solid mechanics theory, deformation of an object can be described by a function:

$$\mathbf{x} = \mathbf{x}(\mathbf{X}, t) \tag{2.19}$$

The original position $\mathbf{X}$ is known as the *reference configuration* and $\mathbf{x}$ is the *deformed configuration.*

The deformation gradient tensor, which deforms the original line segment $\mathrm{d}\mathbf{X}$ to a deformed segment $\mathrm{d}\mathbf{x} = \boldsymbol{F}\mathrm{d}\mathbf{X}$ can then be defined as:

$$\boldsymbol{F} = \nabla\mathbf{x} \;\text{ so }\; F_{ij} = \frac{\partial x_i}{\partial X_j} \tag{2.20}$$

The two most important concepts in solid mechanics theory are *stress* and *strain.* Strain is a description of deformation in terms of relative displacement, and can be measured using length changes, commonly using the square of the local change in distances due to deformation:

$$\mathrm{d}\mathbf{x}\cdot\mathrm{d}\mathbf{x} = \mathrm{d}\mathbf{X}\boldsymbol{F}^T\boldsymbol{F}\mathrm{d}\mathbf{X} = \mathrm{d}\mathbf{X}\boldsymbol{C}\mathrm{d}\mathbf{X} \tag{2.21}$$

Where $\boldsymbol{C} = \boldsymbol{F}^T\boldsymbol{F}$ is Green's deformation tensor, or right Cauchy-Green deformation tensor.

Another measure of strain is the Lagrangian/Green's strain tensor $\boldsymbol{E}$, which describes the local change in length compared to rigid body motion:

$$\frac{1}{2}\left(\mathrm{d}\mathbf{x}_1\cdot\mathrm{d}\mathbf{x}_2 - \mathrm{d}\mathbf{X}_1\cdot\mathrm{d}\mathbf{X}_2\right) = \mathrm{d}\mathbf{X}_1^T\boldsymbol{E}\mathrm{d}\mathbf{X}_2 \text{ where } \boldsymbol{E} = \frac{1}{2}(\boldsymbol{C}-\boldsymbol{I}) \tag{2.22}$$

Stress is a measure of the internal forces acting on an object. In the deformed configuration, the force per area at each point is given by the traction $\mathbf{t}$, which can be expressed in terms of the Cauchy stress tensor $\boldsymbol{\sigma}$, as

$$\boldsymbol{\sigma}\mathbf{n} = \mathbf{t} \tag{2.23}$$

Where $\mathbf{n}$ is the area's unit normal.

Thus, in an object in static equilibrium, for any small cube at point $\mathbf{x}$ with surface S and dimensions $\delta x \times \delta x \times \delta x$, the balance of forces is given by:

$$0 = \int_S \mathbf{t}\,\mathrm{d}S = \delta x^2 \sum_i \boldsymbol{\sigma}(\mathbf{x})\mathbf{e_i} + \boldsymbol{\sigma}(\mathbf{x}+\mathbf{e_i}\delta x)(-\mathbf{e_i}) = \delta x \sum_i \frac{\left(\boldsymbol{\sigma}(\mathbf{x}+\mathbf{e_i}\delta x) - \boldsymbol{\sigma}(\mathbf{x})\right)\mathbf{e_i}}{\delta x} \tag{2.24}$$

Taking $\delta x \to 0$ yields

$$\forall j:\ \sum_i \frac{\mathrm{d}\sigma_{ji}}{\mathrm{d}x_i} = 0, \tag{2.25}$$

Which is the main equation to be solved in a (quasi-)static solid mechanics problem. The problem can also be restated in the undeformed configuration, using the second Piola-

Kirchhoff stress tensor $\boldsymbol{T}$ and the relation

$$\boldsymbol{\sigma} = \frac{1}{\det \boldsymbol{F}} \boldsymbol{F}\boldsymbol{T}\boldsymbol{F}^{\boldsymbol{T}} \tag{2.26}$$

Stresses can be expressed in terms of strain using a *constitutive law*, described in the next section.

Many materials can more easily change shape than volume. In this case the material can be modelled as completely incompressible, by requiring the additional constraint:

$$\det \boldsymbol{F} = 1 \tag{2.27}$$

With this extra constraint, an extra unknown p is introduced which represents the hydrostatic pressure responsible for the incompressibility. This term appears in the Cauchy stress tensor as $-p\boldsymbol{I}$, and as $-p\mathbf{C}^{-1}$ in the second Piola-Kirchhoff stress.

2.3.3.1 Constitutive laws

The solution to the mechanics problem requires a description of the material behaviour known as the *constitutive law*, which gives the stress as a function of the strain for the material.

Most constitutive laws for cardiac tissue go back to Fung, who observed an exponential relation between strain and stress (Fung, 1993). Like the electrical properties, the direction of fibers is important, as myocardial tissue is highly anisotropic and nonlinear. Therefore, the constitutive laws introduced below are given in terms of a coordinate system locally aligned with the fiber, sheet, and normal directions $(\mathbf{f}, \mathbf{s}, \mathbf{n})$ in the reference configuration. Given these directions we can define the matrix:

$$\boldsymbol{L} = [\mathbf{f}\ \mathbf{s}\ \mathbf{n}] \tag{2.28}$$

Where the vectors are properly normalized and the signs chosen such that L is orthonormal. The strain tensor is transformed to a fiber-aligned coordinate system using $\boldsymbol{E}^{\boldsymbol{fsn}} = \boldsymbol{L}^T\boldsymbol{E}\boldsymbol{L}$, stress tensor $\boldsymbol{T}^{\boldsymbol{fsn}}$ is determined using one of the constitutive laws, and transformed back using $\boldsymbol{L}\boldsymbol{T}^{\boldsymbol{fsn}}\boldsymbol{L}^T$. For a transversely isotropic law, $\mathbf{s}, \mathbf{n}$ are arbitrary, as long as L is orthonormal.

A constitutive law is usually expressed as a *strain energy function* W, and the relation:

$$\boldsymbol{T}^{\boldsymbol{fsn}} = \frac{\mathrm{d}W}{\mathrm{d}\boldsymbol{E}^{\boldsymbol{fsn}}} \tag{2.29}$$

This form of a constitutive law automatically ensures some important theoretical restrictions, such as consistency under changes of coordinate system.

A commonly used cardiac constitutive law is the transversely isotropic law proposed

by Guccione et al. (1991):

$$\begin{aligned} W &= {}^1\!/_2\, C_1 \left(e^Q - 1\right) \text{ where} \\ Q &= C_2 E_{ff}^2 + C_3 \left(E_{ss}^2 + E_{nn}^2 + 2E_{sn}^2\right) + 2C_4 \left(E_{fs}E_{sf} + E_{fn}E_{nf}\right) \end{aligned} \tag{2.30}$$

This constitutive law is used throughout the thesis, as it strikes a good balance between detail and parametrizability. Another common constitutive law is the an extension of the Guccione law by Costa et al. (2001) to model orthotropic behaviour, with stress-strain laws differing in three orthogonal directions:

$$W = {}^1\!/_2\, C_1 \left(e^Q - 1\right) \tag{2.31}$$

$$Q = \sum_{i,j\in\{f,s,n\}} b_{ij} E_{ij}^2 \tag{2.32}$$

Other orthotropic laws include the pole-zero proposed by Nash and Hunter (2000) and recent constitutive law proposed by Holzapfel and Ogden (2009), and several variations on these (Schmid et al., 2006).

Using a strain energy function, the hydrostatic pressure term, and an active tension T_a can in the fiber direction $\mathbf{f}$, we can express the second Piola-Kirchhoff stress tensor as:

$$\boldsymbol{T} = \boldsymbol{L}\frac{\mathrm{d}W}{\mathrm{d}\boldsymbol{E}^{\boldsymbol{fsn}}}\boldsymbol{L}^T - p\mathbf{C}^{-1} + T_a \mathbf{f}\mathbf{f}^T, \tag{2.33}$$

which expresses the stresses in actively contracting incompressible cardiac tissue in terms of its strain, and completes the set of equations required to model actively contracting cardiac tissue.

2.4 Windkessel models

The blood pumped by the heart appears in electromechanical models as a mechanical boundary condition for the cavity pressure. During ejection, the change in pressure can be accurately simulated using a Windkessel model.

This framework models the aorta as a compliant vessel, which obeys

$$p_{\mathrm{ao}} = v_{\mathrm{ao}}/C, \tag{2.34}$$

where C is the total arterial compliance, and $v_{\mathrm{ao}}, p_{\mathrm{ao}}$ the volume of blood in the aorta and pressure in the vessel, respectively. Blood flow to the rest of the body is modelled as a simple resistance model

$$I_{\mathrm{out}} = \left(p_{\mathrm{ao}} - p_{\mathrm{out}}\right)/R, \tag{2.35}$$

where R is the peripheral resistance, and the external pressure $p_{\mathrm{out}} \approx 0$ is assumed. These elements make up the two-element Windkessel model, introduced by Frank (1899). A third element, aortic characteristic impedance, was proposed by Broemser and Ranke (1930),

which introduces a second resistance Z for the aortic valve, resulting in more realistic aortic pressure waves. The resulting three-element Windkessel model is given by:

$$\begin{aligned} \frac{\mathrm{d}v_{\mathrm{lv}}}{\mathrm{d}t} &= \frac{1}{Z}\left(p_{\mathrm{ao}} - p_{\mathrm{lv}}\right) && (2.36)\\ \frac{\mathrm{d}v_{\mathrm{ao}}}{\mathrm{d}t} &= -I_{\mathrm{out}} - \frac{\mathrm{d}v_{\mathrm{lv}}}{\mathrm{d}t} && (2.37)\\ I_{\mathrm{out}} &= \frac{1}{R}p_{\mathrm{ao}} && (2.38)\\ p_{\mathrm{ao}} &= v_{\mathrm{ao}}/C && (2.39) \end{aligned}$$

Where $v_{\mathrm{lv}}, p_{\mathrm{lv}}$ are left-ventricular volume and pressure, respectively. This equation can be solved for $\frac{\mathrm{d}^2 v_{\mathrm{lv}}}{\mathrm{d}t^2}$, resulting in:

$$\frac{\mathrm{d}^2 v_{\mathrm{lv}}}{\mathrm{d}t^2} = -\left(\frac{1}{CZ} + \frac{1}{RC}\right)\frac{\mathrm{d}v_{\mathrm{lv}}}{\mathrm{d}t} - \frac{p_{\mathrm{lv}}}{CZR} - \frac{1}{Z}\frac{\mathrm{d}p_{\mathrm{lv}}}{\mathrm{d}t} \tag{2.40}$$

A further extension has been proposed by Stergiopulos et al. (1999), who introduce inertance of the blood flow through the aortic valve as a fourth element. In this thesis we use the commonly used three-element model to represent hemodynamics, as it is easier to solve and parametrize, and the differences with the four-element model are small (Segers et al., 2008).

2.5 Electromechanical models

Electromechanical models integrate the models described in the previous sections, and combine them in a coupled multiphysics simulation, connecting the mechanical deformation of the heart to electrical and mechanical activity of the constituent cells. These models are used for several different purposes, from investigating specific biological hypotheses to clinically relevant modelling.

Although cardiac mechanical and electrical models have existed for many decades, coupled electromechanical models are relatively recent. In the pioneering work by Usyk, LeGrice, and McCulloch (2002), a 3D electromechanical model of the ventricles was developed based on an earlier mechanics model by Nielsen et al. (1991). This electromechanics model was based on cubic Hermite finite element, and a simple phenomenological cell model. It was very influential in early electromechanics research, and was used to investigate the timing of electrical activation and mechanical contraction (Usyk and McCulloch, 2003b), as well as a study on the effects of biventricular pacing in hearts suffering from left bundle branch block (Usyk and McCulloch, 2003a).

An early study by Sachse et al. (2004) used a high-dimensional guinea pig cell model coupled to a detailed tension and monodomain model. Other early work by Kerckhoffs et al. (2003a) was based on a simpler "eikonal" electrics model, which tracks the propagation wave front instead of solving cell models. Work by this group showed that a constant delay between crossbridge formation and electrical activation leads to unrealistic deforma-

tion. The same model was also used in several related studies focused on analysing the effects of altered depolarization due to pacing (Kerckhoffs et al., 2003b,c, 2005).

The two groups involved in the work by Usyk et al, from the University of California, San Diego and the University of Auckland, have both continued to advance electromechanical models. The UCSD group, joined by Kerckhoffs, have published a number of other studies using electromechanical models. They performed further research into the effect of pacing sites in the context of chronic infarcts (Kerckhoffs et al., 2009), and the impact of major cardiac abnormalities on heart function and clinical measures of dyssynchrony (Kerckhoffs et al., 2010). There are also several studies by Campbell et al. on the mechanisms of transmural variations in excitation-contraction coupling (Campbell et al., 2008b,a), and a recent study by Aguado-Sierra et al. (2011) on patient-specific modelling of dyssynchronous heart failure.

Related to the Auckland group, Smith et al. (2003) developed an early 2D electromechanical model and used it to investigate the effect of cardiac deformation on ECG measurements. Nash and Panfilov (2004) investigated the effect of deformation-dependent conductivity on re-entrant arrhythmias. Nickerson et al. developed another early detailed electromechanics model (Nickerson et al., 2005; Nickerson, 2005). This model included length- and velocity dependence based on the Hunter-McCulloch-ter Keurs contraction model. However, the model took on the order of 4000 processor hours to solve a single cycle of electromechanical activity and instabilities appeared in the solution.

In more recent work on strongly coupled electromechanical models, these stability issues were addressed by Niederer and Smith (2008), leading to the stable 'update method', which will be described in more detail in the next chapter. These authors continued work on electromechanics by studying the effects of tension-dependent binding of TnC on calcium dynamics (Niederer et al., 2009b) in a rat model, as well as the relative role of length- and velocity dependence mechanisms on the efficiency of whole organ pump function (Niederer and Smith, 2009). In more recent work using human models they investigated the effect of length-dependent tension in the failing heart and CRT (Niederer et al., 2011a) and quadripolar pacing (Niederer et al., 2012b,a).

Several other groups have also independently done work in electromechanical modelling of the heart. Among these are groups who have investigated numerical methods for electromechanics, such as the non-standard solution methods by Göktepe et al. (Göktepe and Kuhl, 2009, 2010) and Wong et al. (2010). Pathmanathan and Whiteley generalized the stable solution process of Niederer et al. and investigated convergence of the mechanics component (Pathmanathan and Whiteley, 2009; Pathmanathan et al., 2010).

Nordsletten et al. (2011) review coupling of electromechanical models to other components, including fluid dynamics, and coronary perfusion. Of these possibilities, only a coupled electromechanics-fluid model has been realized, in research by Watanabe et al. (Watanabe et al., 2004, 2008), although on a simple and non-refined model of the heart.

The Panfilov group has continued work on electromechanics in the work by Keldermann et al. (2010) on the potential role of stretch-activated channels on re-entrant wave excitation. There is also significant interaction with the field of image processing. The geometry used in electromechanical models is also often derived from image data, such as MRI measurements. Work by Gurev et al. (2011) and Lamata et al. (2011) determining and discretizing a cardiac geometry from such experimental data. The research group at INRIA have used electromechanical models to enhance image analysis (Sermesant et al., 2006), as well as much research into the use of MRI data for personalizing cardiac electromechanical models (Chabiniok et al., 2012; Delingette et al., 2012; Sermesant et al., 2009).

More recently several other groups have begun research on electromechanical models, such as work by Evangelista et al. (2011) Wall et al. (2012) Lafortune et al. (2012) Nobile et al. (2012). For more on electromechanical models see the reviews by Kerckhoffs et al. (2006) and Trayanova et al. (2011).

Historically, simulating cardiac electromechanics has been a computationally difficult problem to solve. Most of these computational difficulties are related to the resolution needed to solve the monodomain and bidomain equations to convergence. Although efficient parallel solvers for the electrics problem exist, parallelization in electromechanics is more complicated, due to the required coupling and different characteristics of the electrics and mechanics problems. As a result, much of the research cited above uses meshes with a density lower than required for convergence. Although this may not be necessary for demonstrating some aspects of the numerics (e.g. (Göktepe and Kuhl, 2010)), it does raise questions about the suitability of the chosen model, if biological and clinical conclusions are to be drawn. For example, the pioneering work by Usyk et al. used identical meshes with only a few hundred elements for both the monodomain and mechanics problems and the work by Watanabe et al. (2008) uses three coupled problems each of which are not solved to convergence, making their results more difficult to interpret. The earlier work by Kerckhoffs et al. (2003a) used a simpler eikonal approach for the electrics problem, which may be more suitable for situations where computational power is limited.

Another consequence of the difficulty of efficiently implementing electromechanics, is the lack of readily available software to perform such simulations. Perhaps the best known software is CMISS, developed at the University of Auckland over the last 30 years. There are efforts to re-implement the functionality in a modern open-source version known as OpenCMISS but support for detailed electromechanics is currently still a work in progress. Another package is Continuity from the UCSD group, which can solve both cardiac electrics and mechanics. Finally, the CHASTE software developed at Oxford (Pitt-Francis et al., 2009), currently supports a simple model of electromechanics. All such packages tend to be difficult to use, and are rarely used for research outside of their respective research groups, as extensive support is needed to set up simulations or change code for original work.

A further challenge is the species- and temperature consistency of such a complex

multiphysics model. As discussed in section 2.2.2, for electrophysiological and contraction cell models by themselves, this already poses a significant challenge. The variety of parameters are introduced at the whole-organ scale including tissue conductivity, geometry and constitutive parameters, as well as hemodynamic boundary conditions. This requires a wide range of experimental data, which is not always available. Especially in human, some model parameters such as constitutive properties may not be practically or ethically possible to obtain via direct measurements and have to be inferred from other whole-organ data (Wang et al., 2009; Xi et al., 2011). A recent example of this is the work by Wall et al. who incorporate a rat stretch-activated channel into a canine electrics model and couples it to the HMT contraction model (based primarily on 20-27°C rat and ferret data), and solve the resulting model on a mesh based on sheep MRI data. Such inconsistency in even the most recent models shows that developing electromechanical models remains a difficult problem.

2.6 Summary

This chapter summarized the current state of cardiac physiology and modelling, especially as it relates to cardiac electromechanics. From this survey it is clear that there are significant challenges remaining for investigating heart failure progression in genetically modified mice using an electromechanical model. Firstly, there is no readily available computational implementation available to use for new electromechanical model development which has the option of changing electrophysiology and contraction models as necessary. This implementation challenge is addressed in the next chapter. Secondly, there have been no mouse electromechanical models published, and pacing frequencies in whole-organ simulations rarely exceed 1 Hz. We address this in Chapter 4 through careful data-driven modelling, where the developed framework is based on more recent available experimental data for the species that is to be modelled, at realistic pacing rates and temperature. Thirdly, extending this model to represent a genetically modified animal requires further data about the quantitative effects of the genetic knockout, including the direct and compensatory effects of the knockout. Furthermore, as highlighted in section 2.2.4, applying any results to make conclusions about heart function in other species is challenging due to the limitations of animal modelling and differences in calcium regulation between species.

Chapter 3

Computational methods

This chapter gives an overview of the computational methods used to solve cardiac electromechanics. It describes our novel implementation developed for solving this coupled multi-physics problem, including development and testing of the numerical methods to make this process more efficient. The resulting framework forms the basis for further model development in the next chapters.

As discussed in the previous chapter, there are few readily available frameworks available for electromechanical simulations. Furthermore, the research described in the next chapters requires significant control over the computational framework, with the ability to change components at will and quickly test variations in model equations and parameters. As the implementation is mainly a means to accomplish the simulations required for this scientific investigation, there is a balance between ease of implementation and efficiency. The methods were initially developed and tested largely in a human modelling framework, as both meshes and models were more readily available at the time this framework was developed, and at the lower heart rate it represents a testing framework with better known properties. The human modelling framework used for testing consists of an electrophysiology model from the literature, contraction model for rat reparametrized to reproduce a human tension transient, and a human left-ventricular geometry from MRI data. For completeness, details of the cell models are described in an appendix at the end of the chapter, although these are less relevant for the rest of the work.

The next sections describe cell model development, along with the ordinary differential equation solver used. After the presentation of the cellular level framework we extend the models to solve tissue electrics using the monodomain equations. Finally, we extend the model to a fully coupled electromechanical framework and describe several optimization methods for mechanics solving.

3.1 Cell modelling

3.1.1 Electrophysiology

For the electrophysiological basis of our human electromechanical testing framework we have chosen to use the model recently published by Grandi, Pasqualini, and Bers (2010) (GPB model) . Compared to other popular human models, it is not as complex as the Iyer et al. (2004) model , and has more realistic calcium dynamics when compared to the models from ten Tusscher et al. (the 'TNNP model' (ten Tusscher et al., 2004) and the 'TP model' (ten Tusscher and Panfilov, 2006)). Specifically, the ten Tusscher et al. models do not include multiple calcium compartments and calcium release from the sarcoplasmic reticulum. This leads to calcium transients whose time to peak is overly fast compared to experimental measurements.

The GPB model is quite detailed, containing a large number of ion channels, and a detailed model of calcium dynamics including several compartments and associated buffers. To improve computational tractability, we have thus simplified this cell model, making it more suitable for use in human whole-organ simulations. We removed several buffering equations by using quasistatic approximations for high-affinity buffers and removing low-affinity buffers. Furthermore, several intracellular sodium concentrations are approximated as constants as they do not vary much. The resulting model has just 26 variables instead of the original 38 and closely approximates the original.

Differences between the models in the action potential and calcium dynamics can be seen in more detail in Fig. 3.1. Details of the model reduction process are described in an appendix (section 3.A).

3.1.2 Contraction

We base our contraction framework on the model by Niederer, Hunter and Smith (NHS model), which was parametrized using experimental data from rats at 25 °C. For consistency with the GPB model, and to give realistic deformation patterns for testing numerical methods, we have reparametrized this model using available experimental data for human cells at body temperature, resulting in the isometric tension transient shown in Fig. 3.2. The resulting model has faster rates of tension development which match isometric tension development measured experimentally, and changes in rate constants are consistent with the temperature differences between the NHS model and body temperature. Details of the parametrization are described in section 3.B.

3.2 Numerical methods for single cell simulations

In this section we investigate explicit numerical methods for efficiently simulating the reduced GPB model. Any differences mentioned in this section are compared to a reference

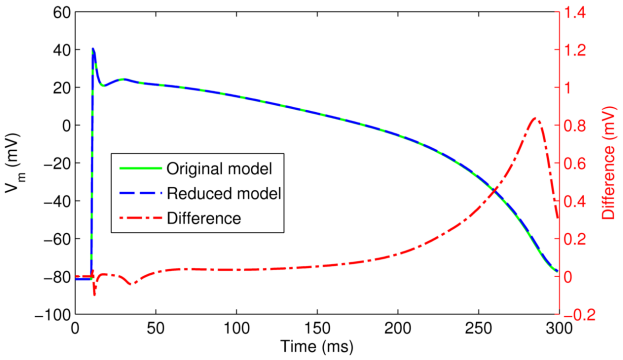

(a) Action potentials

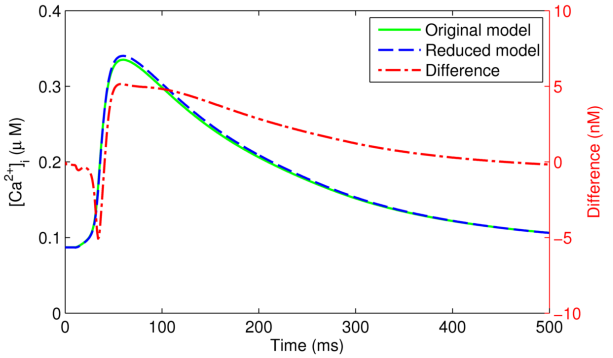

(b) Free Ca^{2+} concentrations.

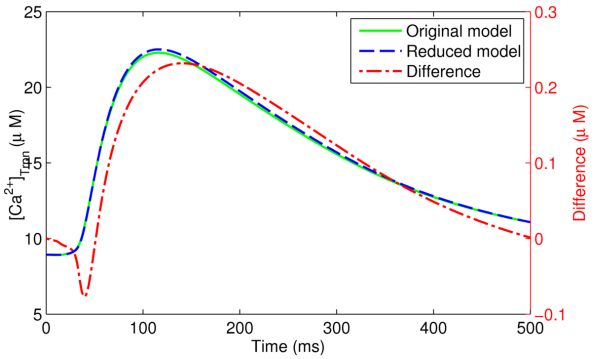

(c) $[Ca^{2+}]_{Trpn}$ concentrations.

Figure 3.1: Comparison between the reduced 26 variable model and original 38 variable GPB model. Panel (a) shows the differences in membrane potential, which are dominated by a slight shift in the timing of repolarization. Panels (b) and (c) show the concentration of free Ca^{2+}, and Ca^{2+} bound to troponin C, respectively. Both of these have maximum differences near their peak value.

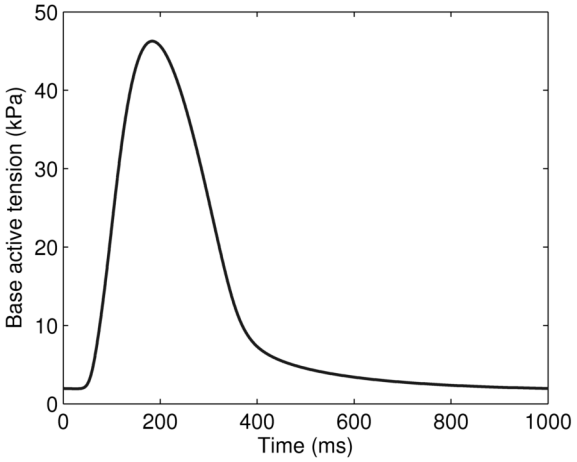

Figure 3.2: Isometric twitch tension. Results of tension generation in the reparametrized NHS model coupled to the reduced GPB model

solution of the reduced model (solved using MATLAB's `ode15s` with a maximum time step of 0.1 ms), and not the original model. First we consider techniques which can be used to make explicit integration more stable, allowing larger time steps, without considering the accuracy of the solver. Next, we investigate adaptive time stepping to obtain the required accuracy, while further improving numerical stability.

3.2.1 Integration methods for Hodgkin-Huxley style gates

A commonly used integration scheme which guarantees the stability of the equations for the Hodgkin-Huxley type gates, is the Rush-Larsen scheme (Rush and Larsen, 1978). This is a first-order method which assumes the opening and closing rates during the time step $[t, t + \Delta t]$ can be taken to be approximately constant, equal to the rate at time t. Using this assumption the exact solution for the fraction of open gates at $t + \Delta t$ is given by:

$$\text{gate}(t + \Delta t) = \text{gate}_\infty(t) - e^{-\Delta t/\tau_{\text{gate}}(t)}(\text{gate}_\infty(t) - \text{gate}(t)) \tag{3.1}$$

Where $\text{gate}_\infty(t)$ is the steady state value given the opening and closing rates at time t and $\tau_{\text{gate}}(t)$ their time scale. Alternatively, the rates can be taken to be equal to the midpoint value, i.e. $\text{gate}_\infty((V_m(t) + V_m(t + \Delta t))/2)$, to give the midpoint steady state value $\text{gate}_\infty(t + \Delta t/2)$.

We propose a simpler alternative scheme, in which the normal forward Euler step is prevented from overshooting this midpoint steady state value. That is, set $\text{gate}(t + \Delta t) = \text{gate}_\infty(t + \Delta t/2)$ whenever the value $\text{gate}(t + \Delta t)_{\text{FWE}}$ given by standard forward Euler step crosses this value (as can be checked using $\frac{\text{dgate}}{\text{d}t}(t) \cdot \big(\text{gate}(t + \Delta t)_{\text{FWE}} - \text{gate}_\infty(t + \Delta t/2)\big) > 0$). This is a first-order method that guarantees the gating variables will stay in their physical $[0, 1]$ range and where solution at each step is bounded between the solutions for the forward Euler and Rush-Larsen method. The method is referred to as the FWE_∞ (forward Euler/steady state) method. For single cell simulations, all of these methods work well,

but there are small differences in the fast upstroke, which are important in monodomain simulations, as we show in the section 3.4.

We apply the FWE_∞ method to the fastest gates (m, d, j), which allows for much larger time steps. However, for steps greater than 0.17 ms oscillations start to appear in the junctional calcium component ($[\text{Ca}^{2+}]_\text{j}$) and its remaining SLH_j buffer during the phase in which this concentration is decreasing. Note that applying a Rush-Larsen like scheme to this buffer does not remove the instability, which seems to be caused by the interaction between different calcium compartments and their buffers. This instability is addressed below using an adaptive time step.

3.2.2 Adaptive time step

Computational efficiency can be further improved by making Δt a function of $\mathbf{v}$ or $\frac{\text{d}\mathbf{v}}{\text{d}t}$. However, the exact rule to use can be dependent on the cell model. In this particular case, the main source of numerical error at $\Delta t \approx 0.1$ ms is the large overshoot in the upstroke and subsequent reaction of the transient outward current, which significantly affects APD_{90}.

To prevent this overshoot we apply an adaptive time step which limits the absolute change in V_m to $\Delta V_{m,\max} = 1$ mV over a single integration step (similar to Luo and Rudy (1991)), and require $\Delta t \leq 0.05$ ms when $V_m > 35$ mV, to prevent a large sideways step at the peak where the derivative is briefly ≈ 0. This last condition is less important in tissue models, where the upstroke tends to be more rounded. Secondly, we use a similar limit to the time step for $[\text{Ca}^{2+}]_\text{j}$, limiting the time step such that $\Delta t J_{[\text{Ca}^{2+}]_\text{j}} \in [-0.001, 0.0015]$ mM, where $J_{[\text{Ca}^{2+}]_\text{j}}$ is the sum of the fluxes in and out of the junctional cleft. These bounds ensure a smaller step during the short phases of fast increase and decrease in $[\text{Ca}^{2+}]_\text{j}$, and removes the instability for the $[\text{Ca}^{2+}]_\text{j}$ component and its buffer.

The resulting method with an adaptive time step gives smooth solutions for a maximum time step of $\Delta t \leq 1/3$ ms, shows minor oscillations for $\Delta t = 0.4$ ms and becomes unstable around $\Delta t = 0.5$ ms, mainly due to the equations for the $[\text{Ca}^{2+}]_\text{i}$ and $[\text{Ca}^{2+}]_\text{SR}$ components. We keep a maximum time step of $\Delta t = 1/3$ ms as standard. For this time step, differences with a reference solution include a 0.2 ms decrease in APD_{90}, 0.3 mV higher spike in the upstroke, 0.07% higher peak $[\text{Ca}^{2+}]_\text{i}$, and 0.03% higher peak $[\text{Ca}^{2+}]_\text{Trpn}$.

Although the integration method is specific to the GPB cell model, the techniques developed are more general. For example, for the TNNP and TP cell models the adaptive time step based on $\frac{\text{d}V_m}{\text{d}t}$ along with the specialized integration scheme for the m, d, h gates, allows for time steps of up to 1 ms with similarly low levels of error.

Below is a pseudocode formulation of the methods used for integrating the single cell model, including the FWE_∞ method and the adaptive time step. In this description, $\mathbf{v}$ is the vector of state variables and f the function which returns $\frac{\text{d}\mathbf{v}}{\text{d}t}$.

Algorithm 1: Integration scheme with adaptive time step for the GPB cell model.

$\mathbf{v} = \mathbf{v}_0$
$t = 0$
$T = 1000$
$\Delta V_{m,\max} = 1$
$J^{\min}_{[\mathrm{Ca}^{2+}]_\mathrm{j}} = -0.001$
$J^{\max}_{[\mathrm{Ca}^{2+}]_\mathrm{j}} = -0.0015$
$\Delta t = 1/3$
while $t < T$ **do**
  $\frac{\mathrm{d}\mathbf{v}}{\mathrm{d}t} = f(t, \mathbf{v})$
  $\Delta t_{\mathrm{curr}} = \Delta t$
  if $\Delta t_{curr} \cdot |\frac{\mathrm{d}V_m}{\mathrm{d}t}| > \Delta V_{m,max}$ **then**
    $\Delta t_{\mathrm{curr}} = \Delta V_{m,\max} / \frac{\mathrm{d}V_m}{\mathrm{d}t}$
  end
  if $V_m > 35$ **then**
    $\Delta t_{\mathrm{curr}} = \min(\Delta t_{\mathrm{curr}}, 0.05)$
  end
  if $J_{[Ca^{2+}]_j} \Delta t_{curr} > J^{max}_{[Ca^{2+}]_j}$ **then**
    $\Delta t_{\mathrm{curr}} = J^{\max}_{[\mathrm{Ca}^{2+}]_\mathrm{j}} / J_{[\mathrm{Ca}^{2+}]_\mathrm{j}}$
  end
  if $J_{[Ca^{2+}]_j} \Delta t_{curr} < J^{min}_{[Ca^{2+}]_j}$ **then**
    $\Delta t_{\mathrm{curr}} = J^{\min}_{[\mathrm{Ca}^{2+}]_\mathrm{j}} / J_{[\mathrm{Ca}^{2+}]_\mathrm{j}}$
  end
  $\mathbf{v} = \mathbf{v} + \Delta t_{\mathrm{curr}} \frac{\mathrm{d}\mathbf{v}}{\mathrm{d}t}$
  for $gate \in \{m, d, j\}$ **do**
    if $\frac{\mathrm{d}gate}{\mathrm{d}t} \cdot (gate - gate_\infty(t + \Delta t_{curr}/2)) > 0$ **then**
      $\mathrm{gate} = \mathrm{gate}_\infty(t + \Delta t_{\mathrm{curr}}/2)$
    end
  end
  $t = t + \Delta t_{\mathrm{curr}}$
end

3.3 Tissue modelling

As explained in the previous chapter, cardiac tissue is modelled using continuum approximation, using the monodomain equations for electrics and nonlinear solid mechanics theory for the deformation. These are both physically and numerically very different problems. For the electrics problem, the computational difficulties are related to the steep wavefront generated by the action potentials seen in typical cell models, which requires a high resolution mesh. However, the spatial term in the problem can be reduced to a sparse

matrix-vector solution process. The mechanics problem is computationally intensive to solve because it is highly nonlinear, especially with the exponential increase in stress seen in cardiac constitutive laws. There are no algorithms that are both tractable and guaranteed to find a solution for such systems of equations, and the calculation involved are computationally intensive.

Because of the differences between these two problems, solving the multiple components in a coupled electromechanical model with all their dependencies as one monolithic system is computationally infeasible, as solving all high-dimensional cell models on a dense grid together with the nonlinear mechanics problem would generate a very large nonlinear system of equations. Instead, we use several numerical techniques to decouple the components and solve each one in an efficient manner. A coupled electromechanics simulation solved in this way consists of the following steps:

- Determine the initial deformation using any applied forces, pressures and residual active tension. (Preload step)

- While time $< t_{\text{end}}$

    1. Solve the monodomain equations and single cell models for a total time of Δt_{mech}. Sections 3.2 and 3.4 describe methods for efficiently solving these equations. For a deformation given by a 1 Hz heart rate, the mechanics time step can be set to $\Delta t_{\text{mech}} = 1$ ms.

    2. Determine relevant cellular quantities for the mechanics model, such as the fraction of bound crossbridges.

    3. Solve for the mechanical deformation using the update method. In section 3.6 we present optimizations for this step.

    4. Determine relevant mechanical quantities for the cell models, such as the active tension or strain.

The update method, described in Niederer and Smith (2008), involves solving the velocity dependent equations of the contraction problem (e.g. the Q_i of the fading memory model) within the Newton iterations of the mechanics solution process. This prevents instabilities that will appear when the velocity of the previous time step is used to integrate these equations.

The next sections describe our implementation of the monodomain and mechanics equations separately. The coupling terms will be discussed in more detail in section 3.5.2 after both of the sub-problems have been discussed separately. Throughout the rest of this chapter we present some novel computational methods for improving the tractability of whole organ simulations. We start by discussing optimizations for electrophysiology, which are also applicable outside of electromechanical models. Finally, section 3.6 presents methods specifically for optimizing the mechanics part of a coupled simulation.

3.3.1 Finite element method

Our computational methods for solving tissue level equations are all based primarily on finite element methods. These are numerical techniques for approximately solving partial differential equations. The main advantage of finite element methods is their flexibility with respect to the geometry of the problem domain, making it very suitable for working with model geometries derived from anatomical data. A full explanation of the finite element method is beyond the scope of this chapter. Basic concepts are briefly explained in this section for the sake of providing context for mathematical symbols used further on. For details consult a text book on finite element techniques (Elman et al., 2005; Bonet and Wood, 2008).
The finite element method is used to approximately solve equations such as

$$\text{find } \mathbf{u}(\mathbf{x}) \text{ such that } \forall \mathbf{x} \in S \quad f(\mathbf{x}, \mathbf{u}) = 0 \tag{3.2}$$

by converting it to a *weak form*:

$$\forall \phi^{(k)} \quad \int_V f(\mathbf{x}, \mathbf{u}) \phi^{(k)}(\mathbf{x}) \, \mathrm{d}\mathbf{x} = 0 \tag{3.3}$$

and finding an approximation to the solution by solving this for a finite set of *basis functions* $\{\phi^{(k)}\}$, known as a *basis*. We use the standard 'Galerkin' finite element methods, in which the solution $\mathbf{u}$ is also limited to be from a linear combination of the same basis functions, i.e. $u(x) = \sum_k \phi^{(k)}(x) u^{(k)}$.

In general, the weak form requires some algebraic manipulation before being usable in a computational setting, by introducing the boundary more explicitly using some variant of the divergence theorem. These details are shown in the specific discretizations later in this chapter. The resulting if f is linear in u, such as for the monodomain and bidomain equations, the problem can be reduced to a simple matrix-vector solution process. Otherwise, it must be solved with a nonlinear solver such as a Newton iteration process, which is the case in nonlinear mechanics.

3.4 Numerical methods for the monodomain model

In this section we investigate numerical methods for the monodomain model, using an operator splitting method similar to Qu and Garfinkel (1999). This method is based on Strang splitting (Strang, 1968), and decouples the cell models from the diffusion part of the monodomain equations, incurring an error of the order $O(\Delta t^2)$ in the process. The resulting method consists of the following steps:

$$\text{solve} \quad \frac{\mathrm{d}V_m}{\mathrm{d}t} = \nabla \cdot \mathbf{D} \nabla V_m \tag{3.4}$$

$$\text{use the result to solve} \quad \frac{\mathrm{d}\mathbf{v}}{\mathrm{d}t} = f(t, V_m, \mathbf{v}) \tag{3.5}$$

$$\text{and} \quad \frac{\mathrm{d}V_m}{\mathrm{d}t} = -\frac{1}{C_m} \left(I_{\text{ion}} + I_{\text{stim}} \right) \tag{3.6}$$

Where $\mathbf{v}$ denotes the vector of all variables of the cell model other than V_m. We use this method over other operator splitting schemes (Whiteley, 2008) since it fully decouples the cell models, which allows us to apply our explicit method with an adaptive time step as developed in the previous section to simulate electrical activation efficiently. This full decoupling also simplifies the implementation in general, allowing for a constant set of equations, as well as easy substitution of the cell model by a different one, which is important in easily adapting the framework for different species and models.

The time-derivative in Equation 3.4 is discretized using a Crank-Nicholson approach:

$$\frac{V_m(t+\Delta t) - V_m(t)}{\Delta t} = \frac{1}{2}\left(\nabla \cdot \mathbf{D}\nabla V_m(t) + \nabla \cdot \mathbf{D}\nabla V_m(t+\Delta t)\right) \tag{3.7}$$

The spatial derivative is handled using the finite element method in our three-dimensional model, described in section 3.4.2.

3.4.1 One-dimensional fiber

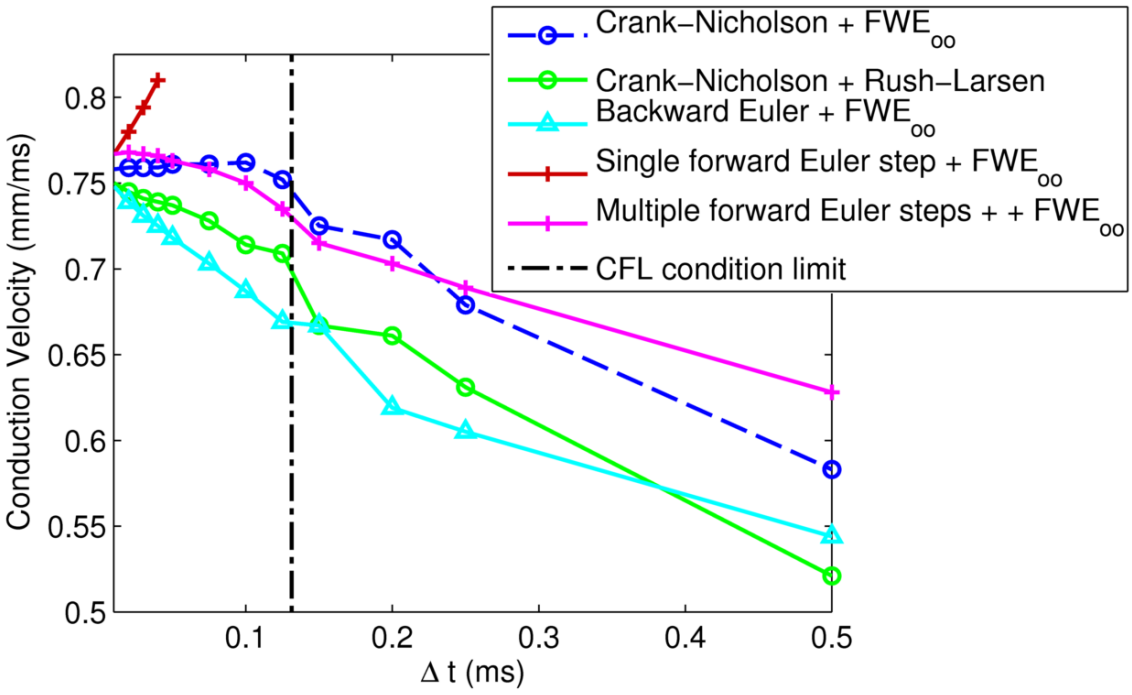

Figure 3.3: Conduction velocity for different numerical methods. Conduction velocity is shown as a function of time step taken for the Crank-Nicholson, backward Euler, and forward Euler methods. Black line indicates $\Delta t = h/\mathrm{CV}(0.1\ \mathrm{ms})$ for the Crank-Nicholson method. The solution labelled "Rush-Larsen" uses the Rush-Larsen scheme on the m, d, j gates, all others use the FWE_∞ scheme for these gates. The "multiple Forward Euler steps" method uses multiple forward Euler steps with a time step of 0.01 ms to integrate the diffusion equations. The dashed blue line using the new FWE_∞ scheme for the cell models combined with the Crank-Nicholson method for the PDE indicates the solution method we use in the rest of our simulations.

Before implementing our methods in a large three-dimensional model of the heart, we first investigate their performance in a more tractable one-dimensional model. This model is used to investigate the interaction with the proposed cell model solver, and its convergence properties related to the time step used. Our one-dimensional model is a simple 10 mm long fiber with nodes spaced 0.1 mm apart, and a finite differences discretization of the diffusion equation, implemented in MATLAB. To determine the method's accuracy we measure the conduction velocity, using a best linear fit to the upstroke times between $x = 3$ mm and $x = 7$ mm to ensure boundary effects will not contaminate the results. We use $D = 0.125$ mm^2/ms to get a CV of approximately 0.75 mm/ms.

Fig. 3.3 shows the conduction velocity for different integration methods for the diffusion equation. The forward Euler method quickly loses accuracy and becomes unstable at PDE time steps $\Delta t_{\text{mono}} > 0.04$ ms, consistent with standard stability analysis. This is very restrictive considering the allowed time step for the cell model, but it is still possible to use this method by integrating over a larger amount of time using several smaller forward Euler steps. Comparing the backward Euler and Crank-Nicholson methods shows that the latter is far more accurate, as can be expected from a second order method, at no significant extra cost. Further examining the accuracy of the Crank-Nicholson method shows the maximum time step for an accurate solution to be around $\Delta t_{\text{mono}} = 0.1 - 0.15$ ms, similar to the time step $\Delta t_{\text{mono}} < h/\text{CV} \approx 0.13$ ms given by the Courant-Friedrich-Lewy condition for a wave travelling at the conduction velocity. Essentially, the cell models need to be updated using the ODE solution process after the wave front has reached them, otherwise conduction velocity slows as the large effects from cells activating their neighbours are delayed.

For greater time steps, the wave travels through multiple grid points in a single integration step, reducing the speed of the reaction-diffusion process. This near-constant CV only appears when using the FWE_∞ scheme. Using the Rush-Larsen method, the CV starts decreasing immediately. The exact reason for this is difficult to determine, but seems to be related to the FWE_∞ method giving a faster upstroke combined with the way the diffusion current is added by our operator splitting method. Similar differences between the methods were found in experiments using the TNNP and TP models. Considering these results we apply the Crank-Nicholson method with a time step of 0.1 ms, in combination with the FWE_∞ scheme for the cell models, in subsequent simulations.

3.4.2 Finite element discretization

For a three-dimensional monodomain problem on an irregular geometry, Equation 3.7 is discretized using a finite element approach in space. We use linear basis functions $\phi^{(1)} \dots \phi^{(n)}$ throughout in solving the monodomain equations.

Converting the term $\nabla \cdot \mathbf{D} \nabla V_m$ to a weak form, and use of integration by parts assum-

ing a zero-flux boundary condition yields:

$$\int_V \phi^{(k)} \nabla \cdot \mathbf{D} \nabla V_m \, \mathrm{d}V = -\int_V \sum_{ij} D_{ij} \frac{\partial \phi^{(k)}}{\partial x_i} \sum_l \frac{\partial \phi^{(l)}}{\partial x_j} V_m^{(l)} \, \mathrm{d}V = -\boldsymbol{A}\tilde{\mathbf{V}}_\mathbf{m} \tag{3.8}$$

$$\text{where } A_{kl} = \int_V \sum_{ij} D_{ij} \frac{\partial \phi^{(l)}}{\partial x_j} \frac{\partial \phi^{(k)}}{\partial x_i} \, \mathrm{d}V \tag{3.9}$$

$$\tag{3.10}$$

Where $\tilde{\mathbf{V}}_\mathbf{m} = \left(V_m^{(1)} \dots V_m^{(n)}\right) = \left(V_m(x^{(1)}) \dots V_m(x^{(n)})\right)$, and $\phi^{(k)}$ is the basis function such that $\phi^{(k)}(x_j) = \delta_{kj}$.
Similarly

$$\int_V \phi^{(k)} V_m \, \mathrm{d}V = \int_V \phi^{(k)} \sum_l \phi^{(l)} V_m^{(l)} \, \mathrm{d}V = \boldsymbol{M}\tilde{\mathbf{V}}_\mathbf{m} \tag{3.11}$$

$$\text{where } M_{kl} = \int_V \phi^{(l)} \phi^{(k)} \, \mathrm{d}V \tag{3.12}$$

$$\tag{3.13}$$

Using these two derivations, Equation 3.7 becomes the matrix-vector problem:

$$\left(\frac{\mathbf{M}}{\Delta t} + \frac{\boldsymbol{A}}{2}\right) \tilde{\mathbf{V}}_\mathbf{m}(t + \Delta t) = \left(\frac{\mathbf{M}}{\Delta t} - \frac{\boldsymbol{A}}{2}\right) \tilde{\mathbf{V}}_\mathbf{m}(t) \tag{3.14}$$

This calculation can be simplified using the mass-lumped approximation $\bar{\boldsymbol{M}}$ instead of $\boldsymbol{M}$, where:

$$\bar{M}_{kl} = \delta_{kl} \int_V \phi^{(k)} \, \mathrm{d}V \tag{3.15}$$

3.4.3 3D fiber model

Our first three-dimensional model is of a $8 \times 1 \times 1$ mm fiber with a regular hexahedral grid using 0.1 mm spacing. We tested our monodomain method and conductivity parameter $\mathbf{D} = \mathrm{diag}\left(1.25, \frac{1.25}{2.2^2}, \frac{1.25}{2.2^2}\right)$ in this model*, by activating the fiber at the leftmost 0.5 mm slice and measuring CV between $x = 2 - 7$ mm. To measure transverse CV we switch fiber directions to a short axis. Results are shown in Table 3.1, and are consistent with the one-dimensional results. Using the Rush-Larsen method instead, once again leads to significant decrease in conduction velocity.

3.4.4 Adaptive time step

Results presented in section 3.4.1 show a limit of approximately 0.1 ms to our monodomain solution method. However, the time step for the cell model integration scheme could potentially be several times greater, as we demonstrated in section 3.2.2.

Solving the monodomain example further shows that after depolarization, diffusion

*i.e. a transversely isotropic conductivity chosen such that the transverse conduction velocity is expected to be $\frac{1}{2.2}$ that of the conduction velocity in the fiber direction.

h (mm)	1/20	1/10	1/5	1/4	1/2	Experimental
Long. CV	0.769	0.758	0.725	0.704	0.588	0.741 ± 0.068
Trans. CV	0.342	0.325	0.281	0.256	0.160	0.331 ± 0.040
Ratio	2.25	2.33	2.58	2.75	3.68	2.2 ± 0.2

Table 3.1: Conduction velocities for different mesh resolutions. CV is shown in mm/ms along with the ratio of longitudinal to transverse CV in the 3D fiber problem for several grid resolutions h on the regular hexahedral mesh. Experimental data from Doi et al. (2003) is from their in vivo measurements on healthy human controls.

is limited, so the time step during this phase could be increased, thereby lifting this limit and increasing the efficiency of both the PDE and ODE solvers. This potential was exploited by using an adaptive time step which depends on the value of $\max|\frac{\partial^2 V}{\partial x^2}|$, which is around 4000 V/mm^2 during activation but less than 0.2 V/mm^2 during the larger part of repolarization. We use a larger (1/3 ms) or smaller (0.1 ms) time step depending on whether $\max|\frac{\partial^2 V}{\partial x^2}|$/(previous Δt) is above or below some threshold θ_d. This results in a clear phase during depolarization in which the smaller time step is taken. When using a criterion independent of the previous time step, there is a tendency to quickly switch between the different time steps at certain phases, as $|\frac{\partial^2 V}{\partial x^2}|$ is dependent on the previous step taken in the cell model integrator.

We can also derive and apply an adaptive time step for our 3D finite element model. Adaptivity in such a model can be implemented using a threshold based on a measure of diffusion derived from the forward Euler discretization:

$$\left(-\boldsymbol{M}^{-1}\boldsymbol{A}\right)\mathbf{V_m} \sim \nabla\cdot(\mathbf{D}\nabla V_m) \tag{3.16}$$

As determining $\bar{\boldsymbol{M}}^{-1}$ is far more time- and memory efficient than calculating $\boldsymbol{M}^{-1}$, we use this approximation throughout our monodomain implementation.

Using this method combined with the adaptive time step to simulate 1000 ms of contraction and relaxation in our fiber takes 3110 time steps in total (157 small steps, 2953 large steps), compared to about 10,000 for an accurate nonadaptive implicit scheme, and 50,000 for forward Euler integration with time step 0.02 ms. The underlying cell model is called approximately 3900 times per cell. The resulting conduction velocity is identical to using a constant 0.1 ms time step for the diffusion equation, and APD_{90} values are around 0.1 ms lower. Compared to a reference solution using a time step of 0.01 ms, APD_{90} values show a similar distribution over the length of the fiber, and are all approximately $0.2 - 0.3$ ms lower. These differences can all be expected from the accuracy of the cell model solver as discussed in section 3.2.2.

3.5 Numerical methods for electromechanics

This section describes the discretization of the solid mechanics equations introduced in the previous chapter, and completes the coupling of the electrical and mechanical problems.

The resulting electromechanical model is used to test several optimization methods related to solving the mechanics equations as part of a coupled multiphysics simulation.

3.5.1 Finite element discretization of the mechanics problem

The implementation of the mechanics problem is also based on the finite element methods, although there are some notable differences due to the fact that this is a nonlinear problem. For the governing equations, recall the balance of stresses (Equation 2.25). If we define $\sigma_{\mathbf{j}*}$ as the column vector representing the jth row of $\boldsymbol{\sigma}$, this can be written as:

$$\forall j: \ \operatorname{div} \sigma_{\mathbf{j}*} = 0, \tag{3.17}$$

Which has the weak form:

$$\forall \phi^{(k)} \forall j: \ \int_V \phi^{(k)} \operatorname{div} \sigma_{\mathbf{j}*} \, \mathrm{d}V = 0, \tag{3.18}$$

Using the divergence theorem $\int_V \mathbf{F} \cdot \operatorname{grad} g + g \left(\operatorname{div} \mathbf{F}\right) \mathrm{d}V = \int_{S=\partial V} g\mathbf{F} \cdot \mathbf{n} \, \mathrm{d}S$, this results in:

$$\forall \phi^{(k)} \forall j: \ \int_V \phi^{(k)} \operatorname{div} \sigma_{\mathbf{j}*} \, \mathrm{d}V = \int_S \phi^{(k)} \sigma_{\mathbf{j}*} \cdot \mathbf{n} \, \mathrm{d}S - \int_V \sigma_{\mathbf{j}*} \cdot \operatorname{grad} \phi^{(k)} \, \mathrm{d}V = 0 \tag{3.19}$$

Since $\mathbf{t} = \boldsymbol{\sigma}\mathbf{n}$:

$$\forall \phi^{(k)} \forall j: \ \int_V \sum_i \sigma_{ji} \frac{\partial \phi^{(k)}}{\partial x_i} \, \mathrm{d}V - \int_S \mathbf{t}_j \phi^{(k)} \, \mathrm{d}S = 0 \tag{3.20}$$

Using Equation 2.26 and incompressibility, the second Piola-Kirchoff form of the weak form can be expressed as:

$$\forall \phi^{(k)} \forall j: \ R_{kj}(\tilde{\mathbf{x}}, \tilde{\mathbf{p}}) = \int_V \sum_{M,N} T_{MN} \frac{\partial x_j}{\partial X_N} \frac{\partial \phi^{(k)}}{\partial X_M} \, \mathrm{d}V - \int_S \mathbf{t}_j \phi^{(k)} \, \mathrm{d}S = 0 \tag{3.21}$$

Where $\tilde{\mathbf{x}} = \left(x_1^{(1)}, x_2^{(1)}, x_3^{(1)}, x_1^{(2)} \ldots x_3^{(n)}\right)$, $\tilde{\mathbf{p}} = \left(p^{(1)} \ldots p^{(m)}\right)$. This equation, with the integrals evaluated using Gaussian integration, forms the basis for our implementation of the solid mechanics problem. The second term is calculated using boundary conditions for $\mathbf{t}$. The first term can be evaluated using the constitutive law for $\boldsymbol{T}$, pre-calculated values of the basis functions, and the deformation gradient $\boldsymbol{F}$, which is calculated using

$$F_{ij} = \frac{\mathrm{d}x_i}{\mathrm{d}X_j} = \frac{\mathrm{d} \sum_k \phi^{(k)} x_i^{(k)}}{\mathrm{d}X_j} = \sum_k \frac{\mathrm{d}\phi^{(k)}}{\mathrm{d}X_j} x_i^{(k)} \tag{3.22}$$

The basis function derivatives are pre-calculated using $\frac{\mathrm{d}\phi^{(k)}}{\mathrm{d}X_j} = \sum_l \frac{\mathrm{d}\phi^{(k)}}{\mathrm{d}\xi_l} \frac{\mathrm{d}\xi_l}{\mathrm{d}X_j}$ where $\frac{\mathrm{d}\xi_l}{\mathrm{d}X_j}$ is determined using a matrix inversion and $\frac{\mathrm{d}X_j}{\mathrm{d}\xi_l} = \sum_m \frac{\mathrm{d}\phi^{(m)}}{\mathrm{d}\xi_l} X_j^{(m)}$.

The incompressibility constraint also has a weak form:

$$\forall k \in [1..m] : \; Q_k(\tilde{\mathbf{x}}) = \int_V \psi^{(k)} \left(\det \boldsymbol{F} - 1\right) \; \mathrm{d}V = 0 \tag{3.23}$$

The basis functions $\psi^{(1)} \dots \psi^{(m)}$ are the same as those used to represent the hydrostatic pressure as $p(\mathbf{x}) = \sum_k \psi^{(k)}(\mathbf{x}) p^{(k)}$. We use trilinear basis functions for the $\psi^{(k)}$, and tricubic Hermite for $\phi^{(k)}$ to ensures continuity of the stresses and strains in the solution (Bradley et al., 1997; Smith et al., 2004).

The resulting $3n + m$ variables $\tilde{\mathbf{x}}$, $\tilde{\mathbf{p}}$ can be solved using the in $3n + m$ constraints R_{kj}, Q_k using a root finding procedure. In our implementation a Newton solver is used, combined with a simple line search method which repeatedly halves the search step to prevent the residual from increasing too much. Although most details of this methods are handled by the software package PETSc, the approach is shown in algorithm 2.

Algorithm 2: Newton Solver with line search.

atol $= 10^{-5}$; `// convergence threshold`
$\alpha_l = 1.05$; `// maximal increase in norm of residual early on`
$\alpha_h = 5$; `// maximal increase in norm of residual later in the search`
$\lambda_h = 10^{-3}$; `// step size threshold`
$\text{iter}_h = 30$; `// iterations threshold`
function residual($\tilde{\mathbf{x}}$, $\tilde{\mathbf{p}}$) **begin**
  return $\big(R_{11}(\tilde{\mathbf{x}},\tilde{\mathbf{p}}) \dots R_{n3}(\tilde{\mathbf{x}},\tilde{\mathbf{p}})\ Q_1(\tilde{\mathbf{x}}) \dots Q_m(\tilde{\mathbf{x}})\big)$
end
function Jacobian($\tilde{\mathbf{x}}$, $\tilde{\mathbf{p}}$) **begin**
  `// entries determined using finite differences`
  return
$$\begin{pmatrix} \frac{\partial R_{11}}{\partial x^{(1)}} & \dots & \frac{\partial R_{11}}{\partial x^{(n)}} & \frac{\partial R_{11}}{\partial p^{(1)}} & \dots & \frac{\partial R_{11}}{\partial p^{(m)}} \\ \vdots & & \vdots & \vdots & & \vdots \\ \frac{\partial R_{n3}}{\partial x^{(1)}} & \dots & \frac{\partial R_{n3}}{\partial x^{(n)}} & \frac{\partial R_{n3}}{\partial p^{(1)}} & \dots & \frac{\partial R_{n3}}{\partial p^{(m)}} \\ \frac{\partial Q_1}{\partial x^{(1)}} & \dots & \frac{\partial Q_1}{\partial x^{(n)}} & 0 & \dots & 0 \\ \vdots & & \vdots & \vdots & & \vdots \\ \frac{\partial Q_m}{\partial x^{(1)}} & \dots & \frac{\partial Q_m}{\partial x^{(n)}} & 0 & \dots & 0 \end{pmatrix}$$
end
function newton-solve($\tilde{\mathbf{x}}$, $\tilde{\mathbf{p}}$) **begin**
  $\mathbf{r} = \text{residual}(\tilde{\mathbf{x}},\tilde{\mathbf{p}})$;
  iter $= 0$; **while** $\|r\| >$ atol **do**
    iter $=$ iter $+1$;
    $\boldsymbol{J} = \text{Jacobian}(\tilde{\mathbf{x}},\tilde{\mathbf{p}})$;
    $\Delta\tilde{\boldsymbol{xp}} = -\boldsymbol{J}^{-1}\mathbf{r}$;
    $\lambda = 2$;
    repeat
      $\lambda = \lambda/2$;
      $(\tilde{\mathbf{x}_n},\tilde{\mathbf{p}_n}) = (\tilde{\mathbf{x}},\tilde{\mathbf{p}}) + \lambda\Delta\tilde{\boldsymbol{xp}}$;
      $\mathbf{r}_n = \text{residual}(\tilde{\mathbf{x}_n},\tilde{\mathbf{p}_n})$;
    until $\|\mathbf{r}_n\| < \alpha_{\text{low}}\|r\|$ **or** $\big(\|\mathbf{r}_n\| < \alpha_{\text{hi}}\|r\|$ **and** $(\text{iter} > \text{iter}_h$ **or** $\lambda < \lambda_h)\big)$;
    $(\tilde{\mathbf{x}},\tilde{\mathbf{p}}) = (\tilde{\mathbf{x}},\tilde{\mathbf{p}}) + \lambda\Delta\tilde{\boldsymbol{xp}}$;
    $\mathbf{r} = \mathbf{r}_n$;
  end
end

3.5.2 Electromechanical coupling

Several quantities still need to be interpolated between the different steps of solving the mechanics and electrics problems. From the finer electrics mesh to the Gaussian quadrature points of the courser mechanics mesh, we interpolate the value of z to each of the mechanics Gauss points using trilinear interpolation.

From the mechanics to the electrics, we need to determine the extension ratio λ at the electrophysiology grid points. This can be done efficiently by using $\lambda = \|f_x\|/\|f_X\|$ where $f_x = \frac{\mathrm{d}\mathbf{x}}{\mathrm{d}\xi} f_\xi$ (likewise for f_X) and $f_\xi = (\cos\alpha, \sin\alpha, 0)$ is the fiber direction in the reference element for a fiber angle α.

Finally, we need the strain and active tension in each of the cell grid points for terms involving length-dependent or tension-dependent binding. Interpolating this from Gauss points back to the electrophysiology grid is problematic, since the Gauss points have much lower resolution and do not extend to the boundaries. The solution we propose involves storing separate values for the state variables $\mathbf{w}$ at the electrophysiology grid points. When determining the new value for λ, we integrate the state variables to determine the length- and velocity-dependent active tension at each grid point.

3.6 Optimizing repeated mechanics solutions

Depending on the number of electrophysiology nodes and number of processors used, either mechanics or electrics may dominate the runtime of the solution process. Algorithmic improvements to the repeated mechanics solution process could thus significantly speed up the coupled solution process.

The most computationally expensive aspects of the mechanics solver are determining the Jacobian of the nonlinear system, and solving the resulting linear system in the Newton iteration, so an effective way to reduce the total simulation time is to reduce the total number of these full Newton iterations needed. We will cover three different methods for accomplishing this.

3.6.1 Strain prediction

We propose to use a technique to reduce the number of iterations needed, using a prediction of the mechanical deformation at the next time step. Such techniques have been applied before (e.g. in structural mechanics (Eriksson, 1993)), but their effectiveness is highly problem dependent and they have not been applied previously in cardiac electromechanics, where length- and velocity-dependent active contraction uniquely drives the deformation.

Changes in the deformation between the 1 ms time steps are small, and stress and strain are generally smooth over time, so a prediction derived by extrapolating from the previous solutions will likely be closer to this solution than directly using the previous solution. Since Newton iterations tend to converge faster when the initial guess is close to the converged solution, this will speed up the overall solution process.

The effectiveness of this approach is demonstrated in section 3.7 by using linear, quadratic and cubic extrapolation. The use of exact polynomial fits to solutions may cause some overfitting when higher order polynomials are combined with potential small errors in the solution due to the convergence criterion. In an attempt to prevent this, we have also tested a "best fit" extrapolation using more previous solutions, which is more likely to detect the general trend in changes while ignoring small deviations. To determine the least squares best fit of order n, $\sum_{i=0}^{n} a_i t^i$, to data points $d(t_j), j = 1 \ldots m$, we solve the linear system $\mathbf{Aa} = \mathbf{b}$ where $A_{kl} = \sum_{j=1}^{m} t_j^{k+l-2}$, $b_l = \sum_{l=1}^{m} d(t_j) t^{m-1}$. See Fig. 3.4 for an example which shows the different types of extrapolation for a single degree of freedom.

These techniques can be used during the simulation phase, as well as in the preload phase when the force is slowly increased over several load increments.

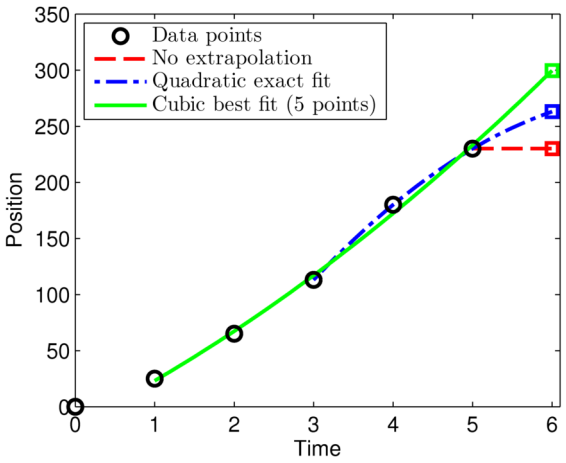

Figure 3.4: Schematic illustrating the different methods for predicting the next solution for a degree of freedom using extrapolation. The circles indicate previous solutions, and the three squares indicate the three different predictions at time = 6. The red line uses the default method of no extrapolation, the blue line uses an exact quadratic fit over three previous solutions, and the green line uses a best cubic fit over five previous solutions. Since an exact cubic fit would take four data points, this last extrapolation corresponds to "Order 3, best fit (+1)" in results presented in Table 3.2.

3.6.2 Modified Newton methods

An additional way to avoid calculating the Jacobian is to keep it constant over several iterations. This will reduce the convergence rate, but make each iteration much less computationally expensive. We use a strategy similar to the "N2" method from Linge et al. (2005), updating the Jacobian when convergence is slow, specifically if convergence is expected to take > 20 iterations given the ratio of the norms of the last two residuals.

3.6.3 Matrix-free solvers

A third way to avoid calculating the Jacobian is the use of Jacobian-Free Newton-Krylov methods which allow for taking a Newton step without requiring the evaluation of a Jacobian. An overview of these methods is given by Knoll and Keyes (2004). They are based on the observation that for a Jacobian at $\mathbf{x}_0$, $\mathbf{J}(\mathbf{x}_0) = \frac{\mathrm{d}\mathbf{f}}{\mathrm{d}\mathbf{x}}(\mathbf{x}_0)$ and vector $\mathbf{x}$, the Jacobian-vector product can be approximated by just one evaluation of $\mathbf{f}$:

$$\mathbf{J}(\mathbf{x}_0)\mathbf{x} \approx \frac{\mathbf{f}(\mathbf{x_0} + h\mathbf{x}) - \mathbf{f}(\mathbf{x_0})}{h} \tag{3.24}$$

When using Krylov subspace methods, the Jacobian appears only in these matrix-vector products, and in GMRES specifically we need only one such product per iteration. A JFNK solver will be more efficient as long as the linear system can be solved within a few hundred GMRES iterations. In practice this is not sufficient to lead to a solution in later Newton iterations, which is likely caused by the fact that there is no simple way to use a preconditioner (Knoll and Keyes, 2004). However, it does often lead to rapid decrease in the residual at the beginning of the solution process. We therefore switch to our normal solver when the JFNK solver fails to reduce the norm of the residual of the linear system by at least 90% within 100 GMRES iterations for 3 consecutive Newton iterations. In the normal Newton solver we calculate the full Jacobian and solve the linear systems using UMFPACK (Davis, 2004).

Both the modified Newton and matrix-free method will generally use more residual evaluations, but with fewer evaluations of the Jacobian. We will test these methods only on 3D problems, where the relative computational cost of evaluating a Jacobian is much greater compared to evaluating a residual.

3.7 Models and results

We also used the fiber model to investigate the performance of the extrapolation methods, by coupling the electrics to a one-dimensional mechanics model with quadratic/linear finite elements and a Mooney-Rivlin constitutive law. Results for a fiber with a fixed left boundary and free right boundary are shown in Table 3.2. These show even simple extrapolation as outlined in section 3.6.1 can lead to large improvements in performance.

In the one-dimensional case, the number of Newton iterations can be further reduced if the residuals for several extrapolated candidate starting points are evaluated and the best one used as the starting point of the solution process. Since in three-dimensional cubic Hermite finite elements, a full Newton iteration is over two orders of magnitudes more expensive than a simple residual evaluation, considering multiple extrapolations and modified Newton iterations is more important. Therefore, we always try several candidate solutions in the three-dimensional case, and present the results by maximum order included.

Order	Exact fit	Best fit (+1)	Best fit (+2)
0	4205	-	-
1	2241	2318	2385
2	1525	1411	1216
3	1499	1159	1343

Table 3.2: Newton iterations required for the 1D fiber problem. Shown are the number of iterations required for 2000 ms of simulation time in the 1D fiber problem, using better initial guesses for the mechanics solution. Best fit (+1) and (+2) use 1 and 2 more previous points than required for an exact fit, respectively.

3.7.1 3D Fiber

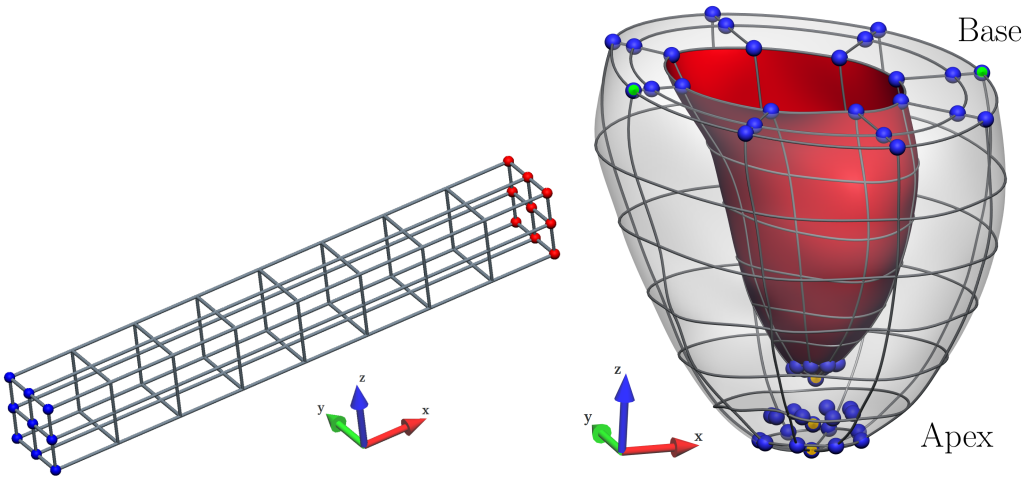

(a) 3D Fiber (b) Left ventricle

Figure 3.5: Problem setup for the three-dimensional models. Panel (a) shows the 3D fiber, with the fixed left side indicated in blue, and the flat side with applied force indicated in red. Panel (b) shows the personalized mesh of a human left ventricle, where the blue nodes have extra stiffness and the blue nodes at the base have boundary conditions on their z position and derivatives to ensure a flat surface throughout the solution process. The position of the rightmost node with a green dot is fixed in the x, y, z directions, while the leftmost one is fixed along the y, z directions. Nodes at the apex with a yellow dot are part of multiple collapsed elements and have their derivatives fixed to zero.

Our first three-dimensional model is that of the $8 \times 1 \times 1$ mm fiber, which we model using 32 tricubic Hermite elements, with the fiber direction along the long axis (see Fig. 3.5(a)). For electrophysiology we keep our regular hexahedral grid with 0.1 mm spacing.

For testing the optimization of our mechanics implementation, we add mechanical boundary conditions: a completely fixed left side, fixed derivatives to give a flat right side $\frac{\mathrm{d}x}{\mathrm{d}\xi_2} = \frac{\mathrm{d}x}{\mathrm{d}\xi_3} = \frac{\partial^2 x}{\partial \xi_2 \partial \xi_3} = 0$, and a 10 kPa force applied at the right end which extends the fiber. Electrical activation for our coupled simulation consist of an intracellular stimulus in the sphere $\|\mathbf{x}\| \leq 0.5$ mm at one corner, to induce a slight bend in the fiber as tension

is generated earlier at this corner. Results for the strain prediction and modified Newton methods are shown in Table 3.3. The JNFK methods can have some impact in the context of non-modified Newton methods, but are ineffective compared to the best results here, and we have not included them in further comparisons.

3.7.2 Human left ventricle

For our next test of the improved mechanics solver, we use a 112 element cubic Hermite mesh of the left ventricle fitted to human patient data (Lamata et al., 2010) (see Fig. 3.5(b)). Fiber directions with transmural and apex-to-base heterogeneity were automatically generated based on data by Usyk et al. (2000). For boundary conditions we fix the base to be fixed and flat in z, fix one node on epicardium at the base completely, and fix the one on opposite side in just the y position. We also fix all derivatives to be 0 for the three nodes at the apex, and apply a constant 1 kPa cavity pressure. Furthermore, we increase the stiffness for the nodes at the base by doubling C_1 (and interpolating the constitutive parameters linearly within elements), to account for the interaction with the rest of the heart, as well as near the apex as in Nickerson et al. (2005). We use Gaussian integration, which avoids determining any quantities at the singularity in fiber directions at the apex. The relatively course hexahedral electrophysiology grid was generated regularly spaced in the mechanics finite elements reference space and consist of 3.98 million nodes spaced at most 0.5 mm apart. We increase the conductivity to compensate for the course grid and stimulate in a 4 mm high section in the middle of the heart (see figure 3.6). The main purpose of the model is as a numerical testbed rather than a clinically relevant tool, and to show that results on a realistic geometry can be quite different compared to simple geometries applied in other studies. The resulting number of Newton iterations, Jacobian evaluations and CPU time needed can be seen in Table 3.4.

The results show that modified Newton methods are very effective at reducing the number of Jacobians required in the solution process. As these are computationally intensive to obtain, this method decreases CPU time by as much as a factor 100 in the fiber model, even though the required number of Newton iterations can increase. In all cases, predicting the next solution using extrapolation methods is also effective, further reducing CPU time and the required number of Jacobians, as well as the number of iterations. Combined they result in a 99.6% reduction in the number of Jacobians in the LV problem, resulting in a 98% reduction in computational time, even when the required number of iterations doubles. Fastest simulations in this section took around 7 hours on a single processor, divided between around 86% in solving electrics, 3% in solving mechanics and 11% in coupling routines.

Mod. Newton	JFNK	Extrap.	Iter.	Jac.	CPU (h)
off	off	off	2815	2815	3.08
off	off	on	664	664	0.72
off	on	off	2409	2409	3.11
off	on	on	865	865	1.36
on	off	off	8355	22	0.06
on	off	on	1546	16	0.03

Table 3.3: Results for the 3D fiber problem. Shown are the total number of Newton iterations, Jacobians calculated, and CPU time of the mechanical part for 10 preload steps and 1000 solver steps of 1 ms each in solving the 3D fiber problem, with a tolerance $\|\text{residual}\| < 10^{-5}$. The experiments with modified Newton "on" use the "N2" method from Linge et al. (2005), JFNK 'on' start the solution process with a Jacobian-free Newton-Krylov solver before switching to a normal solver when convergence slows down, and extrapolation "on" tests several extrapolated solutions, and use the one with the lowest residual as the starting point for the solution process, including exact fits up to cubic, and quadratic and cubic best fits over five previous solutions, as in the quadratic best fit (+2) and cubic best fit (+1) in Table 3.2.

Mod. Newton	Extrap.	Iter.	Jac	CPU (h)
off	off	3155	3155	15.15
off	on	894	894	6.12
on	off	18430	27	0.51
on	on	6385	12	0.28

Table 3.4: Results for the human left ventricle problem. Shown are the total number of Newton iterations for 100 preload steps and 1000 time steps of 1 ms each in solving the human left ventricle problem, with the same setup as used in the experiments from Table 3.3.

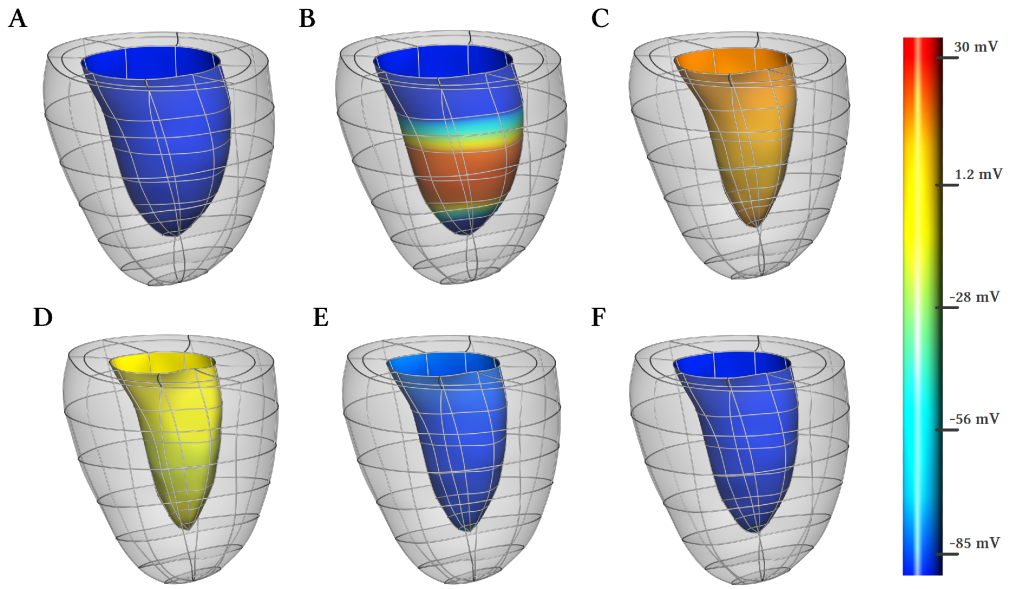

Figure 3.6: Results for the human left ventricle problem. Panels A-F show the deformation and electrical activity on the endocardium at $0, 25, 125, 225, 325, 425$ ms simulation time respectively. The stimulation site can be seen in panel B as the region of early activation.

3.8 Discussion

This chapter presented an integrated set of numerical methods to speed up multiple aspects of solving a strongly coupled electromechanical model, which forms the basis of our electromechanical mouse modelling framework.

Our model includes several feedback mechanisms: influence of sarcomere length on tension, velocity dependent crossbridge kinetics and length- and tension-dependent binding rates. Furthermore, the framework proposed here can readily include stretch-activated channels, whereby mechanical deformation influences the cellular electrophysiology, although there is still significant debate over their basic mechanism (Kohl and Sachs, 2001). This will allow for sufficient flexibility in substituting a different contraction model, regardless of which feedback mechanisms need to be investigated.

For the monodomain model we developed a method which allows a PDE time step of 0.1 ms with no significant impact on conduction velocity and adaptivity which increases this limit. Our cell model integrator complements this solver, as it allows taking similarly large ODE time steps. These methods can be applied in simulating cardiac conduction, as well as both weakly and strongly coupled electromechanical models.

Specifically for electromechanical models we suggested a technique for improving the starting point of the nonlinear solver, by predicting the next solution from the previous ones. These methods were found to be effective on 3D finite element problems, where they can save $70 - 75\%$ of the computational time for mechanics, in a non-modified Newton setting. Use of a modified Newton method which keeps the Jacobian constant over several time steps, changes the impact of the extrapolation methods. They can reduce both the total number of iterations needed and number of Jacobians calculated, but with a lower computational cost in general, the absolute reduction in CPU time is smaller.

Jacobian-free Newton-Krylov methods were also investigated, but were not effective combined with a modified Newton method. This lack of effectiveness of JFNK methods is related to both the ability to re-use the LU factorization when a direct solver is used in a modified Newton method setting, as well as the lower number of residual calculations required, which changes the balance of efficiency such that iterative methods are less competitive.

The impact of these methods on performance depends largely on the size of the heart. The mechanics problem has fewer degrees of freedom, but involves solving a nonlinear system and is more difficult to parallelize. Also, models of smaller hearts (e.g. mice, rats) have approximately the same number of mechanics elements, but far fewer electrophysiology nodes, which makes optimizing the mechanics part of the model relatively more important. On larger hearts, the electrics solution process is an important factor in total runtime. For such larger hearts with dense electrophysiology grids, solving the electrophysiology system on tens of millions of nodes would dominate the solution process even more. This also brings with it a large memory requirement, as storing large linear system and preconditioner and the variables for a complex cell model takes over 45 GB of memory for 32 million nodes. This is a major remaining challenge for running these kind of

simulations without supercomputing power, and the main reason for the coarse grid used in section 3.7.2. However, for work on smaller mouse hearts in the following chapters, performance of the monodomain solver is less relevant, and the improved numerical methods for mechanics will translate directly into significant speedup.

There are also a number of weaknesses in our current approach which were revealed in using this framework. Although the monodomain solver performs adequately for our purpose, it has a weakness that was revealed by later research. When tested in a benchmark of monodomain solvers (Niederer et al., 2011b), it was revealed that although convergence of the solver with respect to larger time steps is good, other numerical methods have better spatial convergence properties. This seems to be related in part due to the choice of mass lumping (Pathmanathan et al., 2012). Using $\bar{\boldsymbol{M}}$ only for speeding up the adaptivity criterion, and using the full matrix in the discretization, would lead to improved spatial convergence properties without significant loss of efficiency. Furthermore, although specialized cell model solvers, such as the one we developed for the GPB model, can be very efficient, they can take some effort to develop and don't generalize to other families of models, including the mouse electrophysiology model used in the next chapter.

Finally, the use of truncated left ventricular models leads to some ambiguity with respect to the boundary conditions at the base. The determination of an optimal choice for these mechanical boundary conditions remains a challenge. Previous solutions have included similar increased stiffness (Nickerson et al., 2005), a fixed base plane (Keldermann et al., 2010) or epicardium (Niederer and Smith, 2009), and prescribing this boundary based on MRI data (Xi et al., 2011). Prescribing the motion is not an option for our particular simulations, and which of the remaining choices leads to more accurate predictions is still unknown.

These appendices expand on some technical details of reducing the GPB model, and parametrizing the contraction model.

3.A Details of simplifying the GPB model

We consider several ways of simplifying the GPB model, making it more efficient for simulating cardiac electrophysiology, using standard techniques from the literature. These simplifications also remove some of the stiffness in the model, which enables effective application of the explicit methods we describe in section 3.2. In all experiments we use the epicardial version of the model, stimulated at $\mathrm{mod}(t, \mathrm{period}) \in [10, 11)$ ms by $I_{\mathrm{app}} = 52$ mV/ms. We use the same notation as in the supplement to Grandi et al. (2010).

3.A.1 QSS formulation of the calsequestrin buffer

The first technique to reduce the number of equations we use involves replacing an equation for a buffer b with maximum capacity b_t for a free concentration c,

$$\frac{\mathrm{d}b}{\mathrm{d}t} = k_{\mathrm{on}} c(b_t - b) - k_{\mathrm{off}} b, \tag{3.25}$$

$$\frac{\mathrm{d}c}{\mathrm{d}t} = f(c, \dots) - \frac{\mathrm{d}b}{\mathrm{d}t}, \tag{3.26}$$

with its quasi-steady state (QSS) approximation $\frac{\mathrm{d}c}{\mathrm{d}t} = \frac{1}{1+\theta} f(c, \dots)$ where $\theta = \frac{b_t K}{(K+c)^2}$ and $K = k_{\mathrm{off}}/k_{\mathrm{on}}$ (see (Keener and Sneyd, 1998) for details).

The rate of change in the calcium concentration in the sarcoplasmic reticulum ($\frac{\mathrm{d}Ca_{SR}}{\mathrm{d}t}$) is given by;

$$\frac{\mathrm{d}Ca_{SR}}{\mathrm{d}t} = J_{serca} - \left(J_{SR_{leak}} \frac{V_{myo}}{V_{sr}} + J_{SR_{Carel}} \right) - \frac{\mathrm{d}C_{sqn_b}}{\mathrm{d}t} \tag{3.27}$$

Where J_{serca}, $J_{SR_{leak}} \frac{V_{myo}}{V_{sr}}$, $J_{SR_{Carel}}$ are calcium fluxes in and out of the sarcoplasmic reticulum and C_{sqn_b} is the concentration of calcium bound to calsequestrin in the sarcoplasmic reticulum. By applying a rapid buffering approximation this equation is changed to:

$$\frac{\mathrm{d}Ca_{SR}}{\mathrm{d}t} = \frac{1}{1 + \theta_{csqn}} \left(J_{serca} - \left(J_{SR_{leak}} \frac{V_{myo}}{V_{sr}} + J_{SR_{Carel}} \right) \right) \tag{3.28}$$

Where $\theta_{csqn} = \frac{B_{max_{csqn}} K_{csqn}}{(K_{csqn} + Ca_{SR})^2}$ and $K_{csqn} = k_{off_{csqn}}/k_{on_{csqn}}$, where $k_{on_{csqn}}, k_{off_{csqn}}$ are the binding and unbinding rates of calcium to calsequestrin and $B_{max_{csqn}}$ is the maximum buffer capacity.

3.A.2 Fixed sodium concentrations

Another technique is to set concentrations which do not vary much over a single cardiac cycle to be constant. There are 5 variables which describe sodium concentrations in the cytosol, junctional cleft and subsarcolemmal space, as well as buffers in the junctional

cleft and subsarcolemmal space. However, none of these vary sufficiently over the course of a single action potential to have a large impact on model predictions. The intracellular sodium concentrations vary little over the course of a single beat (Na_i changes less than $<$ 0.1%), and can be set to a constant value. For this change we set $\frac{dNa_i}{dt} = \frac{dNa_j}{dt} = \frac{dNa_{sl}}{dt} = 0$ and remove equations for their buffers Na_{B_j} and $Na_{B_{sl}}$. We set the concentrations to a constant value, after pacing the model at a certain frequency for 100 beats. Differences after eliminating these equations are small (Table 3.5, row " Fixed sodium"), including only a 0.15 mV higher membrane potential during upstroke and 0.3 ms slower repolarization.

3.A.3 Myo and TnCh calcium buffers

Similarly, buffering to myosin and high-affinity binding site of troponin also has a limited effect. Replacing the buffers by algebraic equations using a quasi-steady state assumption is not possible due to the low binding rates, so we choose to completely eliminate these buffers from the model, setting the equations for them to $\frac{dMyo_c}{dt} = \frac{dMyo_m}{dt} = \frac{dTnC_{h_m}}{dt} = \frac{dTnC_{h_c}}{dt} = 0$. Differences in Table 3.5 (rows "No TnCh buffers" and "No Myo buffers") show that removing the extra troponin buffers has the largest effect and removing the myosin buffers has a smaller additional effect on the calcium transient. In later sections any mention of the concentration of calcium ions bound to troponin C ($[Ca^{2+}]_{Trpn}$) refers exclusively to the low-affinity binding site which drives contraction.

3.A.4 Quasi-steady state formulation of the subsarcolemmal and junctional buffers

The last change involves fast buffering approximations to some of the subsarcolemmal and junctional buffers This change is applied much like the formulation of the calsequestrin buffer. Define:

$$K_{sll} = k_{off_{sll}}/k_{on_{sll}} \tag{3.29}$$

$$\theta_{sll_j} = \frac{B_{max_{SLlowj}} K_{sll}}{\left(K_{sll} + [Ca^{2+}]_j\right)^2} \tag{3.30}$$

$$K_{slh} = k_{off_{slh}}/k_{on_{slh}} \tag{3.31}$$

$$\theta_{slh_j} = \frac{B_{max_{SLhighj}} K_{slh}}{\left(K_{slh} + [Ca^{2+}]_j\right)^2} \tag{3.32}$$

$$\frac{d[Ca^{2+}]_j}{dt} = J_{[Ca^{2+}]_j} - \frac{dSLH_j}{dt} - \frac{dSLL_j}{dt} \tag{3.33}$$

Where we define $J_{[Ca^{2+}]_j}$ as all the fluxes in and out of the junctional cleft unrelated to buffering.

The model we use only makes the assumption of a quasistatic state for the SLL buffer, using $\frac{dSLL_j}{dt} = \theta_{sll_j}\frac{d[Ca^{2+}]_j}{dt}$ to end up with:

$$\frac{d[Ca^{2+}]_j}{dt} = \frac{1}{1+\theta_{sll_j}}\left(J_{[Ca^{2+}]_j} - \frac{dSLH_j}{dt}\right) \tag{3.34}$$

Further applying the quasistatic formulation of the SLH buffer $\frac{\mathrm{d}SLH_j}{\mathrm{d}t} = \theta_{slh_j}\frac{\mathrm{d}[\mathrm{Ca}^{2+}]_\mathrm{j}}{\mathrm{d}t}$ gives the formulation for both buffers eliminated, which is:

$$\frac{\mathrm{d}[\mathrm{Ca}^{2+}]_\mathrm{j}}{\mathrm{d}t} = \frac{1}{1+\theta_{sll_j}+\theta_{slh_j}} J_{[\mathrm{Ca}^{2+}]_\mathrm{j}} \tag{3.35}$$

However, we did not use this formulation as it results in larger changes in key variables. Equivalent changes can be applied to the subsarcolemmal space (subscripts j replaced by sl in equations). This results in slightly lower peak concentrations in these compartments, resulting in slightly lower peak $[\mathrm{Ca}^{2+}]_\mathrm{i}$ as can be seen in Table 3.5 ("QSS SLL buffers").

Applying the same technique to the high-affinity buffers in these compartments, or to the ryanodine subsystem (as in the TP model, where a similar model reduction was performed (ten Tusscher and Panfilov, 2006)) results in significant changes in peak $[\mathrm{Ca}^{2+}]_\mathrm{i}$ timing, because of the slow ($1/k_\mathrm{off} \approx$ 15-30 ms) time scales involved, so we have left the original formulations unchanged.

Simplification	#ODE	APD_{90}	Peak $[\mathrm{Ca}^{2+}]_\mathrm{i}$	Peak $[\mathrm{Ca}^{2+}]_\mathrm{Trpn}$
QSS CSQN buffer	37	-	+0.06%	+0.03%
Fixed sodium	32	+0.3 ms	+0.19%	+0.05%
No TnCh buffers	30	+0.7 ms	+1.2%	+0.8%
No Myo buffers	28	+0.7 ms	+1.4%	+1%
QSS SLL buffers	26	+0.6 ms	+1.5%	+1%

Table 3.5: Differences for important variables in the GPB model after reducing the number of equations. #ODE indicates the number of ordinary differential equations in the reduced models. All differences are compared to the original model, at 1 Hz pacing.

3.B Parametrization of the contraction model

This section describes in detail the re-parametrization of the NHS rat contraction model to represent human muscle. Currently available experimental data are insufficient to fully reparametrize the model, but does allow us to fit the most important parameters to give sufficiently physiological whole-organ function to test our solution methods. We start by adding the tension-dependent unbinding of Ca^{2+} from troponin C from the NHS model to the GPB model, by introducing a tension dependence in the troponin C unbinding coefficient within the GPB model:

$$k_\mathrm{off} = k_\mathrm{refoff} \cdot \max\left(0.1, 1 - \frac{T_a}{\gamma T_\mathrm{ref}}\right) \tag{3.36}$$

We keep the original value of γ, and now need to estimate k_refoff, taking into account the lower tension-dependent unbinding at higher levels of tension. Assuming $\frac{\mathrm{peak}\ T_a}{T_\mathrm{ref}} \approx \frac{27}{56.2}$ at $\lambda = 1$ as in the original model, and assuming the single cell values reflect isometric tension, we can define a simple tension curve with this $\frac{\mathrm{peak}\ T_a}{T_\mathrm{ref}}$ and approximate time to

peak and relaxation of tension. Using this as input to our coupled model, we estimated k_{refoff} as 5% higher than the GPB value of k_{off}, at which the tension-dependent $[Ca^{2+}]_{\text{Trpn}}$ curve is a good match for the original one of the GPB model.

Values of peak tension during a twitch from experimental data vary around $20 - 50$ kPa in single cells generating maximum tension (Mulieri et al., 1992; Pieske et al., 1996). We use a reference tension of $T_{\text{ref}} = 100$ kPa, which has been shown to be consistent with whole-organ contraction(Niederer and Smith, 2009). This corresponds to around 45 kPa peak tension in an isometric twitch at resting sarcomere length.

Next, we determine the Hill coefficient, which determines the steepness of the steady state relationship between force and $[Ca^{2+}]_{\text{i}}$ (Bers, 2001). Force-pCa curves vary depending on sarcomere length and temperature, with Hill coefficients ranging from 2.0-6.5 have been reported in a variety of mammals (Yue et al., 1986; Hunter et al., 1998; Niederer et al., 2006). There is limited data on intact cardiac muscle in humans at body temperature, but Gwathmey and Hajjar (1990) reported a Hill coefficient of around 5 in intact human cardiac muscle at 30 °C, which is consistent with values observed at that temperature in other species. We set the Hill coefficient to $n = 5$ in accordance with the best available data in intact fiber at higher temperatures.

Similar to our process for determining T_{ref}, we set $[Ca^{2+}]_{50}$ to the same fraction of the peak $[Ca^{2+}]_{\text{i}}$ as in the NHS model, resulting in a value of $[Ca^{2+}]_{50} = 0.25$ μM. This is quite low compared to experimental data, which includes $[Ca^{2+}]_{50}$ in ferrets as 0.44μM at 30 °C (Yue et al., 1986) and $[Ca^{2+}]_{50}$ in humans as 0.58μM at 30 °C (Gwathmey and Hajjar, 1990). However these comparisons are made in the context of the general lack of data for intact human cardiac muscle at body temperature, and this low value is also a direct consequence of peak $[Ca^{2+}]_{\text{i}}$ in the GPB model, which is at the lower end of experimentally observed values. For coupling to other electrophysiology models this parameter should be adjusted according to peak $[Ca^{2+}]_{\text{i}}$.

Removal of the cooperative unbinding term in the equation for actin binding ($\alpha_{\text{r2}} = 0$) gives a tension transient that can not both reach a high maximum and relax to low levels of tension, which shows the importance of this term. Including the half-activation value K_z for cooperative unbinding in optimization results in a very low K_z, since this adds a constant unbinding factor which makes it easier to achieve better relaxation. However, this is also highly unrealistic. Setting $K_z = 0.1$ is sufficient to give better relaxation overall, so we do not include in further optimization. We are left with three free parameters, the binding and unbinding rates α_0, α_{r1} and α_{r2}. To constrain our optimization we use a common measure of how reaction rates in biological systems change when temperature increases, known as the Q10 value:

$$\text{Q10} = \left(\frac{R_2}{R_1}\right)^{10/(T_2 - T_1)} \tag{3.37}$$

Where R_1, R_2 are the reaction rates at temperatures T_1, T_2. For biological systems, the Q10 value is generally between 1 and 3, which corresponds to a maximum 270% increase when changing the temperature from 25 °C to 37 °C. Using simulated annealing to fit

the parameters to experimental data for time to peak tension (TPT), and time to 50% and 95% relaxation (RT_{50}, RT_{95}), as well as low levels of resting tension, restricted to these Q10 values, we arrive at values shown in Table 3.6, which show consistent Q10 values across all three parameters. These values give a peak tension of 46.3 kPa, tension at 990 ms after activation of 1.9 kPa, and relaxation times consistent with experimental data, as shown in Table 3.7 ("Reparametrization"). Fig. 3.2 shows the resulting tension transient for an isometric twitch in a single cell.

Parameter	T_{ref}	$[Ca^{2+}]_{50}$	α_0	α_{r1}	α_{r2}	K_z
Original	56.2 kPa	1.05 µM	8/s	2/s	1.75/s	0.15
Reparametrization	100 kPa	0.25 µM	22.3/s	5.2/s	4.6/s	0.10
Q10			2.3	2.2	2.2	

Table 3.6: New parameters for the NHS active contraction framework. Shown are the parameters we use to simulate human cells at body temperature. Note that Q10 values only apply to binding rates.

Source	TPT (ms)	RT_{50} (ms)	RT_{95} (ms)
Mulieri et al. (1992)	157 ± 10	117 ± 8	-
Pieske et al. (1996)	165 ± 7	116 ± 6	334 ± 43
Reparametrized coupled model	146	123	330

Table 3.7: Tension development in isometric twitch. Shown are the time to peak tension (TPT) from onset of tension and time to 50% (RT_{50}) and 95% (RT_{95}) relaxation from peak tension. For the models we use a rate of increase in tension greater than 0.01 kPa/ms as threshold to detect onset of tension, and measure RT_{50}, RT_{95} as the time when tension decays below $50\%, 95\%$ of the difference between peak tension and minimum tension for 1 Hz pacing.

Chapter 4

Electromechanical modelling of the mouse heart

As outlined in the introduction, genetically modified mice are increasingly being used to investigate the biophysical underpinnings of cardiac mechanics. However, computational models have lagged behind this move to using mice as the standard experimental animal. Furthermore, many cardiac models lack species and temperature consistency, which creates limitations in their use in interpreting experimental data.

The use of heterogeneous data is indicative of challenges in identifying model parameters from only cell measurement data. Specifically, many contraction experiments are done at lower temperatures (Stull et al., 2002) or in skinned preparations, which (as discussed in Chapter 2) are known to significantly affect results. Even in intact preparations at body temperature, maximal active tension at the cellular level is typically significantly less than seen in tissue, and decreases over tens of seconds in conditions of saturated calcium concentrations (Campbell, 2011).

These difficulties with single cell data further confound our ability to make quantitative connections between detailed measurements at the cellular scale, and whole organ function observed in vivo. Translating between these measurements is a challenge, as there are significant differences between measurements of single cell tension transients and ventricular pressure. Single cell tension tends to be more asymmetric, with longer relaxation, compared to the more symmetric pressure transients (e.g. compare Figures 4.5 and 4.11). These differences are most likely to be a result of length- and velocity dependent feedback on cellular contraction. However, their relative effect on whole organ function can be difficult to measure, due to the difficulties with cellular data, as well as the controversies that exist over the biophysical mechanisms (cf. sections 2.2.7.1 and 2.2.7.2). This has led to the use of phenomenological tension models being used at the whole organ scale (e.g. (Sermesant et al., 2006)), for reproducing realistic ventricular pressure transients in the absence of detailed knowledge of the coupling mechanisms involved.

In this chapter our goal is to address these challenges through the development of an electromechanical mouse model at 37°C and a physiological 6-8 Hz heart rate. This model provides an important opportunity to integrate data which is increasingly becoming

available in both normal and transgenic mice, and using it towards a better quantitative understanding of cardiac function, both specifically in this common experimental model, and ultimately in other species.

The next section describes our new contraction model for murine cardiomyocytes at 37°C, which is based primarily on experimental data obtained under physiological conditions, and is able to represent fast murine contraction kinetics. This cellular model is extended to the whole-organ scale in section 4.2 supported by data from the literature as well as MRI and pressure-volume measurements, and passive inflation on isolated hearts. We also look at the issue of model parametrization in detail in both single-cell and whole-organ contexts, with the goal of providing clarity about the degree of confidence in these parameters given the experimental data constraining them. Firstly, we investigate the identifiability of the cell model parameters in the section 4.1.4 by using a novel visualization which relates constraints given by experimental data to the model parameter space. Secondly, we use our electromechanical model to perform a comprehensive sensitivity analysis and an investigation of coupling mechanisms in sections 4.3. Finally we use this framework in section 4.4 to compare in-silico experiments with recent experimental data and provide an analysis of deformation dependent electromechanical coupling mechanisms. Through this model analysis our goal is to quantify the effects of the deformation dependent coupling mechanisms underlying the shape of ventricular pressure transients.

4.1 Cellular modelling

For our contraction model we have aimed to strike a balance between modelling detail and ability to parameterize the model using available data. The model is primarily based the two previously published models discussed in section 2.2.8, both of which have been used before in a whole organ context.

The first of these is the model developed by Niederer, Hunter, and Smith (2006) ("NHS model") , which has a relatively simple structure and has clear procedures for determining most of its parameters. However, the model is unable to capture the faster relaxation kinetics of mouse cardiac muscle at higher pacing frequencies.

The second model published by Rice et al. (2008a), provides a more detailed four state Markov model of the sarcomere, incorporating troponin, tropomyosin and crossbridge kinetics. The processes for determining its many parameters are less clear, as are their uniqueness with respect to the fitting methods used. However, the model reproduces a wide variety of experimental data, and is better able to capture the faster kinetics of contraction. Both models are also primarily based on experimental data obtained under nonphysiological temperatures ranging between 15-25°C at a 1 Hz stimulation frequency in animals which have physiological heart rates in the 6-10 Hz range. Figure 4.1 shows an overview of the cell model and interaction with the tissue scale. This model has also been made available in the CellML repository*.

*`http://models.cellml.org/e/e4/`, `http://models.cellml.org/w/dcowan/Land_et_al_2012`

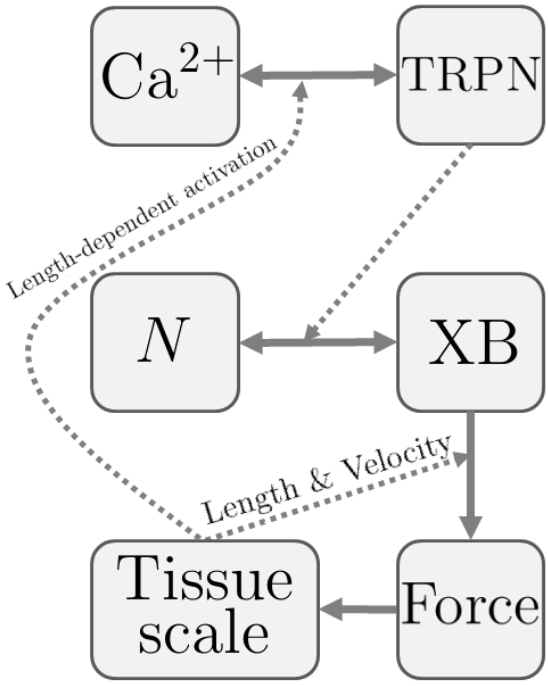

Figure 4.1: Cell model overview. Calcium binds to troponin C (TRPN) in a cooperative way. This increases XB, the fraction of actively cycling crossbridges. Length- and velocity dependencies are added to calculate the force generated, which is used at the tissue scale.

4.1.1 Electrophysiology

At the basis of contraction lies the change in intracellular calcium, for which we use the data-driven C57BL/6 mouse model developed by Li et al. (2011) based partly on experimental data from Andersson et al. (2009a). The only change we have made to this model is a reparametrization of the ryanodine receptors to $A_{P_{\mathrm{RyR}}} = -0.08$, to better match experimental data for time to peak of the calcium transient. The new calcium transient after setting $A_{P_{\mathrm{RyR}}} = -0.08$ and pacing the model at 6 Hz is shown in Figure 4.2, and has time to peak, decay profile, and diastolic calcium all in the range of experimental data. Changes in action potentials between the old and new choice of $A_{P_{\mathrm{RyR}}}$ differ by at most 0.3 mV.

4.1.2 Troponin binding

Active tension is initiated by calcium binding to the second calcium binding site on troponin C (TnC). There is significant evidence that shows that this reaction is cooperative with a Hill coefficient of 1.6-2.0 in experiments on isolated bovine and human actin filaments (Davis et al., 2007; Gillis et al., 2000; Tobacman and Sawyer, 1990). This is further supported by recent data from Kreutziger et al. (2011), who show that different single amino acid variants of TnC can have a significant effect on the steepness of the force-calcium relationship in mice. Our model of troponin binding captures this cooperativity

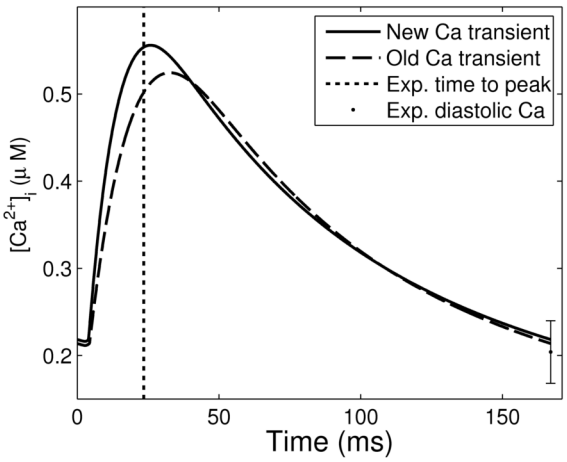

Figure 4.2: Calcium transient for the electrophysiology model paced at 6 Hz. Figure shows the original $A_{P_{\mathrm{RyR}}} = -0.04$ transient, new $A_{P_{\mathrm{RyR}}} = -0.08$ transient, experimental time to peak calcium, and experimental diastolic calcium levels.

using a standard cooperative binding equation which has a Hill curve as its steady state solution:

$$\frac{\mathrm{dTRPN}}{\mathrm{d}t} = k_{\mathrm{TRPN}} \left(\left(\frac{[\mathrm{Ca}^{2+}]_{\mathrm{i}}}{[\mathrm{Ca}^{2+}]_{\mathrm{T50}}} \right)^{n_{\mathrm{TRPN}}} (1 - \mathrm{TRPN}) - \mathrm{TRPN} \right). \tag{4.1}$$

Where TRPN represents the fraction of occupied regulatory sites, k_{TRPN} the unbinding rate, and n_{TRPN} the Hill coefficient. We use $n_{\mathrm{TRPN}} = 2$ because of the higher temperature and increase in cooperativity with temperature observed in mice (Blanchard et al., 1999), and $k_{\mathrm{TRPN}} = 0.1/\mathrm{ms}$ based on Davis et al. (2007) (15°C, isolated reconstituted filaments from mixed bovine/human/rat proteins). While this k_{TRPN} value was determined at lower temperature, it does not have a clear temperature dependence (Niederer et al., 2006; Little et al., 2012) and the current value is high enough to reproduce experimental measurements of force at a 6 Hz stimulation frequency. The value of $[\mathrm{Ca}^{2+}]_{\mathrm{T50}}$, the calcium concentration needed for 50% bound TnC in steady state, can be taken directly from K_d values obtained in experiments ($K_d = ([\mathrm{Ca}^{2+}]_{\mathrm{T50}})^{n_{\mathrm{TRPN}}}$). However, such measurements are also typically obtained at lower temperatures, and is inconsistent between different sources. Davis et al. (2007) gives $K_d \approx 5$, which results in significantly reduced activation for physiological calcium transients. Gillis et al. (2000) give $[\mathrm{Ca}^{2+}]_{\mathrm{T50}} > 3\mu\mathrm{M}$ at 37°C, with a shift of 0.13 pCa units from 21°C to 37°C in bovine preparations. Tobacman and Sawyer (1990) report $[\mathrm{Ca}^{2+}]_{\mathrm{T50}} \approx 1\mu\mathrm{M}$ at 25°C in bovine thin filaments. Applying a $0.13 \cdot (37 - 25)/(37 - 21) \approx 0.1$ pCa shift to this gives $[\mathrm{Ca}^{2+}]_{\mathrm{T50}} \approx 0.8\mu\mathrm{M}$, which was deemed a more plausible value considering our calcium transient.

As discussed previously in section 2.2.7.1, there have also been suggestions of cross-bridge binding affecting the unbinding rate of calcium from TnC. However, more recent

work suggests this effect appears only under rigor conditions, and is not significant under physiological conditions (Sun et al., 2009; Farman et al., 2010). For this reason we have not included it in the model. Furthermore, the troponin buffer can be either strongly or weakly coupled to the intracellular calcium, depending on whether binding directly affects intracellular calcium. In the previous chapter we coupled our troponin buffer strongly, as there was an equation for the troponin concentration already present in the electrophysiology model. However, since the Li et al. model of electrophysiology includes only a quasi-steady state buffer for cytosolic calcium, unlike the Grandi et al. model which has more detailed buffering equations. The quasi-steady state buffer represents a combination of several buffers present in the cell, and the total concentration of these individual buffers (including troponin) is unknown. Therefore we have chosen to keep the original formulation, and couple only weakly between our electrophysiology and mechanics models.

4.1.3 Tropomyosin/crossbridge kinetics

The process of calcium binding to TnC causes a conformational change in its associated tropomyosin complex, unblocking the actin sites for myosin crossbridge cycling.

These mechanisms can be described using many states and parameters, although there are not nearly enough experimental data to parametrize such models. However, it is still useful to relate our simpler model to a more detailed description of the underlying biophysical mechanisms. As described in section 2.2.8, the six-state model of McKillop and Geeves (1993) described the mechanisms of contraction using a blocked, closed and open state of tropomyosin along with weakly, strongly or unbound crossbridges. While both the open and closed states allow for weak binding of myosin crossbridges, only the open state allows for transition to the force-generating strongly bound state. Assuming the open and closed states are in rapid equilibrium, this reduces to a four-state model as in Rice et al., with tropomyosin kinetics and a crossbridge cycle.

Due to the scarcity of experimental data and the intrinsic difficulties of measuring the details of subcellular processes, we further reduce this model by collapsing the crossbridge cycle to a single state, which leaves the model with the following two states. The first state is the crossbridge state XB, in which the crossbridge is actively cycling. A constant fraction of these is considered to be in weakly/strongly/unbound states. The second state is the nonpermissive state $N = 1 - \mathrm{XB}$.

As the crossbridge cycle is not faster than tropomyosin kinetics, this reduction will only be reasonable for sufficiently slowly changing calcium, as is physiological. The model is less suitable for reproducing other features such as the response to fast step changes in calcium.

The equation for transition between these two states is also chosen to give a Hill curve at steady state. There are several functions which give such a steady state which have been used previously. These include as cooperativity only in the binding rate (Niederer et al., 2006) or a division of cooperativity between the binding and unbinding rates (Rice et al., 2008a). Since there are insufficient data about subcellular mechanisms to distinguish between these two possibilities, we tested both in a simulation study. Using the division

of cooperativity results in a 10 ms reduction in RT_{90} and halves tension at the end of a twitch without significantly affecting time to peak tension, resulting in an improved fit for the twitch transient compared to experimental data (Stull et al., 2002).

We choose our nonlinear function to ensure $TRPN_{50}$ has a clear interpretation, i.e. $XB(TRPN = TRPN_{50}) = 0.5$ at steady state, resulting in:

$$\begin{aligned} \frac{dXB}{dt} &= k_{xb}\left(\text{permtot}\ (1 - XB) - \frac{1}{\text{permtot}}XB\right) \\ \text{where permtot} &= \sqrt{\left(\frac{TRPN}{TRPN_{50}}\right)^{n_{xb}}}. \end{aligned} \tag{4.2}$$

We set $k_{np} = 0.1, n_{xb} = 5$ in accordance with time to peak and Hill coefficient measurements (Blanchard et al., 1999; Stull et al., 2002), and $TRPN_{50} = 0.35$ to obtain a peak XB of around 1/3 which leaves sufficient room for length-dependent activation, and is consistent with levels typically seen in force-calcium loops (Stull et al., 2002).

These parameters result in a force-pCa Hill fit with coefficient of 6.7, compared to 6.68 ± 0.63 at 37°C from experimental data (Blanchard et al., 1999). A biphasic Hill fit (McDonald and Moss, 1995) results in Hill coefficients of 8.3 and 4.1 for the lower and upper part of the curve, respectively, as shown in Figure 4.3. Such different Hill coefficients have been observed previously in experiments (McDonald and Moss, 1995; Dobesh et al., 2002; Rice and de Tombe, 2004), and have previously been attributed to slower rates of crossbridge cycling at higher saturation (Dobesh et al., 2002). However, we found that this effect is to some extent even present in a simple $[Ca^{2+}]_i$/TnC model, where the Hill coefficient in their lower part of the Hill curve is approximately 50% higher compared to the upper half when fit separately. Introducing cooperative binding of calcium to TnC increases this effect to the magnitude observed in experiments, with the lower part of the Hill curve having double the Hill coefficient compared to the upper half.

The model's response for tension generation and relaxation is shown in Table 4.1, where it is compared to experimental data.

4.1.4 Parameter sensitivity and identifiability

The two stages of cooperative binding in the model introduces pairs of parameters, some of which may be highly coupled and thus problematic to distinguish during fitting: the sensitivities $[Ca^{2+}]_{T50}, TRPN_{50}$, binding rates k_{TRPN}, k_{xb}, and Hill coefficients n_{TRPN}, n_{xb}. To determine the effect of this coupling on model parametrization, as well as how new experimental data could help improve it, we performed a parameter sensitivity analysis. We vary the pairs of parameters to identify the regions in which $RT_{50} \in [19, 25], RT_{90} \in [45, 55], TPT \in [30, 41], \max XB(t) \in [0.3, 0.4], XB(t = 167\text{ms}) < 0.01$. The Hill coefficients are further limited by the resulting Hill fit of the steady state force-pCa curve to $[6, 7.5]$. We visualize the regions in which these constraints are met for each pair of parameters. The "viable" region for a pair of parameters can then be identified as the intersection of these individual constraints, and its boundaries show which experimental data best constrains which parameters.

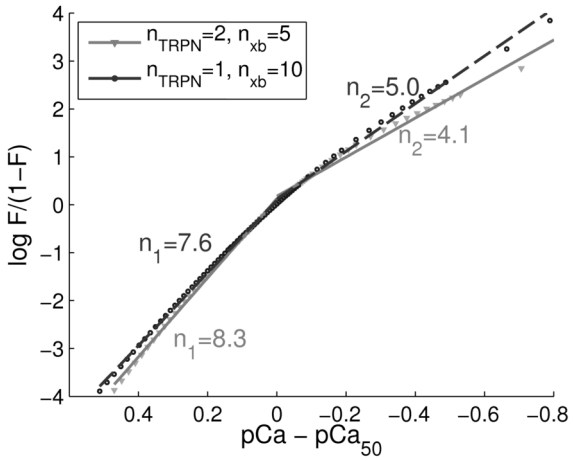

Figure 4.3: Biphasic Hill fits to model force-pCa response. A best linear fit of $\log F/(1-F)$ to pCa was applied separately for the upper and lower halves. The Hill coefficient n_{xb} for the $n_{\mathrm{TRPN}} = 1$ case was chosen to ensure the Hill coefficient fit for the entire curve matched the $n_{\mathrm{TRPN}} = 2$ case.

Source	TPT	RT_{50}	RT_{90}	Experiment, muscle, pacing
Andersson et al. (2009a)	33.5 ± 0.5			US, isolated myocytes, 6 Hz
Stull et al. (2002)	~ 35	22 ± 3	~ 45	IT, trabeculae, 6 Hz
Stull et al. (2006)		24 ± 2		IT, trabeculae, 6 Hz
Bluhm et al. (1999)	~ 30	~ 27	~ 60	IT, LV papillary, 6 Hz
Bluhm et al. (2000)	37 ± 2	35 ± 2		IT, LV papillary, 6 Hz
Stuyvers et al. (2002)	~ 40	~ 30	~ 50	IT, RV trabeculae, 5 Hz.
Palmer et al. (2004b)	$\sim 41/37$		$\sim 55/38$	IT, RV trabeculae,4/10 Hz
Model results	36	23	49	

Table 4.1: Experimental data compared to model results for isometric twitch tension. TPT is time to peak tension from onset of tension in ms, except for Andersson et al. where it indicates time to peak shortening. RT_{50}, RT_{90} refer to time to 50% and 90% relaxation in ms. US refers to an unloaded shortening experiment, IT to an isometric twitch experiment, and RV, LV to right- and left-ventricular. All data are from mice at 37°C or 37.5°C. The $\sim$ symbol indicates an approximation obtained from twitch transient graphs or bar charts shown in sources.

Results for the sensitivities are shown in Figure 4.4 (A). These confirm the high degree of coupling between these parameters, constrained by the peak XB and relaxation times. While the viable region spans a wide range of values of either parameter, it is also very narrow, showing that determining one parameter accurately is sufficient for constraining both of them. Panel B shows results for the binding rates. Assuming that both processes happen on a similar time scale, we can see that these rates should be in the range of 0.07-0.15 to obtain realistic tension development and relaxation. Without such an assumption, there is a significant range of viable parameter values. Finally, results for the Hill coefficients are shown in panel C. These parameters are restricted to a fairly narrow window determined by the force-calcium Hill coefficient fit, peak XB, and relaxation kinetics. Overall, evaluating pairs of parameters in this way results in an intuitive visualization of what parameters are well constrained, which experimental data matters most, and where new data can help further constrain the model development process.

4.1.5 Length dependencies

Adding length- and velocity dependent factors to the model, the normalized force including length and velocity dependence is given by:

$$F_n = g(Q) \times h(\lambda) \times \mathrm{XB}. \tag{4.3}$$

Where $g(Q)$ determines the velocity dependence, $h(\lambda)$ the change in maximum force, and λ is the extension ratio along the fiber direction.

Consistent with recent reviews (Hanft et al., 2008; Solaro, 2007), we base the increase in maximum force on filament overlap, modelled using the approach from Rice et al. (2008a), and simplified as:

$$h'(\lambda) = 1 + \beta_0(\lambda + \min(\lambda, 0.87) - 1.87) \tag{4.4}$$

$$h(\lambda) = \max(0, h'(\min(\lambda, 1.2)) \tag{4.5}$$

where $\beta_0 = 1.65$, resulting in a linear length dependence near resting length, and a twice as steep decrease in tension when the sarcomere length falls below the thick filament length (at $\lambda = 0.87$).

As outlined in section 2.2.7.1, a shift in calcium sensitivity is an additional and important mechanism for the length-dependence of tension. As details of the subcellular mechanisms which cause this are still being debated, we use a simple phenomenological representation, where the calcium sensitivity $[\mathrm{Ca}^{2+}]_{\mathrm{T50}}$ is directly length dependent:

$$[\mathrm{Ca}^{2+}]_{\mathrm{T50}} = [\mathrm{Ca}^{2+}]^{\mathrm{ref}}_{\mathrm{T50}} \left(1 + \beta_1 \left(\lambda - 1\right)\right). \tag{4.6}$$

Data from Stull et al. (2002, 2006) shows twitch transient force roughly doubles with a 10% increase in sarcomere length. Having established $h(\lambda)$, the length-dependent activation can be estimated from these data, resulting in $\beta_1 = -1.5$. Figure 4.5 shows the length-dependencies at both steady state and for twitch transients.

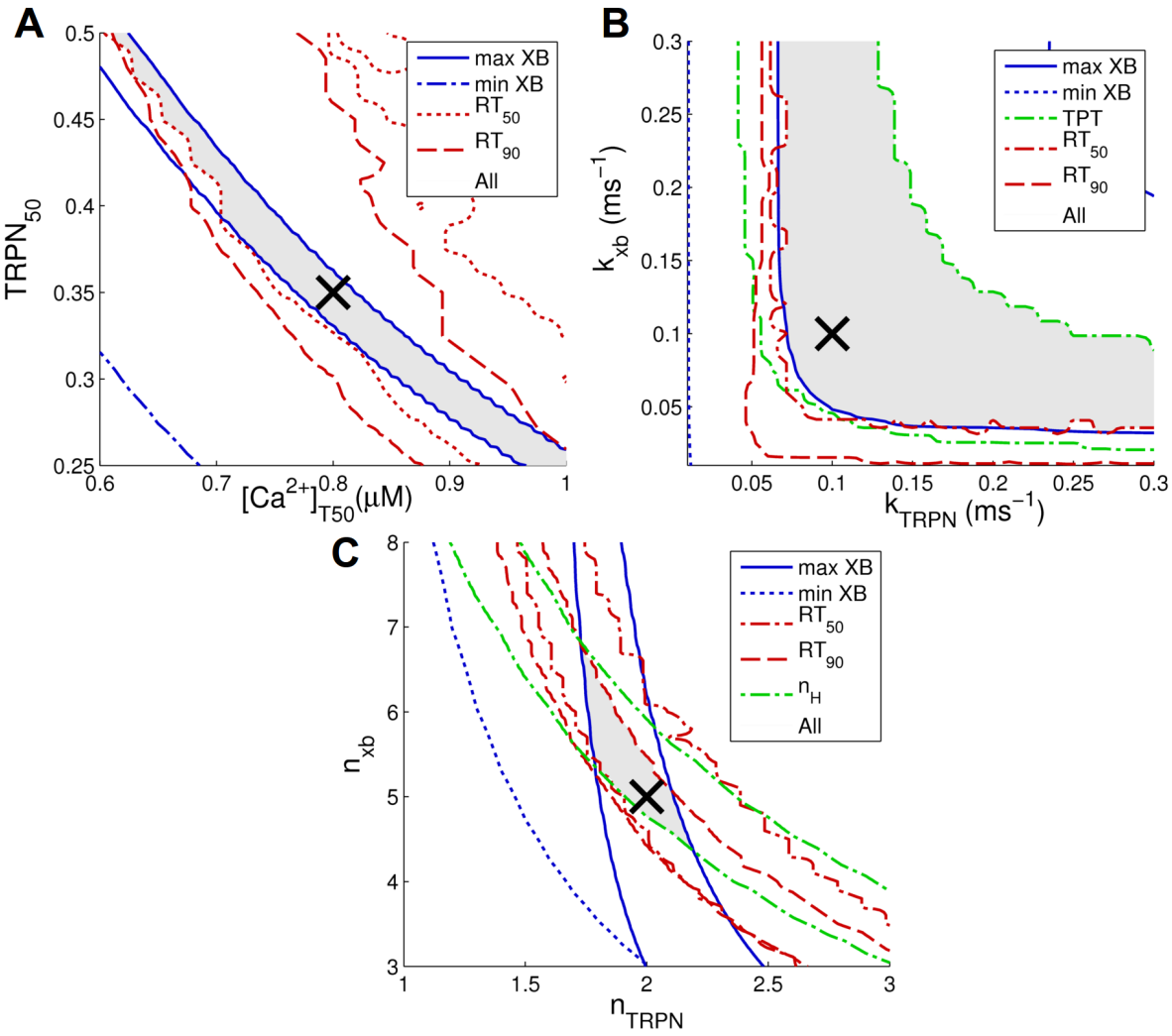

Figure 4.4: Viable regions for pairs of highly coupled parameters. The viable regions are shown as the shaded region as the intersection of all constraints, with lines showing the borders of individual constraints: 'max XB' is the maximal value of XB in a beat, 'min XB' is the minimal value of XB in a beat, 'TPT' is the time to peak tension, 'RT_{50}' as the time to 50% relaxation, 'RT_{90}' as the time to 90% relaxation. The ranges for these constraints are given in section 4.1.4. Our final choice of model parameters is indicated by 'X' in the figures. Panel A shows the parameter sensitivity for $[Ca^{2+}]_{T50}$ and $TRPN_{50}$. The time to peak does not limit parameters within these ranges, and has been omitted from this visualization. The 'max XB' constraint is most influential in limiting the range of possible parameter choices. Panel B shows the parameter sensitivity for k_{TRPN} and k_{xb}. Many of the constraints limit these parameters from below, while only the time to peak tension is influential in setting an upper bound. Panel C shows the parameter sensitivity for n_{TRPN} and n_{xb}. The time to peak curve was omitted in this panel as well, to improve the visualization as it does not contribute to restricting the parameters. A further constraint n_H, representing the Hill coefficient fit of the complete model, was also included here. The 'max XB', RT_{90} and n_H constraints combined result in a clear region in parameter space for these two parameters.

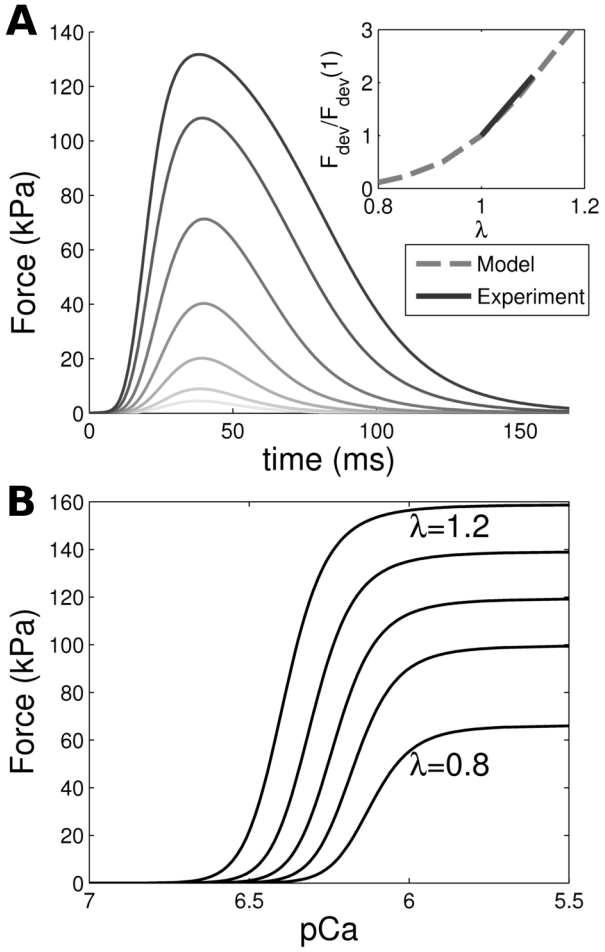

Figure 4.5: Length-dependence of tension. Panel A shows twitch transients at various sarcomere lengths ($\lambda = 0.8, 0.85, 0.925, 1, 1.075, 1.15, 1.2$ from bottom to top, where the extension ratio $\lambda = \frac{\text{SL}}{\text{resting SL}}$). The maximum force F_{dev} is compared to experimental data in inset. Panel B shows force-pCa curves for different extension ratios ($\lambda = 0.8, 0.9, 1.0, 1.1, 1.2$ from bottom to top).

There are significant differences between models with regards to the relative importance of the change in maximum force and length-dependent activation such as increased calcium sensitivity. For example, our choice of β_0 is significantly smaller than in the NHS model, where $\beta_0 = 4.9$. This balance between the different factors in the length-dependence of tension will be further investigated later in this chapter at the whole organ level.

4.1.6 Velocity dependence

Another well known aspect of cardiac muscle is the velocity dependence of force. As the exact mechanisms involved remain debated (cf. section 2.2.7.2), we use a phenomenological "fading memory" model as in the NHS model, which can reproduce many of the observed effects without being tied to underlying mechanisms.

The parametrization of the velocity dependence is based on sinusoidal analysis experiments (Kawai and Brandt, 1980). Our only complete source of data of this kind of analysis performed at 37°C is from Palmer et al. (2007), whose data was digitized and fitted using equation 2.3:

$$y(f) = \overbrace{A(2\pi i/f)^k}^{\text{passive term}} - \frac{Bif}{b+if} + \frac{Cif}{c+if} \tag{4.7}$$

using a standard unconstrained nonlinear optimization algorithm to obtain the viscous and elastic modulus. See Table 4.2 for results, which are consistent with the $c = 81.7$/s value reported by Palmer et al. Figure 4.6 shows the resulting fit to this sinusoidal analysis data.

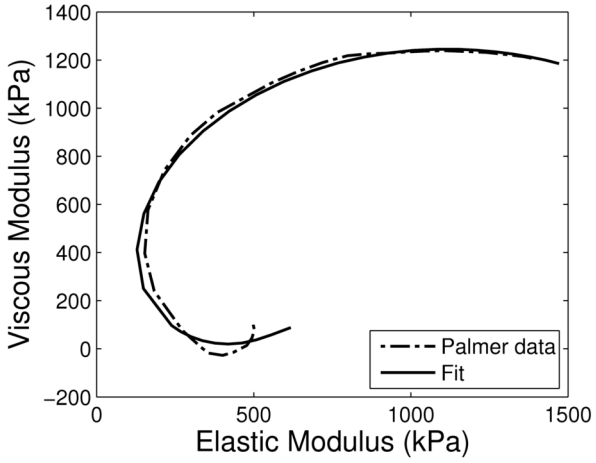

Figure 4.6: Fit to data from Palmer et al. (2007).

Data from Palmer et al. suggests $\sum A_i/\alpha_i < 0$, which would increase tension at a constant shortening velocity. Therefore we take into account the partial results from Blanchard et al. (1999), and set $\alpha_1 = 150/\text{s}, \alpha_2 = 500/\text{s}$. We leave a at 0.35 based on the NHS model. Finally we set $A_1 = -4, A_2 = -4A_1$ to obtain a magnitude and ratio of B, C in the range of experimental data. These values are uncertain as the viscous and elastic moduli scale with isometric tension, which was not reported by Palmer et al. and can

Source	$\alpha_1 = 2\pi b$	$\alpha_2 = 2\pi c$	B	C	temp.
Blanchard et al. Blanchard et al. (1999)	$2\pi 15 = 94$/s	$2\pi 66 = 415$/s	≈ 800	≈ 1000	27°C
Blanchard et al. Blanchard et al. (1999)	$2\pi 27 = 170$/s	$2\pi 94 = 591$/s	-	-	37°C
Palmer et al. (2007)	$2\pi 10.7 = 67$/s	$2\pi 83.7 = 526$/s	566	2489	37°C
Model	150/s	500/s		$-4\ B$	
Virtual experiment	153/s	502/s	642	$-3.7\ B$	

Table 4.2: Experimental data compared to model parameters and results for strain-rate response using sinusoidal analysis. Showing experimental results from the literature for the frequency parameters of the B and C processes converted to equivalent model parameters α_1, α_2, and their magnitudes B, C. The data from Palmer et al. were obtained by fitting parameters to data digitized from a figure. "Model" shows model parameters used, while "Virtual experiment" shows results from fitting the model response.

often be lower in experiments with saturating $[Ca^{2+}]_i$as mentioned previously. We thus investigate the effect of this parameter further in our whole-organ simulations below.

Running a virtual sinusoidal analysis ($[Ca^{2+}]_i = 1$ mM, 0.25% length change) and fitting the resulting curve to Equation 2.3 with $k = 0$ fixed results in values shown in Table 4.2. Our resulting $f_{\min} = 20$ Hz, $f_{\max} = 85$ Hz also closely match results from Palmer et al. ($f_{\min} = 20$ Hz, $f_{\max} = 80$ Hz).

4.1.7 Tension scaling

Finally, tension is scaled from normalized force to actual tension for a whole organ context:

$$T_a = T_{\text{ref}} \times F_n. \tag{4.8}$$

Where the reference tension T_{ref} encapsulates the total number of crossbridges and the fraction of cycling crossbridges in the force generating state at any time. For the NHS model the equivalent parameter is 56.2 kPa, but this is set to 100 kPa in later whole organ models (Niederer and Smith, 2009). In the Rice et al. model an equivalent value can be derived from $T_{\text{ref}} = \frac{\text{XB}_{\text{PostR}}}{P_{\text{NoXB}}} \times$ kxb / $\text{XB}^{\max}_{\text{PostR}} \approx 0.7 \times 120$ / $0.71 \approx 120$kPa, where P_{NoXB} is the sum of all states in the crossbridge cycle.

Experimental data often indicates much lower values of around $20 - 30$ kPa (Blanchard et al., 1999; Stuyvers et al., 2002; Palmer et al., 2004a) although some twitch transient data peaks at 50 kPa (Stull et al., 2002) and other results go up to 112 kPa for maximum developed tension (Kreutziger et al., 2011). We set $T_{\text{ref}} = 120$ kPa consistent with previous models and the higher end values for maximum tension and twitches, XB ≈ 0.35 resulting in 42 kPa in a twitch transient at resting SL.

4.2 Whole organ simulations

As murine experimental models are typically primarily focused on determining the effects of changes at the cellular scale on whole-heart function, and experimental data are more readily available at this scale, it is important to extend models to make this link between subcellular mechanisms and whole-organ function in models. This introduces several new model components, including the material properties of cardiac tissue, electrical activation sequences, mechanical boundary conditions, valves, and blood flow in the chambers. Their effects on model results also needs to be characterized within their experimental constraints, to provide or exclude alternative explanations for any changes observed in heart function. Most of our experimental measurements are only available for the left ventricle, including passive inflation and pressure-volume measurements. The MRI data includes a right ventricle as well, but is also not of sufficient resolution to accurately capture this part of the anatomy. Therefore we limit our computational model to only represent the left ventricle.

4.2.1 Experimental data

To develop and validate our model at the whole organ scale, we have recently obtained a range of multimodal whole-organ data sets in mice. These measurements were performed by our collaborators at the Oslo University Hospital on the same Black6 strain as used to parametrize the electrophysiological cell model (Li et al., 2011). Appendix B includes details of the materials and methods used to obtain these measurements. Briefly, the data includes in vivo MRI data and pressure-volume measurements and passive inflation of ex vivo hearts. MRI data used for mesh generation and volume estimation was obtained at a $0.2 \times 0.2 \times 1$ mm resolution during a whole heart cycle. Pressure and volume were measured in vivo using a pressure-volume catheter, along with ECG, and flow measurements to accurately determine start and end of ejection. These data were used to obtain end-diastolic pressure (EDP), aortic pressure at start of ejection, and pressure and volume transients for comparison.

The passive inflation data set was obtained from echo measurements in isolated hearts at $0, 5,$ and 10 mmHg, and used to estimate the increase in volume at a given pressure. Using manual segmentation of the short-axis slices as well as a measurement of apex-base distance in a long-axis slice, the volume change $V(p)/V(0)$ was estimated as:

$$V(p)/V(0) = A(p)/A(0) \cdot D(p)/D(0) \tag{4.9}$$

where $A(p)$ is the area of the cavity in a short-axis slice and $D(p)$ the apex-base distance, as functions of the cavity pressure. This was done separately for two slices to give two estimates for 5 and 10 mmHg.

4.2.2 Simulation setup

For our whole-organ simulations we apply the framework for electromechanics as described in the previous chapter. For mechanics we use a 112 element cubic Hermite mesh derived from the MRI data, at a time point halfway through diastole to approximately match the geometry of a stress-free ventricle. We estimate mechanical properties based on passive inflation data, as described below, and adjust the reference state as needed to match EDP and EDV from PV and MRI data. Since this process converges quickly, the second choice of reference geometry was consistent with available data. We use a dense electrophysiology grid with a spacing of ≈ 0.1 mm. The smaller size of the mouse allows for this high resolution, although the $\approx 10^5$ nodes still incur a significant computational cost due to the fast time scales involved in the detailed cellular model. The ODE solver used is described in algorithm 3. Due to faster contraction, a smaller time step than the 1 ms used in Chapter 3 for mechanics is required. Specifically, we use a 0.1 ms time step for mechanics and monodomain equations, and half this for monodomain equations during the depolarization, to ensure convergence. The mesh and mechanical boundary conditions are shown in Figure 4.7.

Algorithm 3: Cell model ODE solver. For the cell model solver we use a standard fixed-point iterations on a Crank-Nicolson scheme, with an adaptive time stepping scheme which decreases the time step temporarily when slow convergence is detected. The algorithm is presented here for completeness, with optimizations and numerical details present in the actual code omitted for clarity.

$\alpha = 0.5$; `// convergence speed threshold for adaptivity`
$\text{tol} = 10^{-5}$; `// convergence threshold`
$S =$ diagonal matrix with S_{ii} giving the approximate magnitude of variable y_i;
function timestep$(t, \mathbf{y}, \delta t)$; `// time step from` t `to` $t + \delta t$
$T = t + \delta t$;
while $t < T$ **do**
  $r_p = r = \infty$;
  $\mathbf{y}_s = \mathbf{y}$;
  while $r\delta t > tol$ **do**
    $\mathbf{y}_n = \mathbf{y} + \frac{\delta t}{2}\left(\frac{\mathrm{d}\mathbf{y}}{\mathrm{d}t}(t, \mathbf{y}) + \frac{\mathrm{d}\mathbf{y}}{\mathrm{d}t}(t, \mathbf{y_s})\right)$;
    $r = \max S^{-1}|\mathbf{y}_n - \mathbf{y}_s|$;
    if $r/r_p > \alpha$ **then**
      $\delta t = \delta t/2$;
      restart outer "$t < T$" loop, without resetting t;
    end
    $r_p = r$;
    $y_s = y_n$;
  end
  $y = y_s$;
  $t = t + \delta t$;
end

The framework is further extended with a full heart cycle model. We inflate to the end diastolic pressure (EDP= 0.7kPa), and stay in the diastolic phase until volume flow reverses. Next, we simulate isovolumetric contraction $\frac{\mathrm{d}v_{\mathrm{lv}}}{\mathrm{d}t} = 0$ until the cavity pressure is high enough to open the aortic valve ($p_{\mathrm{lv}} \geq p_a = 9$ kPa as in experimental data). Ejection is then simulated using the three element Windkessel model described in Chapter 2:

$$\frac{\mathrm{d}^2 v_{\mathrm{lv}}}{\mathrm{d}t^2} = -\left(\frac{1}{CZ} + \frac{1}{RC}\right)\frac{\mathrm{d}v_{\mathrm{lv}}}{\mathrm{d}t} - \frac{p_{\mathrm{lv}}}{CZR} - \frac{1}{Z}\frac{\mathrm{d}p_{\mathrm{lv}}}{\mathrm{d}t} \tag{4.10}$$

where R is the peripheral resistance, C is the total arterial compliance, and Z is the aortic characteristic impedance. When flow reverses once again, we switch to the isovolumetric constraint to reproduce isovolumetric relaxation. Finally, when pressure relaxes below 0.1kPa, we switch back to diastole by solving a simple phenomenological model for diastole given by $\frac{\mathrm{d}p_{\mathrm{lv}}}{\mathrm{d}t} = \frac{1}{10}(\mathrm{EDP} - p_{\mathrm{lv}})$. This is implemented by solving the equation

$$m_1\frac{\mathrm{d}^2 v_{\mathrm{lv}}}{\mathrm{d}t^2} + m_2\frac{\mathrm{d}v_{\mathrm{lv}}}{\mathrm{d}t} + m_3\frac{\mathrm{d}p_{\mathrm{lv}}}{\mathrm{d}t} + m_4 v_{\mathrm{lv}} + m_5 p_{\mathrm{lv}} + m_6 = 0 \tag{4.11}$$

monolithically in the mechanics Newton iteration process, , with coefficients m_i varying depending on the heart cycle to represent isovolumetric phases ($\frac{\mathrm{d}v_{\mathrm{lv}}}{\mathrm{d}t} = 0$), diastolic filling, or the Windkessel model.

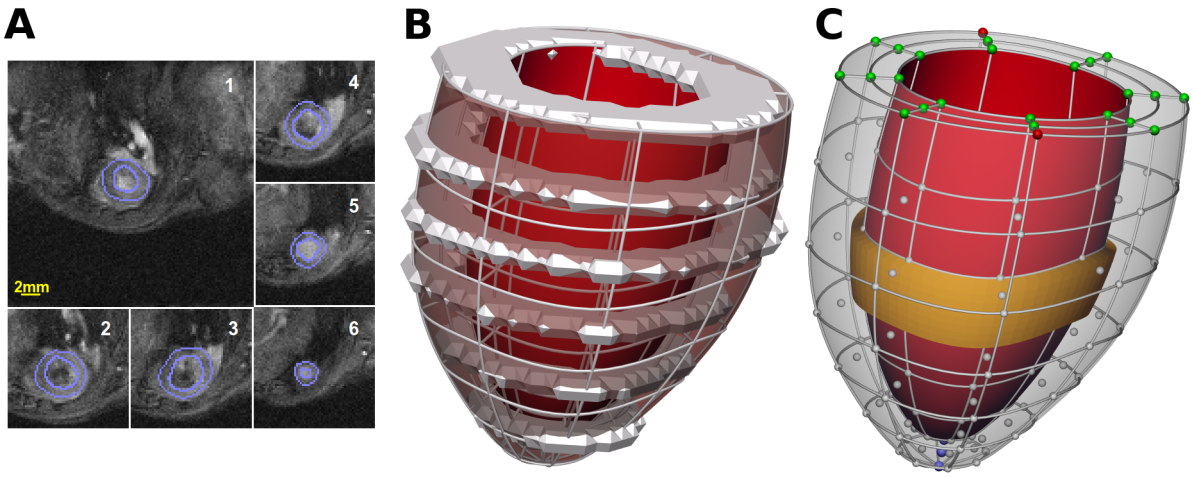

Figure 4.7: Mesh generation process and boundary conditions. Panel A shows the raw MRI data, numbered from base to apex, with segmentation in blue. Panel B shows the fitting of a cubic Hermite finite element mesh to this data set. Panel C shows the application of boundary conditions: blue nodes at the apex are part of multiple collapsed elements and have their derivatives fixed to zero. All nodes at the base (green) are fixed along the apex to base z axis. Furthermore, one of the red nodes at the base is fixed along the x and y directions, and the other along the y axis, which prevents free rotation and translation of the mesh during the solution process without limiting the deformation. Nodes at the apex and base have increased stiffness, interpolated throughout their neighbouring elements. The region of electrical activation is indicated in gold.

4.2.3 Electrical activation

Two important factors in the electrical activation of tissue are the activation pattern, and the conductance The latter was set using $D_{ff} = 0.33$ mm^2/ms to obtain a conduction velocity of around 75 cm/ms (Tamaddon et al., 2000), with $D_{ss} = D_{nn} = \frac{1}{2.2^2} D_{ff}$ consistent with the anisotropy observed in mice (Baker et al., 2000).

We initiate electrical activation with a stimulus midway between apex and base near the endocardium (60 mV/ms for 3 ms). This was compared to the simpler case of inducing full activation homogeneously, which gives a large decrease in EF (ejection fraction, 36.5% vs 56.3%). These differences are caused by a difference in calcium transient, which is increased in cells which act as a source for activation of nearby cells. This effect can be reproduced by inducing homogeneous activation with a stimulus current of $I_{\text{stim}} = -40\sin(2t)\text{mV/ms}$ for $t \in [0, \pi]$, which increases EF back up to 53.1%.

Since the shape of the stimulus current can change simulation results significantly, and is significantly different in tissue from the stimulus protocol used in single cells ($I_{\text{stim}} = -50\text{mV/ms}$ for 1 ms), we pace the cell model again for 5000 beats with the above sinusoidal current, so as to better prepare it for a tissue environment. This changes EF to 61.2% for endocardial activation, and aids in an earlier decrease of the larger calcium transient seen in tissue. Figure 4.8 shows this pacing protocol is sufficient to reach steady state ion concentrations.

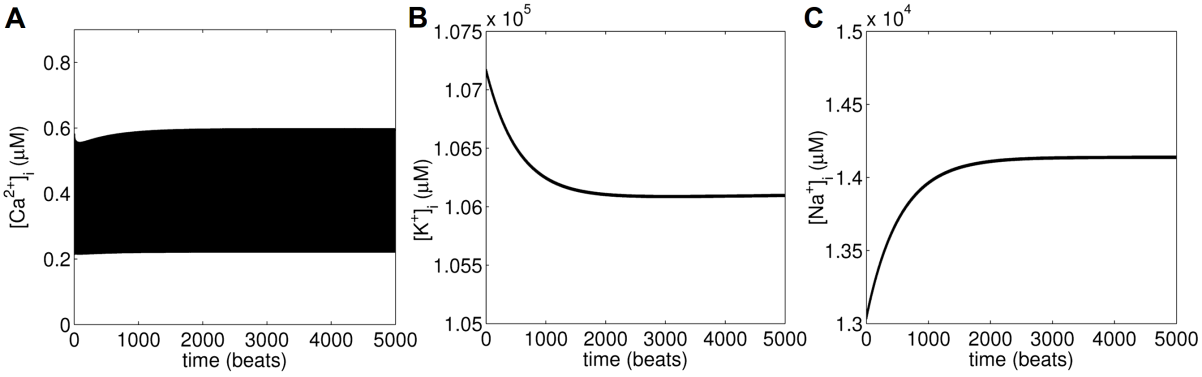

Figure 4.8: Changes in intracellular ion concentrations. Shown are changes in intracellular calcium (A), potassium (B) and sodicum (C) when pacing the electrophysiology model for 5000 heartbeats using the sinusoidal stimulus current.

4.2.4 Fibers

Our choice of fiber distribution throughout the tissue is -60°at the epicardium to +90°at the endocardium, based on mouse DTMRI data from Jiang et al. (2004). To investigate the sensitivity of our model to this choice, we compared it to several other choices of fiber directions. By looking at the position of the apex, we are able to clearly show

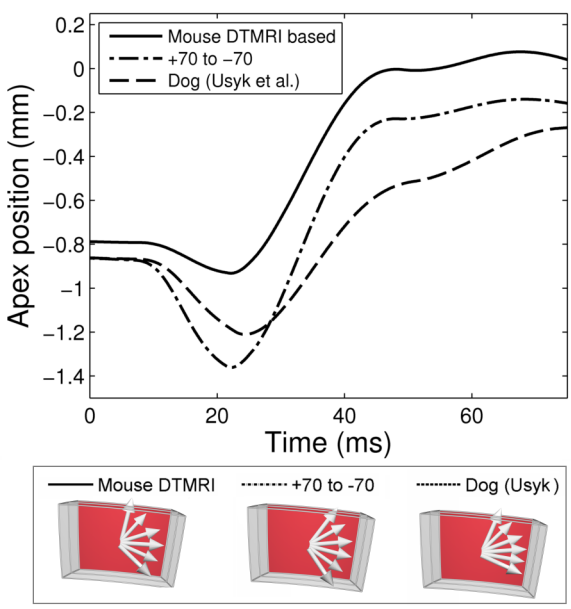

Figure 4.9: Location of the apex for three different fiber distributions. Simulation time includes inflation, isovolumetric contraction, ejection and the beginning of isovolumetric relaxation. The legend shows a slab of tissue with transmural fiber directions.

some small but significant differences in deformation. When using a -70°to +70°variation throughout the wall, ejection is similar, but the deformation was more realistic in the case of using mouse DTMRI data, as the apex-to-base distance did not increase. With detailed fiber directions based on dog data (Usyk et al., 2000) the ventricle inflates slightly more compared to the $\pm 70°$ case, and generates more force because of this, but the model produces an approximately 10% lower ejection fraction, as the apex moves less during ejection. Details of the apex movement for these three cases are shown in Figure 4.9, which demonstrates the steep fiber angles are important for preventing a large increase in apex-base distance during IVC. The mouse DTMRI fiber directions produce a similarly high ejection, but also does not suffer from the unrealistically large increase in apex/base distance during isovolumetric contraction.

4.2.5 Material and hemodynamic properties

What remains to be determined are the material properties of cardiac tissue, and the Windkessel parameters which determine the relation between blood flow and pressure during ejection.

For our material properties we use the Guccione constitutive law (see section 2.3.3.1) We use $C_1 = 1.1, C_2 = 8, C_3 = 2.0, C_4 = 3.7$ based on work by Omens et al. (1994), with C_2 adjusted from 9.2 to 8 to better match passive inflation data. Figure 4.10 shows the estimates for volume change in experimental data, compared to parameters from Omens et al. (1994) ($C_2 = 9.2$) and adjusted parameters ($C_2 = 8$). We only estimate C_2 since it is highly coupled to other constitutive parameters (Xi et al., 2011), and passive inflation

data are insufficient to estimate all parameters. Stiffness at the base and apex is increased ($C_1 = 8$) as in Chapter 3.

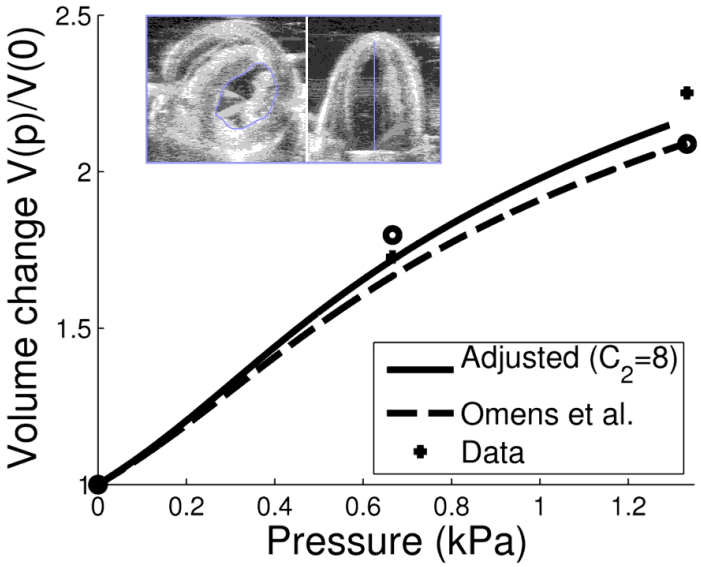

Figure 4.10: Constitutive parameters and passive inflation data. Figure shows the relative increase in volume. Inset shows example segmentation of echo data, where apex-base distance is indicated in the long-axis slices and the cavity is segmented in the short-axis slices.

For the Windkessel model we use $R = 400\,\mathrm{mmHg\,s/ml}$, $Z = 20\,\mathrm{mmHg\,s/ml}$, $C = 0.002\,\mathrm{ml/mmHg}$. Aortic characteristic impedance and peripheral resistance are compatible with extrapolations from rat data (Westerhof and Elzinga, 1991) assuming the mass of a mouse is 20% that of a rat, as well as data from Segers et al. (2005). A simple estimate using the cardiac output and aortic blood pressure results in $R = 535\,\mathrm{mmHg\,s/ml}$, which is known to be an overestimate (Toorop et al., 1987), and therefore also consistent with our choice. Compliance was based on differences between different Windkessel model fits (Segers et al., 2008) and data from four-element fits (Segers et al., 2005) to constrain C to a moderate increase from the value used in four element Windkessel models, and then adjusted according to PV data.

4.3 Parameter variation results

Table 4.3 shows a summary of parameter variations at the whole-organ level. We have chosen a set of key metrics available from pressure-volume data to compare with. Of these, ejection time and peak systolic pressure are important for characterizing ejection, easily determined, and show little variation across experiments. The other measures, end-systolic pressure and stroke volume, are more difficult to compare directly, as end-systolic pressure is more variable in the literature, and the volume measurements differs between MRI and PV data. However, these are still included to give a more complete picture of the relative influence of different parameters.

	ejection	peak SP	ESP	SV
PV data	43 ms	11.8 kPa	6.9 kPa	28.8 µl
default	27.3 ms	16.0 kPa	11.3 kPa	38.5 µl
Whole-organ parameters				
C_2 −12.5%	↑ 0.3 ms	↑ 0.3 kPa	↑ 0.1 kPa	↑ 1.9 µl
C_4 +370%	↓ 0.5 ms	↑ 0.3 kPa	↑ 0.1 kPa	↑ 1.1 µl
EDP +0.1 kPa	↑ 0.5 ms	↑ 0.4 kPa	↑ 0.1 kPa	↑ 2.6 µl
p_a +1 kPa	↑ 0.1 ms	↑ 0.5 kPa	⇑ 0.7 kPa	↓ 1.8 µl
R −50%	↑ 0.1 ms	↓ 0.1 kPa	↓ 0.4 kPa	↑ 0.5 µl
Z +50%	⇑ 3.8 ms	⇑ 1.3 kPa	↓ 0.3 kPa	↓ 2.6 µl
C −50%	=	↑ 0.5 kPa	⇑ 1.6 kPa	⇓ 4.6 µl
Cellular parameters				
β_0 −50%	↑ 0.1 ms	↑ 0.2 kPa	=	↑ 2.4 µl
β_1 −50%	⇑ 2.5 ms	↓ 0.5 kPa	↓ 0.1 kPa	↓ 0.2 µl
T_{ref} −20 kPa	↑ 1.3 ms	⇓ 1.3 kPa	↓ 0.5 kPa	⇓ 5.2 µl
$A_1 = -29$	⇑ 10.8 ms	⇓ 2.7 kPa	↓ 0.5 kPa	⇓ 4.9 µl
a +50%	↑ 0.5 ms	↓ 0.2 kPa	↓ 0.1 kPa	=

Table 4.3: Summary of parameter sensitivity results at the whole organ level. Results shown for duration of ejection, peak systolic pressure (SP), end systolic pressure (ESP) and stroke volume (SV), in the first beat of the simulation. The magnitude of parameter variation is based on how constrained it is given available data, and generally taken in the direction to increase duration of ejection. See Tables 4.4 and 4.5 for detailed results.

The constitutive parameters C_1, C_2, C_3 have similar effects on overall stiffness, where a higher stiffness decreases diastolic volume, and ejection as expected. Surprisingly, increasing C_4 results in a slightly *higher* SV, and duration of ejection can both slightly increase or decrease depending on the geometry used. Overall the model is very insensitive to large changes in this parameter. The model is also not very sensitive to large changes in R or C.

There are clearly some significant differences between simulations and PV data, in both the duration of ejection and peak systolic pressure. The only parameter which extends ejection by > 1 ms for our default parameter variation is the aortic characteristic impedance Z. However, this parameter is well constrained from data, and furthermore increases peak systolic pressure when extending ejection, increasing the difference between model results and pressure data from measurements.

4.4 Coupling mechanisms

Even after careful model parametrization, significant differences remain between experimental data and simulations, as can be seen from comparing the rows 'PV data' and 'default' in Table 4.3. The new parameters and boundary conditions introduced when embedding the cellular model within the whole organ framework have been constrained, and we have found no explanation at this scale. This motivated an investigation into those aspects of the cell model that were less constrained during the cellular modelling stage,

and are influenced by the mechanical deformation. This includes the balance between the mechanisms of length dependence, as well as aspects of the velocity dependence.

4.4.1 Length dependence of tension

For the length dependence of tension, we included a filament overlap factor as well as a shift in calcium sensitivity. We assumed the latter factor was dominant, but had no direct data in mice to constrain their relative influence.

To test the assumptions made in our cell model, we applied two parametrizations which give a roughly identical increase in tension for 10% stretch: our parametrization $\beta_0 = 1.65, \beta_1 = -1.5$ with dominant LDA factors, and $\beta_0 = 4.9, \beta_1 = -0.8$ closer to the NHS model's settings. The comparison in Figure 4.11 (A) shows the former parameter set maintains higher pressures for longer, as it takes some time for tension to decrease when shortening, which leads to a higher EF and faster relaxation. These differences show that our initial choice is closer to experimental data, and suggests to keep the unchanged parametrization.

4.4.2 Velocity dependence

Another important aspect of the cell model, in the context of ongoing debates about the mechanisms underlying the coupling between mechanical deformation and cell function, is the velocity dependence. We parametrized this model component using data from sinusoidal analysis. The moduli A_1, A_2 involved were fitted to experimental data using the viscous and elastic modulus, but these scale with isometric tension, which can often be lower in experimental measurements.

To further investigate the effect of these parameters, in light of the differences between experimental data and our results, we again compare two different cases in detail. Comparison of our default parametrization as outlined in 4.1.6 to using $A_1 = -29$ as in the NHS model (keeping $A_2 = -4A_1$). Figure 4.11 (B) shows the difference is clear, and the higher velocity dependence is much closer to PV catheter pressure data. This confirms our previous suspicion that the elastic and viscous modulus may not always be suitable for parametrizing single cell models directly. The results also show a reduction in several differences between model and experiments, most significantly the duration of ejection which was much lower. Other cellular scale parameters which can reduce this difference include a decrease in the length-dependent binding parameter β_1. However, β_0 has the opposite effect and the combination of these parameters is well constrained from cellular data, as shown in the previous section.

A higher a results in a slightly longer ejection phase, and lowers peak systolic pressure, though the effects are very small considering experimental data is centered around the $0.2 - 0.4$ range (Niederer et al., 2006). We also briefly tested violating the constraint $\sum A_i/\alpha_i < 0$ mentioned in the section on cellular modelling (by setting $\alpha_2 = 750$ /s or $\alpha_1 = 75$ /s). This results in oscillating tension and strain, as well as very short ejection time, confirming that the adjustment to meet this constraint was indeed needed. Figure 4.11

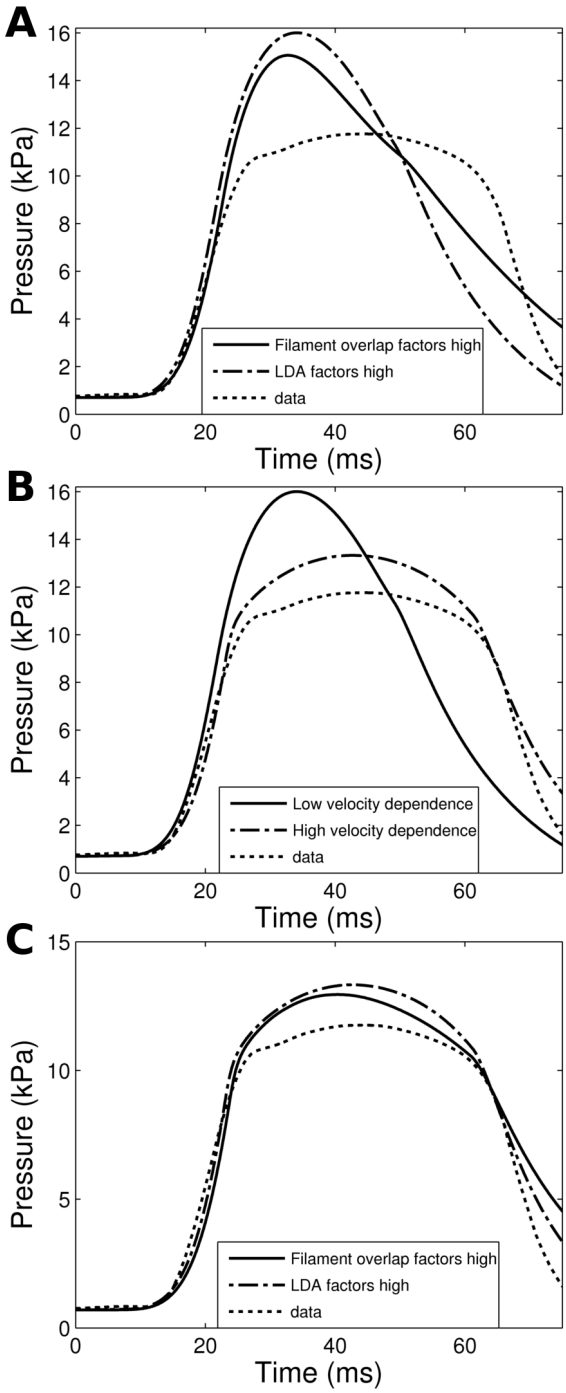

Figure 4.11: Effect of length and velocity dependence on whole organ function. Panel A shows a comparison for two different length dependent tension mechanisms, with weak velocity dependence. Panel B shows a comparison of two magnitudes for velocity dependent effects. Panel C shows the same comparison of length dependence as panel A, but using a strong velocity dependence.

(C) shows that in this corrected case, our conclusions about the length dependence are still valid, with 4 µl higher ejection and better relaxation in the case of high length-dependent activation.

4.4.3 Tension scale

Finally, we consider the tension scale T_{ref}. For our initial case, decreasing reference tension to $T_{\text{ref}} = 100$ kPa decreased ejection by 5.2 µl, lowering overall pressure without significantly impacting duration of ejection. In the case of the proposed high velocity dependence, ejection similarly decreased, taking it out of the range of experimental values. Increasing T_{ref} to 140 kPa increased both ejection fraction and overall pressure. This shows that $T_{\text{ref}} = 120$ kPa is a more realistic choice than $T_{\text{ref}} = 100$ kPa, in line with isometric twitch force used in other models. However, it can not rule out a value which is slightly higher, considering the variability in peak pressure found in experimental data (Joho et al., 2007). Figure 4.12 shows a pressure-volume loop for the cases $T_{\text{ref}} = 120$ kPa, $A_1 = -29$ and $T_{\text{ref}} = 140$ kPa, $A_1 = -35$, compared to experimental data. Both of these cases are well within experimental variability, with end-systolic volume between estimates from PV and MRI (≈ 25 µl). Figure 4.13 shows the $T_{\text{ref}} = 120$ kPa, $A_1 = -29$ case in more detail. As there was a significant difference in IVC duration, we also performed a simulation at 8 Hz, closer to the MRI data, at which this difference was reduced as pressure transient minima coincided.

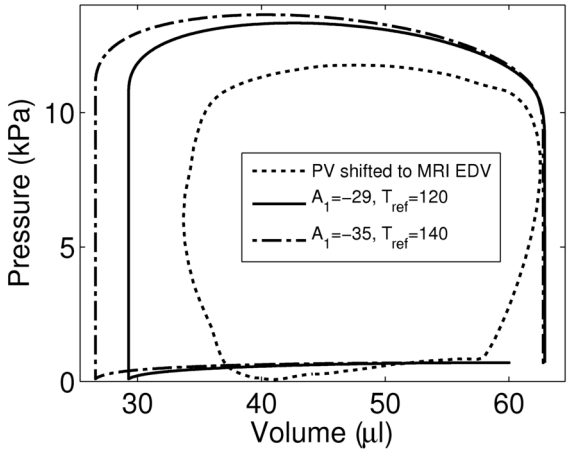

Figure 4.12: Pressure-volume loop, compared to echo data. The volume for PV data has been shifted to the EDV of MRI data, to account for elements like papillary muscles being included in volume in both simulation and MRI data, but not in echo. End systolic volume from MRI data coincides approximately with the left axis limits (25 µl).

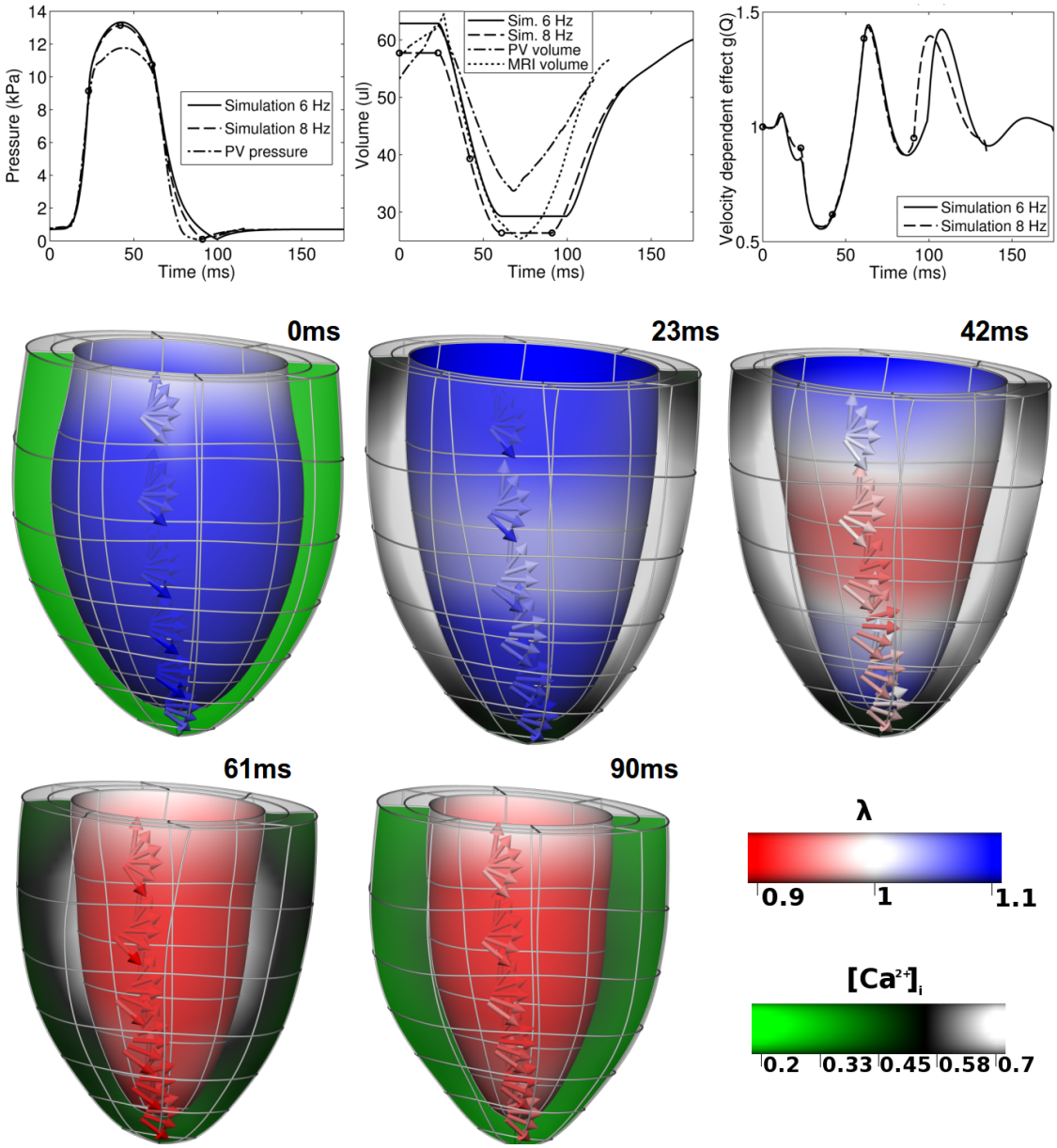

Figure 4.13: Detailed simulation results. Results obtained using $T_{\text{ref}} = 120$, $A_1 = -29$. Left panels show velocity and pressure for simulations at both 6 Hz and 8 Hz compared to experimental data, with PV catheter pressure offset to match EDV from MRI data. Note that heart rates differ slightly between PV and MRI data. Bottom left panel shows the mean value of $g(Q)$, which indicates the relative effect of the velocity dependence on tension. Panels on the right show simulation results (8 Hz) at key points: end of inflation, beginning of ejection, mid ejection, end of ejection and end of isovolumetric relaxation. Both the fiber arrows and the endocardial surface are colored to represent the fiber strain λ. Transmural surfaces is colored depending on the calcium concentration, ranging from green (diastolic) to black (peak in single cell preparations with standard pacing) to white (hyper-activated in tissue).

4.5 Discussion

In this chapter we have developed an electromechanical model which can reproduce the ventricular function of the mouse at body temperature. The model combines a novel cellular contraction model, and a ventricular model for electromechanics. The limitations and wider significance of both components are discussed in this section.

4.5.1 The cellular contraction model

A fundamental component of our model for electromechanics of the mouse, is the cardiac cellular contraction model we have developed. This model is simple enough to be suitable for use in organ-scale simulations, while still being firmly grounded in the biological foundations of muscle contraction.

To parametrize this model we have used a range of experimental data from the literature, including twitch transient times, properties of isolated myofilaments, force-calcium curves, and other data. Our visualization method for parameter identifiability shows which parameters of the contraction model are already well determined from this experimental data, and where new experimental data could help further model development. For example, it shows that the narrow but long valley of viable parameters shown in Figure 4.4 (A) means that more detailed data on calcium to TnC binding at physiological temperatures would further constrain both parameter values.

However, the model also has a number of limitations which may be improved upon in the future. Firstly, in our contraction model, the steep relationship between force and calcium is driven by cooperative effects at two different points. The first is the equation for calcium binding to troponin C. This choice was mainly driven by experimental results which show this reaction is cooperative, but not sufficiently so to explain force-calcium curves. We also model cooperativity downstream from TnC activation, which represents cooperative effects of tropomyosin and crossbridges during tension development in the myofilaments. Such a two-stage cooperativity model has to our knowledge not been used in previous mathematical models of cardiac contraction. The resulting force-calcium relationship shows strong biphasic cooperativity, with higher cooperativity at lower calcium concentrations. This is in good quantitative agreement with experimental data that was not used in parametrizing our model, further validating our choice of including multiple cooperative effects. A single-stage cooperative binding, with a simple ligand binding model for TnC as used in previous models, still produces a biphasic Hill curve, but not one that quantitatively agrees with the experimental data. Furthermore, from the visualization of viable regions in parameter space we can see that our choice of cooperativity is well constrained by experimental data. However, there are also still a number of uncertainties in our model of cooperativity. Without a good understanding of the biophysical underpinnings of cooperativity, Hill curves are used to represent individual cooperative effects. Although these are commonly used to represent a generic type of cooperative reaction, they are derived using a theoretical assumption which is biologically implausible (Weiss, 1997).

Furthermore, the choice of splitting cooperative terms between binding and unbinding is not well constrained. For calcium to TnC binding, the cooperativity was assumed to be on the binding rate, whereas downstream cooperative effects were split between binding and unbinding. This was mainly motivated by previous modelling efforts and the need for some cooperative unbinding to allow for sufficiently fast relaxation. Thus, although some cooperative unbinding is needed to accurately reflect the relaxation of muscle in an isometric twitch, and our model of two-stage cooperativity represents experimental data well, the exact form of our model is not grounded in solid biophysical mechanisms, as these are currently not known.

The length-dependent aspect of our contraction model is largely based on phenomenological considerations. Whereas recent experimental data implicates titin and troponin as major components underpinning the length dependent response, our model implements LDA as a simple modification of the half-activation of calcium to TnC. In practice this choice works well to reproduce experimental data. However, this result may be in part due the binding step of calcium to TnC introducing a small delay in length-dependent activation, which ensures that the strong decrease in tension influences late ejection and isovolumetric relaxation. In reality this delay may be linked to other biological mechanisms, such as titin and its downstream factors. Strong delays in the response of force to length changes have been shown before in experiments (Levy and Landesberg, 2006), but to our knowledge has not been measured in mice at body temperature, and will likely be difficult to separate from velocity dependent effects under these conditions. Further length-dependence is implemented as filament overlap, although this is only a minor factor, and there are fewer uncertainties in representing this mechanism. The simpler form we use is only suitable near resting sarcomere length, which is sufficient in realistic tissue deformations. This LDA model may be updated in the future as more data becomes available, although the difficulties that have been encountered in this field so far suggest that it may be several decades until controversies are resolved and consistent quantitative data of mechanisms of length-dependent activation of cardiac muscle becomes available.

The velocity dependence of cardiac muscle was modelled using a fading memory approach. This approach fits well with the experimental data from sinusoidal analysis that was used to parametrize it. Our data sources suggested the lack of a D process in murine cardiac muscle, which has been previously hypothesized to not be significant in cardiac muscle in general. Due to mathematical constraints on the parameters, i.e. the fact that tension should decrease when muscle shortens with a constant velocity. we used data from two different sources. Both of these sources presented data from mice at body temperature, and the differences may reflect difficulties in fitting data, especially at lower frequencies. Although in theory sinusoidal analysis data can be used directly to parametrize a fading memory model, the magnitude of results is conflated with the tension generated by cells. Normalized metrics may be more useful in parametrizing contraction models, but the mean active tension during such experiments is often not reported. The parameter a, which reflects the curvature of the force-velocity response, was inherited from previous work. This parameter has been shown to be relatively constant across species. Furthermore, model

predictions are not influenced much by changing this parameter within the range of experimentally observed values. The form of the force-velocity equation is also dependent on the assumptions made in NHS model, i.e. that shortening and lengthening muscle have opposite responses. Considering current research data suggests that these responses involve different mechanisms (Yadid and Landesberg, 2010; de Tombe and ter Keurs, 1992), such symmetry is likely to be an oversimplification. Other recent research points to a more complex response, which may be dependent on the history of tension development (Nishikawa et al., 2012), although this research is still preliminary and speculative.

In summary, our contraction model improves significantly on existing models and provides novel explanations for experimental data. Further refinements to the model can be made in future work, especially as additional experimental data becomes available which better elucidates the mechanisms of cardiac muscle contraction.

4.5.2 The ventricular model

The cellular contraction model was embedded in an electromechanical model of the left ventricle. The parameters introduced at the tissue level include tissue conductivity, mechanical properties of tissue, and hemodynamics. Extending our model thus required additional experimental data, which was collected by our collaborators. Data from passive inflation and in vivo pressure-volume loops, combined with data in the literature, enabled us to determine most of these parameters introduced at the whole-organ level.

We were able to estimate overall tissue stiffness based on passive inflation data. However, C_1 and C_2 remain tightly coupled as previously shown (Xi et al., 2011). The relatively small effect of C_4 on the mechanical deformation explains the large variations in this parameter between different studies, and the difficulty of determining it using optimization methods (see e.g. Wang et al. (2009)).

Regarding hemodynamics, we identified pressure at the beginning of ejection as an important parameter which can significantly influence simulation results. Taking this parameter directly from experimental results prevents incorrect fitting of Windkessel models and velocity dependent effects, as they are highly coupled with pressure at the beginning of ejection in their effects on peak systolic pressure. The three-element Windkessel model we use does not include an inertance element, unlike more detailed models of hemodynamics (Segers et al., 2008). This may have caused ejection to end earlier in our model, with a higher end systolic pressure, although it is less likely to significantly affect predictions of ejection fraction. For our whole organ results, we have used a simple model for diastole, as our study focuses on earlier cardiac phases, which are more sensitive in changes to our parameters. Overall, parameters introduced at the tissue level tend to be either well constrained by these data, or have a relatively minor effect on results.

Using this model we have also demonstrated that using whole-organ experimental data and modelling can help bridge some of the uncertainties inherent in cellular experimental data and improve our understanding of mechanical feedback mechanisms. The marked differences between isometric tension development in single cells and pressure development measured in vivo, can be largely attributed to a strong velocity-dependent component of

tension development during early ejection. This velocity dependence is key in both limiting the rate of pressure development as well as extending the duration of ejection, resulting in the more flattened shape of pressure transients. At the end of ejection, tension is briefly increased by the 'B process' known from sinusoidal analysis (Kawai et al., 1993), resulting in higher pressures at the end of ejection, as can be seen from the velocity dependence effects in Figure 4.13. The end of this phase, combined with the faster relaxation at a shorter sarcomere length, likely leads to the high $\mathrm{d}p/\mathrm{d}t_{\mathrm{min}}$values seen. Although this result was obtained in mice, the observed differences between tension transients in isolated cells are apparent in many other species, including humans. Thus, our results strongly suggest that including a velocity-dependent component of tension is important across species in accurately predicting tension generation during systole.

Furthermore this result confirms our suspicion that isometric tension in these single cell experiments was likely to be much lower than generated in vivo. Explicit reporting of the isometric tension during sinusoidal analysis experiments would make such experimental data more useful for direct use in cell model parametrization, by allowing parametrization based in relative magnitudes. Compared to previous parametrization of fading memory model in the NHS model, our analysis revealed similar magnitudes for the B and C processes, although they have higher characteristic frequencies. This may be related to the fast heart rate in mice. We were also able to test the choice of T_{ref} in a whole-organ context, confirming that isometric twitch transients at resting SL should generate around 40-45 kPa peak tension, as used in previous whole-organ work and cell models.

Fiber directions were also shown to be important, as they can affect deformation and whole-heart function, most significantly apex to base shortening during IVC and ejection. Our current dataset is based on DTMRI measurements in the literature, but uses only the transmural variation in the fiber angle and assumes apex-to-base heterogeneity. Similarly, as mentioned in Chapter 2, the use of a left-ventricular model with transmural homogeneity may limit the predictive value of the model with respect to the mechanical deformation. This is apparent in Figure 4.13, where the movement of the base is likely influenced by the lack of connection to other tissue near the base.

Modelling cardiac function at a higher heart rate and physiological temperature allowed for more quantitative comparison with data from in vivo measurements compared to previous murine models at low temperatures or pacing frequencies, as differences between models and experiments can not simply be rationalised by appealing to temperature differences. Using more physiological conditions, it has already been shown that previous contraction models do not always handle relaxation well at these pacing frequencies, which can easily go unnoticed when running simulations at 1 Hz or comparing simulation results to experimental data obtained at lower temperatures.

Finally, there are significant differences between experimental measurements from conscious mice, compared to anaesthetized mice (Joho et al., 2007). In this thesis we have focused on the latter, consistent with our recently obtained experimental measurements and most data in the literature. However, to what extent these differences involve changes in function at the cellular scale remains an important open question.

Despite all of these minor limitations, the framework for mouse modelling is sufficiently detailed for investigation of specific experimental results. The next chapter contains a specific application of the framework by using it to investigate heart failure progression in a genetic knockout mouse.

These appendices present the extended results for parameter variation, and a clear summary of the contraction model equations.

4.A Detailed whole-organ results

Tables 4.4 and 4.5 included here present a more extensive version of Table 4.3. Shown are duration of isovolumetric contraction (IVC), duration of ejection (ej.), peak systolic pressure (peak SP), end-systolic pressure (ESP), end-diastolic volume (EDV) and end-systolic volume (ESV).

For completeness we repeat some of the parameter descriptions here: Material properties are governed by C_1, C_2, C_3, C_4. Windkessel parameters Z, C, R represent aortic impedance, aortic compliance, peripheral resistance. EDP and p_a are pressures at end-diastolic and end IVC respectively. T_{ref} is the reference tension. Reaction rates for troponin C and crossbridges scale with $k_{\text{TRPN}}, k_{\text{xb}}$ respectively. The Hill coefficient for crossbridge binding is given by n_{xb}. Length dependence is modelled by filament overlap (β_0) and LDA (β_1), and α_1, α_2, a are involved in the velocity dependence as the characteristic frequency of the B and C processes and a measure of curvature of the steady state force-velocity relation, respectively. The main parameter A_1 which distinguishes the two tables represents the strength of the velocity dependence. Note that A_2 is changed along with A_1 as $A_2 = -4A_1$.

parameter	IVC (ms)	ej. (ms)	peak SP (kPa)	ESP (kPa)	EDV (μl)	ESV (μl)
default	21.9	27.3	16.0	11.3	62.9	24.4
$Z - 50\%$	21.9	22.6	14.1	11.5	62.9	22.3
$Z + 50\%$	21.9	31.1	17.3	11.0	62.9	26.9
$C - 50\%$	21.9	27.3	16.5	12.9	62.9	28.0
$C + 50\%$	21.9	27.2	15.8	10.6	62.9	23.2
$R - 50\%$	21.9	27.4	15.9	10.9	62.9	23.9
$R + 50\%$	21.9	27.3	16.0	11.4	62.9	24.6
$p_a = 8$ kPa	21.2	27.1	15.4	10.4	62.9	22.7
$p_a = 10$ kPa	22.5	27.4	16.5	12.0	62.9	26.2
EDP $= 0.6$ kPa	22.5	26.8	15.5	11.0	59.7	24.3
EDP $= 0.8$ kPa	21.4	27.7	16.4	11.5	65.5	24.4
$C_1 = 1.05$ kPa	21.7	27.5	16.1	11.2	63.7	24.2
$C_1 = 1.15$ kPa	22.0	27.2	15.9	11.1	62.1	24.3
$C_2 = 7$	21.6	27.6	16.3	11.4	64.6	24.2
$C_2 = 9$	22.2	27.0	15.8	11.2	61.2	24.6
$C_3 = 1.5$	Mechanics solver failed during IVC					
$C_3 = 2.5$	22.2	26.6	15.6	11.0	60.4	24.6
$C_4 = 5.35$	21.8	27.2	16.1	11.2	62.6	23.6
$C_4 = 13.7$	21.7	26.8	16.3	11.4	62.0	22.4
$T_{\text{ref}} = 100$ kPa	22.8	28.6	14.7	10.8	63.0	29.7
$T_{\text{ref}} = 140$ kPa	21.2	25.7	17.0	11.5	62.8	21.1
$\alpha_1 = 0.075$/ms	21.7	25.4	17.1	11.4	62.6	20.7
$\alpha_1 = 0.225$/ms	22.0	28.3	15.5	11.1	62.9	26.5
$\alpha_2 = 0.4$/ms	22.1	29.0	15.3	11.1	62.9	26.3
$\alpha_2 = 0.75$/ms	21.6	24.3	17.2	11.4	62.6	21.9
$a = 0.175$	21.9	26.8	16.2	11.3	62.9	24.4
$a = 0.525$	21.9	27.8	15.8	11.2	62.9	24.4
$k_{\text{xb}} = 0.05$/ms	24.2	30.2	15.4	11.2	62.9	24.1
$k_{\text{xb}} = 0.15$/ms	21.0	26.5	16.1	11.3	62.9	25.1
$k_{\text{TRPN}} = 0.05$/ms	26.0	30.6	15.3	11.1	62.9	24.4
$k_{\text{TRPN}} = 0.15$/ms	20.2	26.3	16.0	11.2	62.9	24.9
$\beta_0 = 0.825$	22.1	27.4	16.2	11.3	62.9	22.0
$\beta_0 = 2.475$	21.6	27.0	15.7	11.1	62.8	26.3
$\beta_1 = -0.75$	23.9	29.8	15.5	11.2	62.9	24.6
$\beta_1 = -2.25$	20.0	25.6	16.3	11.2	62.9	24.4
$n_{\text{xb}} = 4$	21.6	29.2	15.5	11.2	62.5	25.1
$n_{\text{xb}} = 6$	22.0	25.9	16.5	11.3	63.4	23.7

Table 4.4: Detailed whole organ parameter variation results for $\mathbf{A_1 = -4}$. Columns show duration of isovolumetric contraction, duration of ejection, peak systolic pressure, end-systolic pressure, end diastolic volume and end-systolic volume, respectively. Cells are colored according to minimum (blue), maximum (green), or no change from default (white).

parameter	IVC (ms)	ej. (ms)	peak SP (kPa)	ESP (kPa)	EDV (μl)	ESV (μl)
default	23.2	38.1	13.3	10.8	62.9	29.3
$Z - 50\%$	23.2	35.7	12.2	11.0	62.9	26.7
$Z + 50\%$	23.2	40.0	14.3	10.6	62.9	31.6
$C - 50\%$	23.2	37.4	14.1	12.1	62.9	31.9
$C + 50\%$	23.2	38.4	13.1	10.2	62.9	28.3
$R - 50\%$	23.2	38.4	13.2	10.3	62.9	28.6
$R + 50\%$	23.2	38.0	13.4	10.9	62.9	29.5
$p_a = 8$ kPa	22.6	38.3	12.7	10.0	62.9	27.2
$p_a = 10$ kPa	23.8	37.8	14.0	11.6	62.9	31.6
EDP $= 0.6$ kPa	23.8	37.2	13.0	10.6	59.7	29.1
EDP $= 0.8$ kPa	22.7	38.9	13.6	10.9	65.8	29.5
$C_1 = 1.0$ kPa	23.0	38.5	13.5	10.9	64.6	29.7
$C_1 = 1.2$ kPa	23.4	37.7	13.1	10.6	61.4	29.0
$C_2 = 7$	22.9	38.6	13.5	10.9	64.9	29.4
$C_2 = 9$	23.5	37.6	13.2	10.7	61.2	29.3
$C_3 = 1.5$	22.9	38.9	13.6	10.9	65.6	29.7
$C_3 = 2.5$	23.5	37.3	13.1	10.6	60.4	28.9
$C_4 = 5.35$	23.1	38.3	13.4	10.9	62.6	28.7
$C_4 = 13.7$	22.8	38.9	13.4	10.9	62.0	27.4
$T_{\text{ref}} = 100$	24.1	38.1	12.6	10.4	63.0	34.5
$T_{\text{ref}} = 140$	22.5	37.7	13.9	11.0	62.8	25.3
α_1 0.075	Mechanics solver failed during ejection					
α_1 0.225	23.7	40.4	12.3	10.3	62.9	37.0
α_2 0.4	23.9	41.7	12.1	10.3	62.9	36.1
α_2 0.75	Mechanics solver failed during ejection					
$a = 0.175$	23.0	36.7	13.7	10.9	62.9	28.3
$a = 0.525$	23.5	39.3	13.1	10.8	62.9	30.5
$k_{\text{xb}} = 0.05$/ms	25.4	41.2	13.1	10.7	62.9	28.8
$k_{\text{xb}} = 0.15$/ms	22.3	37.1	13.4	10.8	62.9	29.7
$k_{\text{TRPN}} = 0.05$/ms	27.3	42.3	13.1	10.7	62.9	28.9
$k_{\text{TRPN}} = 0.15$/ms	21.6	36.8	13.4	10.8	62.9	30.1
$\beta_0 = 0.825$	23.5	38.7	13.3	10.8	62.9	28.4
$\beta_0 = 2.475$	22.9	37.4	13.3	10.7	62.8	30.0
$\beta_1 = -0.75$	25.2	40.4	13.0	10.7	62.9	30.8
$\beta_1 = -2.25$	21.3	36.1	13.5	10.8	62.9	28.6
$n_{\text{xb}} = 4$	22.8	40.9	13.1	10.7	62.6	29.7
$n_{\text{xb}} = 6$	23.4	36.1	13.6	10.8	63.4	28.9

Table 4.5: Detailed whole organ parameter variation results for $\mathbf{A_1 = -29}$.

4.B Contraction model

This appendix lists all equations, symbols, and parameters used for the contraction model.

$$[\mathrm{Ca}^{2+}]_{\mathrm{T50}} = [\mathrm{Ca}^{2+}]^{\mathrm{ref}}_{\mathrm{T50}} \left(1 + \beta_1 \left(\lambda - 1\right)\right) \tag{4.12}$$

$$\frac{\mathrm{dTRPN}}{\mathrm{d}t} = k_{\mathrm{TRPN}} \left(\left(\frac{[\mathrm{Ca}^{2+}]_{\mathrm{i}}}{[\mathrm{Ca}^{2+}]_{\mathrm{T50}}} \right)^{n_{\mathrm{TRPN}}} (1 - \mathrm{TRPN}) - \mathrm{TRPN} \right) \tag{4.13}$$

$$\frac{\mathrm{dXB}}{\mathrm{d}t} = k_{\mathrm{xb}} \left(\mathrm{permtot}\ (1 - \mathrm{XB}) - \frac{1}{\mathrm{permtot}} \mathrm{XB} \right) \tag{4.14}$$

$$\mathrm{permtot} = \sqrt{\left(\frac{\mathrm{TRPN}}{\mathrm{TRPN}_{50}} \right)^{n_{\mathrm{xb}}}} \tag{4.15}$$

$$\frac{\mathrm{d}Q_i}{\mathrm{d}t} = A_i \frac{\mathrm{d}\lambda}{\mathrm{d}t} - \alpha_i Q_i \tag{4.16}$$

$$g(Q) = \begin{cases} \frac{aQ+1}{1-Q} & Q \leq 0 \\ \frac{1+(a+2)Q}{1+Q} & Q > 0 \end{cases} \quad \text{where } Q = \sum_{i=1}^{2} Q_i \tag{4.17}$$

$$h'(\lambda) = 1 + \beta_0(\lambda + \min(\lambda, 0.87) - 1.87) \tag{4.18}$$

$$h(\lambda) = \max(0, h'(\min(\lambda, 1.2)) \tag{4.19}$$

$$F_n = g(Q) \times h(\lambda) \times \mathrm{XB} \tag{4.20}$$

$$T_a = T_{\mathrm{ref}} \times F_n \tag{4.21}$$

Symbol	Meaning
λ	Extension ratio, i.e. $\lambda = \frac{\text{sarcomere length}}{\text{resting sarcomere length}}$.
$h(\lambda)$	Influence of filament overlap on tension.
$g(Q)$	Velocity dependent effect on tension
Q_i	Internal fading memory variables
TRPN	Fraction of regulatory troponin C sites with bound calcium
XB	Fraction of available crossbridges cycling.
F_n	Normalized force
T_a	Active tension

Table 4.6: Symbols used in the contraction model.

Parameter	Value	Meaning	Source
n_{TRPN}	2	Hill coefficient for cooperative binding of Ca to TnC	Fitted to F-pCa
k_{TRPN}	0.1/ms	Unbinding rate of Ca from TnC	Data from isolated filaments.
$[\mathrm{Ca}^{2+}]^{\mathrm{ref}}_{\mathrm{T50}}$	0.8 μM	Calcium sensitivity at resting sarcomere length	Cellular data, magnitude of calcium transient.
n_{xb}	5	Hill coefficient for cooperative crossbridge action	Data from isolated filaments.
k_{xb}	0.1/ms	Scaling factor for rate of cross-bridge binding	Fitting to isometric tension.
TRPN_{50}	0.35	Troponin C sensitivity	Fitting to isometric tension.
A_1	-29	Magnitude of the 'B process'	Whole-organ data and simulations.
A_2	$-4A_1$	Magnitude of the 'C process'	Sinusoidal analysis data.
α_1	150/s	$2\pi\times$ characteristic frequency of the 'B process'	Sinusoidal analysis data.
α_2	500/s	$2\pi\times$ characteristic frequency of the 'C process'	Sinusoidal analysis data.
β_0	1.65	Magnitude of filament overlap effects	Rice et al. model, based on sarcomere geometry.
β_1	-1.5	Magnitude of length-dependent activation effects.	Peak isometric tension data at several SL.
T_{ref}	120 kPa	Tension scale	Cellular data, previous work, confirmed by whole-organ simulations.

Table 4.7: Data sources and methods of parametrization for the contraction model.

Chapter 5

Heart failure progression in Serca2 knockout mice

Wee, sleekit, cow'rin, tim'rous beastie,
O, what a panic's in thy breastie!

As discussed in Chapter 2, contraction in cardiac muscle cells is caused by rapid changes in the intracellular calcium concentration. An important factor in these rapid changes is release and uptake of calcium ions by the sarcoplasmic reticulum (SR), an intracellular compartment which functions as a calcium store. Uptake of calcium into this store is regulated by the sarco(endo)plasmic reticulum Ca^{2+}ATPase 2 (SERCA2) ion pump, which transports calcium from the cytosol into the SR at the end of each heartbeat. The majority of calcium cycling during a heart beat is through release and uptake from the SR, with the remainder being transported through transmembrane currents such as the L-type calcium channel, sodium-calcium exchanger (NCX) and plasma membrane Ca^{2+}ATPase (PMCA). SR function accounts for up to 90% of calcium cycling in mice (Bers, 2002), and decreased SERCA2 function has been associated with both systolic and diastolic heart failure across species (Kranias and Bers, 2007; Louch et al., 2010).

To investigate the effects of decreased SERCA2 function, including the effects of the gene on normal function and its role in diseases, our collaborators at the Oslo University Hospital have developed a genetic knockout mouse (Andersson et al., 2009b). In this chapter we model these genetically modified mice, motivated by previous experimental results recently obtained in these animals. The next section provides some necessary background for this particular study. Section 5.2 further describes the role of our computational modelling framework, which we apply in the rest of this chapter to investigate the progression of heart failure in these mice.

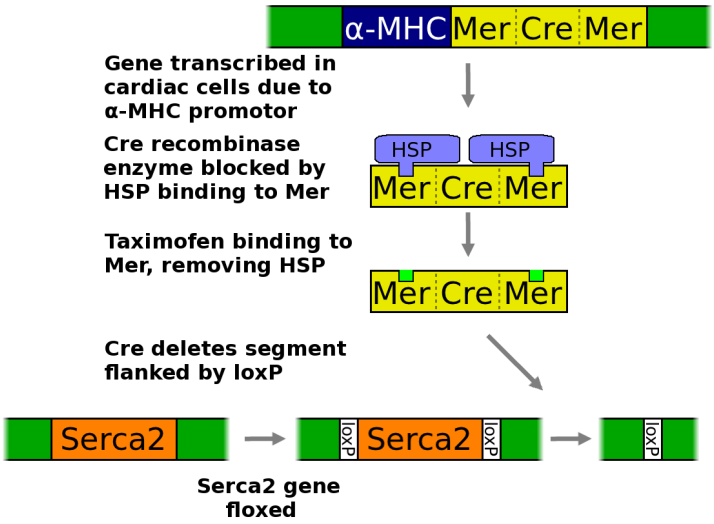

Figure 5.1: Serca2 knockout mouse. The Serca2 gene is 'floxed', which allows it to be the MerCreMer gene after introduction of tamoxifen.

5.1 Previous work in Serca2 knockout mice

As may be expected from the vital importance of SERCA in the heart, removal of the Serca2 gene has major consequences for heart function. Periasamy et al. (1999) found that when mating of heterozygous mutant mice with one missing copy of the Serca2 gene, there are no living homozygous offspring. That is, a full knockout of the SERCA pump is lethal at the embryonic stage, which prevents investigation of the effects of two missing copies of the Serca2 gene on heart function from birth.

Fortunately, technology for genetic manipulation has advanced to the point where gene-knockouts can be induced at a later stage, as well as limited to cardiac tissue. The mice we will model in this chapter are genetically modified to lose the Serca2 gene in cardiomyocytes after introduction of tamoxifen in their food. The development of these genetic knockout mice is described in detail in (Andersson et al., 2009b). Briefly, genes can be removed by using a Cre recombinase gene, which was originally discovered in a bacteriophage. The Cre gene removes sections of DNA flanked on both sides by a 34 base pair "loxP" signal sequence (Sauer and Henderson, 1988). By combining this gene with a tissue-specific promotor sequence, such as the α-MHC promotor (Sohal et al., 2001) or β-actin promotor (Zhang et al., 1996), the Cre gene will be expressed only in the heart.

Next, to be able to induce the expression of the Cre protein at a specific time, its genetic sequence is combined with that of a hormone binding domain. A hormone binding domain attached to a protein often inhibits expression of the protein in the absence of a relevant hormone. Specifically, a mutated variant of the oestrogen receptor is used, which is no longer sensitive to oestrogen, but still sensitive to the pharmaceutical tamoxifen (Littlewood et al., 1995). The effectiveness of such a hormone binding domain on the

inhibition of protein expression can depend on many factors, including which protein is targeted and the location of the hormone binding domain (Picard et al., 2000). In this particular case, Zhang et al. (1996) found that for the Cre protein, effectiveness increases when Cre is flanked on both sides by the tamoxifen binding domain. The resulting gene is referred to as MerCreMer (murine oestrogen receptor - Cre recombinase - murine oestrogen receptor).

Andersson et al. (2009b) applied these techniques to investigate the effects of gene knockout of the Serca2 gene in mice. They inserted the loxP signal sequences to flank the Serca2 gene to create heterozygous $\text{Serca2}^{\text{wt/flox}}$ mice*. These were used to breed homozygous $\text{Serca2}^{\text{flox/flox}}$ mice, before interbreeding with α-MHC MerCreMer mice to create $\text{Serca2}^{\text{flox/flox}}$ Tg(α-MHC MerCreMer) mice with a homozygous inducible cardiomyocyte specific gene knockout of the Serca2 gene. Figure 5.1 shows a schematic of the process of gene knockout in these mice.

The $\text{Serca2}^{\text{flox/flox}}$ mice are used as controls in research, and referred to as flox/flox or "FF" mice, while the $\text{Serca2}^{\text{flox/flox}}$ Tg(α-MHC MerCreMer) are referred to as knockout, "KO" mice. The FF mice are for our purposes considered identical to wild-type $\text{Serca2}^{\text{wt/wt}}$ mice, as the minor change of "floxing" this gene does not have significant effects on gene expression (Andersson et al., 2009b).

This genetically modified mouse has been the focus of several studies so far. In a follow-up study to developing the knockout mice, Andersson et al. (2009a) measured cellular calcium, shortening as well as whole-organ ejection. Even though SERCA protein content is reduced to $< 5\%$ by 4 weeks after knockout, ejection fraction is near normal. Only after 7 weeks the mice develop more severe cardiac dysfunction. This sustained function of the heart, despite a large reduction in SERCA function and lethality of a gene knockout in utero, suggests the existence of significant compensatory mechanisms which may be important in understanding SERCA related heart failure across species. Previous experiments on isolated myocytes, combined with mathematical modelling, has shown that calcium transients are compensated for by upregulation of transmembrane calcium dynamics, most importantly the L-type calcium channels and NCX (Li et al., 2011, 2012). Underlying these are adaptive changes in the cell geometry, including T-tubule remodelling and a decrease in SR volume (Swift et al., 2012). However, despite all of these compensatory mechanisms, calcium transients in knockout mice remain very small, an observation that seems fundamentally inconsistent with the whole organ response.

5.2 Computational modelling study

In this chapter we apply our integrative mouse modelling framework to investigate the link between cellular and whole-organ function in the Serca2 knockout mouse. There appears to be a significant discrepancy between the large decrease in calcium dynamics and the relatively small changes in whole-heart function observed. This discrepancy can be

* "flox" refers to **f**lanked by **lox**P

resolved in several ways. Firstly, compensatory mechanisms at the level of the myofilaments could be boosting the calcium signal to allow for sufficient tension generation to be consistent with the ejection fractions observed. Secondly, the calcium transient could be significantly different in vivo compared to what is measured in isolated cells. This is possible since previous observations in isolated myocytes were performed mainly in the absence of other factors present in vivo, and with many experiments performed at low frequencies. Most significantly, effects of β-adrenergic stimulation, which is involved in the body's response to stress and the fight-or-flight response, are not taken into account in such measurements. The effects of β-adrenergic stimulation include increased cardiac output through increased SERCA and L-type calcium influx, changes in calcium sensitivity, and myofilament properties (Saucerman and McCulloch, 2006; Metzger and Westfall, 2004). Furthermore, increased norepinephrine levels have been observed previously in KO mice (Andersson et al., 2009a), but have not yet been taken into account in experiments on isolated myocytes at physiological pacing rates.

In this chapter we use our electromechanical modelling framework to investigate both of these hypotheses: increased β-adrenergic stimulation and changes in myofilament properties. Since the data collected by our experimental collaborators on the effects of β-adrenergic stimulation on calcium dynamics can be investigated using an identical protocol as applied to control data, the effects of increased β-adrenergic stimulation are presented first in sections 5.3, 5.4 and 5.5. However, these measurements were performed in part due to preliminary results from computational modelling and visualization. As shown in Figure 5.2, contractile response to identical calcium concentrations differs drastically in knockout mice compared to control, and do not seem easily explainable from compensatory changes to the myofilaments alone. To better quantify this intuition, parameter estimation experiments are included at the end of this chapter in section 5.6, which outline the whole-organ response to alterations in myofilament properties.

5.3 Measurements of calcium transients

5.3.1 Experimental methods

Collaborators at the University of Oslo performed experimental measurements on isolated cardiac cells to obtain calcium transients. Measurements were performed 4 and 7 weeks after introduction of tamoxifen, in separate groups of mice, referred to as KO4 and KO7 mice. Control flox/flox mice at the same age as KO7 mice are denoted by FF. Pressure-volume loops were also measured in FF, KO4 and KO7 mice. Calcium transients were measured using whole-cell fluorescence, and calibrated using previously measured levels of diastolic calcium. These measurements were repeated with the addition of 200 nM isoproterenol, which is used to simulate the effect that β-adrenergic stimulation has in vivo. We refer to measurements with and without isoproterenol as '+ISO' and 'control' respectively throughout this chapter. For more details on the experimental methods, see appendix B.

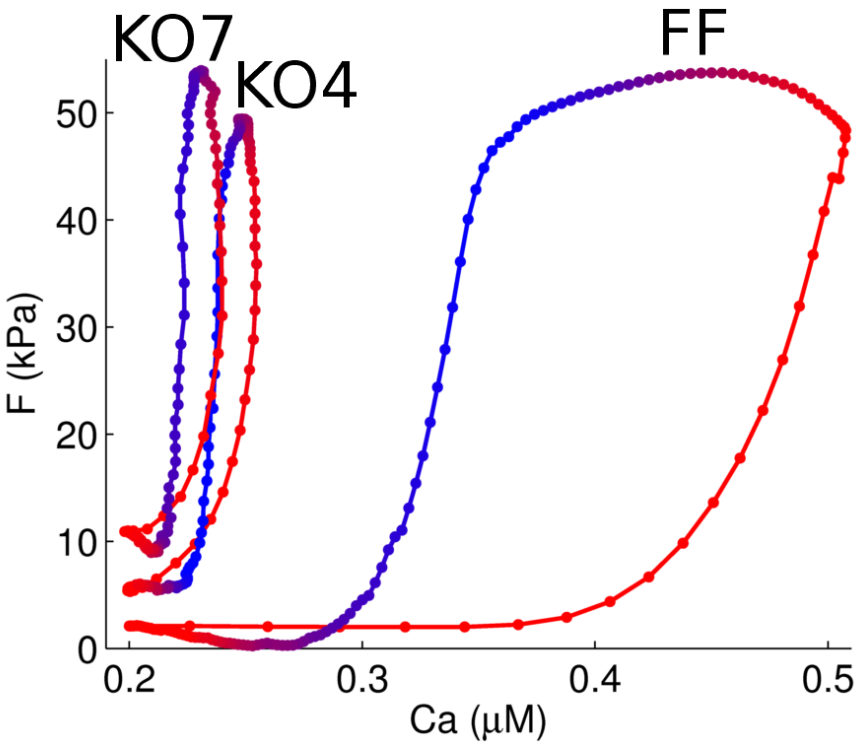

Figure 5.2: Force-calcium loops. A preliminary visualization which links previously measured cellular and whole-organ response. Results show force estimated as in section 5.5 plotted against previously measured calcium transients. Colors represent average sarcomere length, from $> 5\%$ shortening in blue to $> 5\%$ lengthening in red.

5.3.2 Results

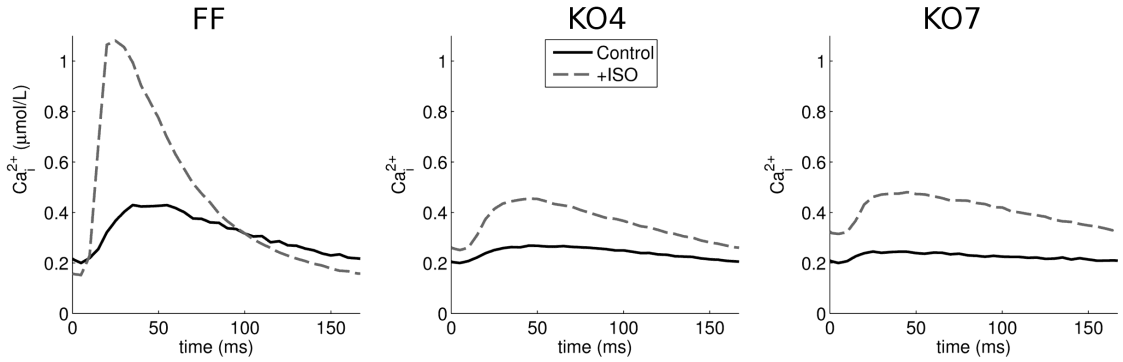

	FF	KO4	KO7
Control Min Ca	calibrated to 200 nM		
Control Peak Ca (nM)	442 ± 25	250 ± 5	236 ± 5
+ISO Min Ca (nM)	152 ± 11	251 ± 23	315 ± 17
+ISO Peak Ca (nM)	990 ± 135	459 ± 84	430 ± 29

Figure 5.3: Calcium transients without ('control') and with ('+ISO') isoproterenol. Panels show results as mean±SE in FF ($n = 7$), KO4 ($n = 12$) and KO7 ($n = 10$) mice from left to right. Accompanying table shows details of peak and minimum calcium concentrations. In control mice, diastolic calcium is maintained, while peak calcium decreases significantly. With isoproterenol, diastolic calcium decreases in FF due to upregulated SERCA, but increases in KO due to a lack of SERCA and increased calcium influx. Peak calcium increases with isoproterenol to reach levels approximately equal to FF control levels.

Representative calcium transients are shown in Fig. 5.3, along with details of diastolic and peak calcium measurements. Firstly, these replicate results previously shown for calcium transients in FF and KO mice in the absence of isoproterenol. In the absence of β-adrenergic stimulation, diastolic calcium is maintained at around 200 nM (Andersson et al., 2009a; Li et al., 2012), which was used to calibrate the new measurements. Peak calcium significantly decreased after gene knockout, and the magnitudes of calcium transients at 7 weeks after introduction of tamoxifen are consistently reduced to $< 15\%$ of FF. After addition of isoproterenol, we see a very different progression in the calcium transients. For the FF mice, peak calcium levels increase due to upregulated calcium influx, while diastolic calcium levels decrease through upregulated SERCA. However, in KO mice upregulation of SERCA has little effect, as protein levels are low after the genetic knockout. This causes a significant increase in both diastolic and peak calcium in the KO+ISO compared to KO control. Interestingly, the peak calcium levels in knockout mice treated with isoproterenol reach levels which appear equal to those in healthy FF controls, and this level is maintained at both time points. Indeed, statistical analysis of peak calcium in FF control, KO4+ISO and KO7+ISO confirms that they are not significantly different (ANOVA $p = 0.945$).

5.4 Simulating ventricular function

Metric	FF	KO4	KO7
EDV adj. (μl)	58.9	54.6	55.0
EDP (kPa)	1.02	1.66	3.02
SEP (kPa)	10.5	9.8	11.1
Min. P (kPa)	0.08	1.28	2.35
Control $[Ca^{2+}]^{ref}_{T50}$ (μM)	0.578	0.469	0.423
+ISO $[Ca^{2+}]^{ref}_{T50}$ (μM)	0.427	0.588	0.661

Table 5.1: Simulated parameters. Parameters obtained from experimental pressure-volume loops. EDV adj. is end-diastolic volume adjusted by 15μl to account for muscles included in simulation cavity volume but not in PV volume (as determined in the last chapter by comparison with MRI data). EDP is end-diastolic pressure. SEP is the pressure at start of ejection, used to determine end of isovolumetric contraction. Min. P is the minimal pressure, used to determine end of isovolumetric relaxation. The parameter $[Ca^{2+}]^{ref}_{T50}$ is the half-activation of calcium binding to TnC at resting sarcomere length, and was fitted such that EDV matches within 0.1μl when prescribing EDP. Calcium sensitivity $[Ca^{2+}]^{ref}_{T50}$ was chosen such that EDV matches experimental data when EDP is prescribed, separately in control and +ISO cases.

We used our electromechanical modelling framework developed in the last two chapters to perform simulations on a left-ventricular geometry and predict whole-organ function from calcium transients described in the previous section. However, due to the fact that the electrophysiology models by Li et al. (2012) only accurately represent calcium dynamics in knockout mice under 1 Hz stimulation and in the absence of β-adrenergic stimulation, calcium transients were prescribed directly from experimental measurements. The lack of an electrophysiology model also has consequences for the activation component of simulations. Although activation times from previous simulations could be used, we found that in these simulations 80% of tissue was activated within a 3 ms period, and homogeneous activation did not substantially affect results in Chapter 4. Therefore, we chose a simpler homogeneous activation for the simulations in this chapter.

We performed simulations for calcium transients measured in FF, KO4 and KO7 mice, both with and without isoproterenol. In all cases the calcium sensitivity $[Ca^{2+}]^{ref}_{T50}$, which determines the half-maximal activation of calcium binding to TnC, was set to match end-diastolic volume at end-diastolic pressure, as this affinity is known to change in vivo depending on regulatory factors. Other contractile parameters were unchanged from the previous chapter, as we have already fitted these to match healthy mouse tension generation at physiological temperature and frequency. Hemodynamic parameters for transitions from isovolumetric contraction to ejection, and from isovolumetric relaxation to diastole were taken from representative traces of experimental PV data, summarized in Table 5.1. As heart failure was observed in these animals without hypertrophy (Andersson et al., 2009a), the LV geometry and constitutive properties used were identical to values used in the previous chapter.

5.4.1 Results

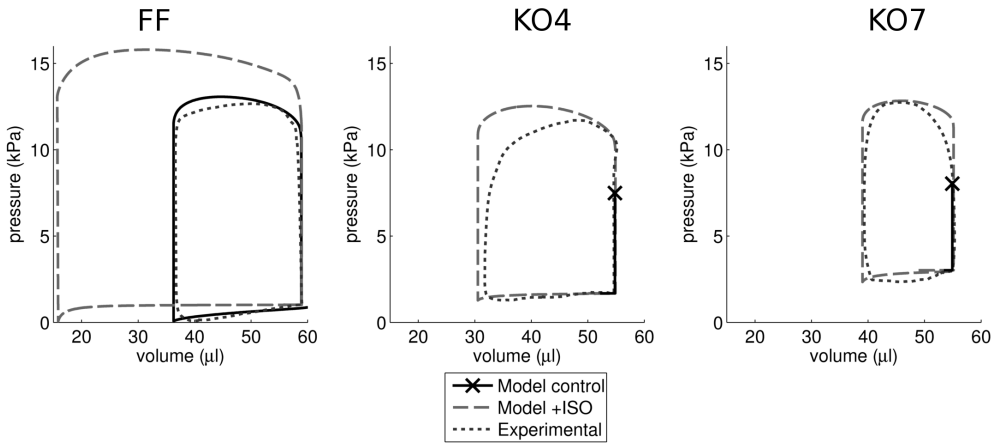

Figure 5.4: Pressure-volume loops from simulations based on calcium transients without ('control') and with ('+ISO') isoproterenol, compared to experimental PV data. Panels show results in FF, KO4 and KO7 mice from left to right. For simulations which do not reach ejection, maximal pressure is indicated by an 'x'.

Fig. 5.4. presents the resulting pressure-volume loops from simulations where the six representative calcium transients were used as input for simulations, alongside a comparison with experimental data. Firstly, they show that the control FF calcium is a good match for the ventricular function observed experimentally, as in the last chapter. Next, they demonstrate that control calcium transients in KO mice are incompatible with observed whole heart function, as the predicted maximum pressures of 7-8 kPa are not sufficient to initiate ejection. Using calcium transients measured following the addition of isoproterenol results in a different response to Serca2 knockout. Here the FF mice have an ejection fraction larger than observed experimentally, which is to be expected considering the increase in the magnitude of the calcium transient, and the match of the control transient. However, using KO+ISO calcium transients results in a PV loop that matches experimental data, resulting in a healthy ejection fraction in KO4 mice, and a reduced but still viable cardiac function in KO7 mice. As can be seen in both experimental and simulation results, end-diastolic pressure is significantly increased in knockout mice. This corresponds to increased residual tension, a result of the increasing diastolic calcium seen in KO+ISO calcium transients. To match end-diastolic volume at the measured pressure, a small reduction in the calcium sensitivity is required. This change is also consistent with higher β-adrenergic state, which is known to affect the affinity of TnC for calcium.

Fig. 5.5 shows deformation for FF, KO4 and KO7 mice from simulations. This visualization shows the striking similarities in ejection, especially between FF and KO4, regardless of differences in IVC and IVR. In KO7, ejection is markedly decreased even following a more rapid IVC phase faster due to higher residual tension.

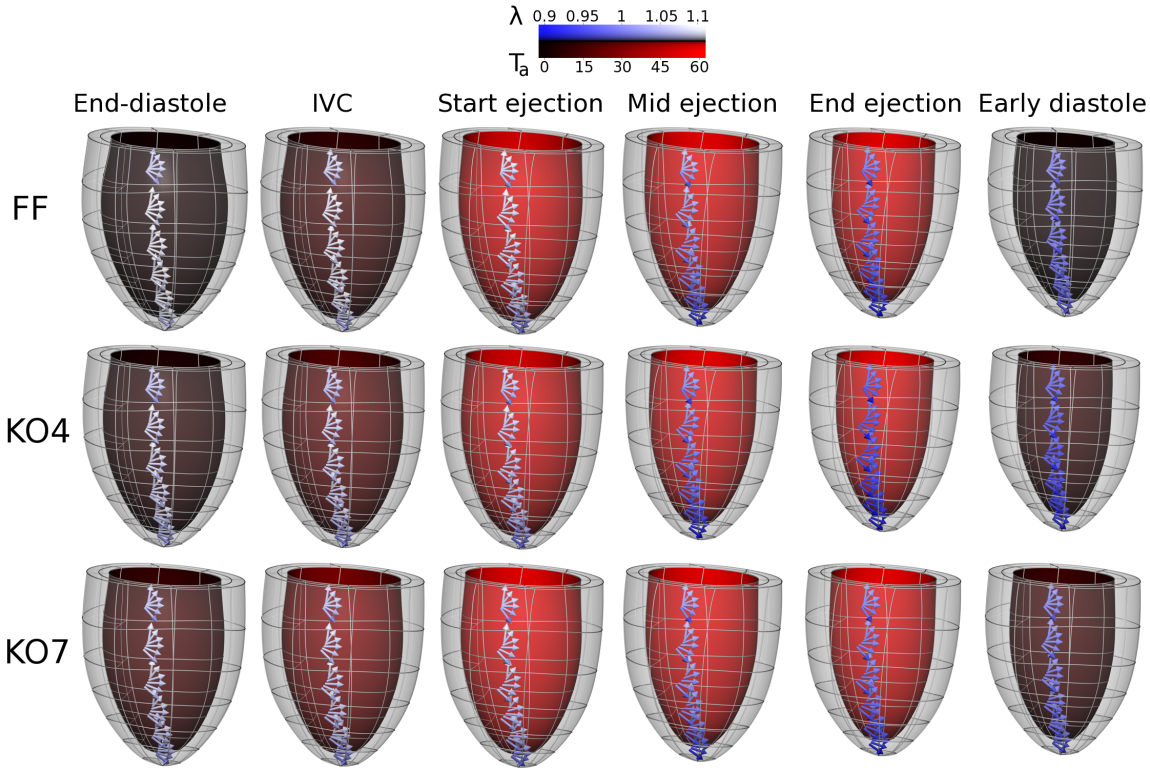

Figure 5.5: Deformation from simulations based on FF control, KO4+ISO and KO7+ISO. Surfaces are colored according to active tension, and fiber direction arrows are colored according to fiber strain, as shown in the legend. Top row shows FF at end-diastole, mid IVC, beginning, mid, end ejection, and beginning of diastole. Middle row shows KO4, and bottom row KO7.

5.5 Active tension estimation

Since comparing pressure-volume loops can obscure temporal differences in results, we also investigated whole-organ tension development. Performing such comparisons requires an estimate of active tension from experimental results. As this can not be obtained directly, we use our computational framework as a basis for estimating active tension in vivo. Specifically, mean active tension was estimated by prescribing pressure and solving for tension to match volume in the mechanics solution process, using the pressure-volume measurements described in the previous section.

As described in Chapter 3, in a nonlinear solve of high order finite element mechanics problem, we solve the node positions and hydrostatic pressure given the balance of forces discretized as $R_{kj}(\tilde{\mathbf{x}}, \tilde{\mathbf{p}}) = 0$ and incompressibility discretized as $(Q_k(\tilde{\mathbf{x}}) = 0)$ as constraints. The general idea of our method is to add a mean active tension variable $\overline{T_a}$ to the vector of variables to be solved, and a volume constraint $v_{\text{lv}} = v_{\text{pv}}(t)$ as an extra equation. The mean tension $\overline{T_a}$ that is estimated will include some averaged velocity-dependent response, as well as averaged length-dependent binding and differences in activation time.

Monolithically solving for this extra variable results in extra entries in the Jacobian $\frac{dR_{kj}}{d\overline{T_a}}$, which can be calculated using finite differences, and $\frac{dv_{\text{lv}}}{d\tilde{\mathbf{x}}}$ likewise, as done before in Windkessel models. The remaining terms $\frac{dQ_k}{d\overline{T_a}}, \frac{dv_{\text{lv}}}{d\overline{T_a}}$ are 0, as $v_{\text{lv}}, \det F$ are not directly dependent on T_a in the residual evaluation.

The resulting solution process is as fast as a normal mechanics solution process, and can be executed with the 1 ms time step given by the PV data resolution. However, some initial estimate of the deformation helps convergence at higher pressures, and can be obtained by inflating the ventricle up to approximately the volume seen in the first time step.

The tension estimation technique was validated using the results of Chapter 4. In this validation it showed $< 10\%$ error in estimating mean active tension in the most complex simulation case where tension development was heterogeneously activated and length- and velocity dependent. As this validation showed that the assumption of homogeneous tension development does not lead to significant errors in estimating the mean active tension, we can use this a metric to combine pressure and volume transients to a single experimental value which can be easily compared to simulated cellular and whole-organ tension development. It also allowed for the visualization shown in Figure 5.2, which shows the hypothesised connection between cellular calcium and ventricular tension generation.

5.5.1 Results

Fig. 5.6 shows mean active tension estimated from experimental PV data compared to active tension from these six simulated cases. This comparison of simulation results to estimated tension traces demonstrate more clearly the unphysiological results produced by the +ISO transient in FF mice, as after the usual fast decrease in tension development at the beginning of ejection due to the velocity dependent effects of fast shortening, there is a

second phase of tension development, leading to a peak tension twice as high as estimated from experimental data. The FF control transient shows good agreement during isovolumetric contraction and relaxation, although some differences appear during isovolumetric relaxation. This may be in part due to a small disparity in stimulation frequency.

In comparison, the control transients in KO mice were too small to result in the contraction observed in measurements, as peak tension developed is approximately half of that required, even when length-dependent activation is maximal during the entire transient due to failure to start ejection. The KO+ISO transients also show good agreement during ejection, although especially the KO7 transient has slower relaxation. As this PV loop was measured with an identical 6 Hz heart rate as the matching calcium transient, the disparity between model prediction and experimental results in these mice can not be attributed to such factors.

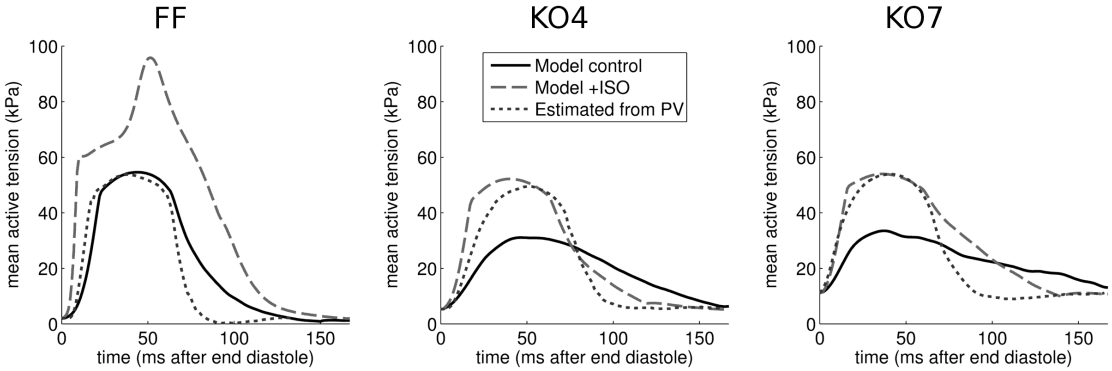

Figure 5.6: Active tension from simulations compared to active tension estimated from PV data. Simulations were based on calcium transients without ('control') and with ('+ISO') isoproterenol, and compared to active tension estimated from PV data. Panels show results in FF, KO4 and KO7 mice from left to right, all aligned by end-diastole. Heart rates for simulations, and experimental data for KO4 and KO7 are 6 Hz, and experimental data for FF is at 7.5 Hz.

5.6 Parameter variation

In this section we investigate the necessity of β-adrenergic stimulation in light of the assumptions inherent in a contraction model developed in the previous chapter. This supports the simulations above, where only the calcium sensitivity $[Ca^{2+}]^{\mathrm{ref}}_{\mathrm{T50}}$ was changed. In doing so we quantify our initial intuitions about the unlikeliness of compensatory contractile mechanisms. In each of these simulations, the calcium sensitivity $[Ca^{2+}]^{\mathrm{ref}}_{\mathrm{T50}}$ was fitted individually as in previous simulations, after variation of fundamental contractile parameters: the Hill coefficient for cooperative crossbridge action n_{xb}, the reference maximal isometric tension T_{ref}, and the magnitude of length-dependent activation effects β_1. We also investigated changing the rate constants, the unbinding rate of calcium from TnC, k_{TRPN} and the scaling factor for rate of crossbridge binding k_{xb}. These simulations were

only performed for the KO4 and KO7 mouse models, as the FF model already shows realistic contraction under control conditions.

5.6.1 Results

Table 5.2 and Figure 5.7 shows the results for alternate contraction models in the KO4 and KO7 control cases.

In the KO4 model, doubling the rate constants $k_{\mathrm{TRPN}}, k_{\mathrm{xb}}$ has little effect. Increasing the cooperativity of crossbridge binding from $n_{\mathrm{xb}} = 5$ to $n_{\mathrm{xb}} = 7$ has the greatest effect, but simulation results are still far from experimental traces. Furthermore, this change leads to an F-pCa Hill curve fit with Hill coefficient of 9.1, and biphasic fit with coefficients 10.8 and 5.1 for the lower and upper half respectively, which exceeds experimentally measured Hill coefficients (Dobesh et al., 2002).

Increasing the reference tension to 240 kPa results in only a small increase in the the maximum pressure, as it requires a lower calcium sensitivity to match end-diastolic state. Finally, maximum pressure increased by *decreasing* the magnitude of length-dependent activation (LDA) factor β_1. This possibly counterintuitive mechanism is related to the fact that calcium sensitivity has to be decreased significantly at higher LDA to match residual tension. Lowering LDA thus allows for higher sensitivity to calcium, and slightly higher developed tension. This lower length dependence also results in a cellular response significantly lower than the length dependence seen in experiments.

In KO7 mice the balance between required changes in calcium sensitivity and maximum pressure changes in some cases. However the overall conclusions remain the same: only changes in reference tension and cooperativity beyond plausible experimental values have the potential to significantly increase maximum pressure. In the KO7 case there is no ejection in any simulation, which further demonstrates that the control calcium transients are incompatible with whole-organ function observed. This confirms our preliminary results and shows the necessity of β-adrenergic stimulation in maintaining cardiac function in knockout mice, as even large compensatory changes in myofilament properties do not result in viable cardiac output.

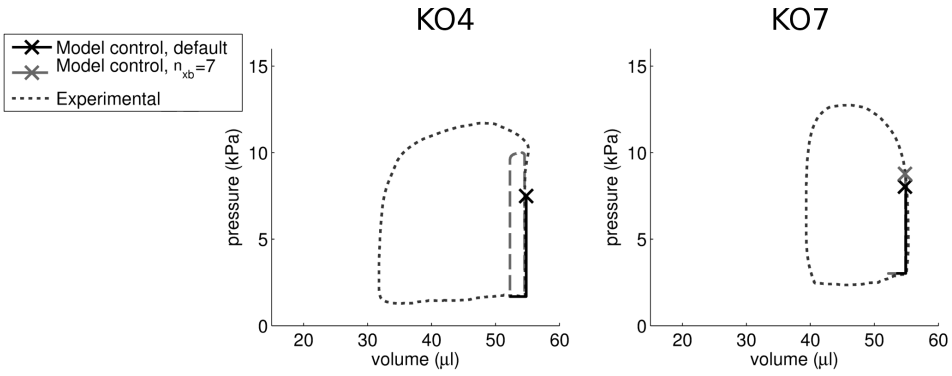

Figure 5.7: Pressure-volume loops for parameter variations. Pressure-volume loops from the 'original' and $n_{\mathrm{xb}} = 7$ simulations shown in Table 5.2, compared to experimental PV loops.

	KO4		KO7	
Parameter	$[Ca^{2+}]^{ref}_{T50}$	Max. pressure	$[Ca^{2+}]^{ref}_{T50}$	Max. pressure
original	0.469	7.5 kPa	0.423	8.0 kPa
$k_{TRPN} = 0.2/ms$	0.470	7.5 kPa	0.429	7.7 kPa
$k_{xb} = 0.2/ms$	0.469	7.5 kPa	0.426	7.9 kPa
$n_{xb} = 7$	0.420	10.0 kPa	0.399	8.8 kPa
$T_{ref} = 240$ kPa	0.511	8.6 kPa	0.469	8.6 kPa
$\beta_1 = -0.75$	0.446	7.7 kPa	0.412	7.4 kPa

Table 5.2: Whole-organ response to changes in the contraction model. Using control calcium for KO4 and KO7 mice. Shown are the necessary change in $[Ca^{2+}]^{ref}_{T50}$ to match end-diastolic state, and resulting maximal pressure developed. The relevant original contraction model parameters are: Hill coefficient for cooperative crossbridge action, $n_{xb} = 5$. Unbinding rate of calcium from TnC, $k_{TRPN} = 0.1$. Scaling factor for rate of crossbridge binding, $k_{xb} = 0.1/ms$. Reference maximal isometric tension, $T_{ref} = 120$ kPa. Magnitude of length-dependent activation effects, $\beta_1 = -1.5$.

5.7 Discussion

In this chapter we applied our electromechanical mouse modelling framework to investigate novel experimental measurements of Serca2 knockout mice at both the single cell and whole-organ levels. In doing so we have been able to explain the progression of heart failure in these knockout mice.

Previous work had already identified several mechanisms that compensate for changes in the calcium transients, including upregulated L-type calcium and NCX, change in SR volume and growth of T-tubules. In light of this previous work it was originally expected that the moderate decrease in heart function could be explained largely by previously identified changes in the calcium transient, combined with compensatory changes in contractile parameters. However, early investigation of this hypothesis revealed the drastically different contractile response to identical calcium concentrations that would be required to explain the changes from FF to KO4 and from KO4 to KO7. Although in FF mice, predicting cardiac function using control calcium transients shows realistic pressure and tension development and ejection consistent with experimental measurements and previous modelling in Chapter 4, predictions in KO mice showed large quantitative differences. Even when pushing single cell models to parameter space regions far outside the range of experimental data to reproduce diastolic and systolic tension levels, tension shape was significantly different from estimated traces from PV loops. Thus, although the decrease in heart function combined with a decrease in measured calcium transients were previously considered to qualitatively compatible, modelling results revealed a significant quantitative gap in our understanding. Combined with preliminary experimental evidence suggesting the importance of β-adrenergic state (Andersson et al., 2009a), these results drove our experimental collaborators to collect additional data on the effects of β-adrenergic stimulation on the cellular measurements.

In FF mice, these additional measurents with added isoproterenol shows unrealistic tension development in the model due to velocity dependent effects during fast shortening, as well as producing a stroke volume significantly greater than values measured experimentally. Furthermore, a higher calcium sensitivity of the contractile proteins is needed to explain the diastolic tension observed experimentally when diastolic calcium is lowered by upregulated SERCA. In contrast, β-adrenergic stimulation generally causes *lower* calcium sensitivity due to the effects of PKA on TnI and TnC (Metzger and Westfall, 2004). These results contrast with those obtained in KO4 and KO7 mice, in which control calcium transients are far too small to result in the ejection observed, and can not sustain the systolic tension observed even when taking into account the fact that diastolic tension is significantly elevated. Furthermore, the observed reductions in calcium transient of $> 70\%$ are too large to be consistent with minor changes in contractile function. With β-adrenergically stimulated calcium transients, simulations matched observed PV data, showing realistic ejection and tension development. Matching diastolic tension in the model required a decrease in calcium sensitivity between control and KO+ISO contraction, which is due to higher diastolic calcium. This small decrease in calcium sensitivity

from FF control to KO+ISO is also consistent with the effects of β-adrenergic stimulation.

From these results we can now provide a novel interpretation of the progression of heart failure and compensatory mechanisms which result from Serca2 gene knockout. Several electrophysiological mechanisms quickly compensate for the decrease in SERCA. Firstly, in the absence of β-adrenergic stimulation, transmembrane calcium dynamics are upregulated to improve the calcium transient (Li et al., 2012). Activation of the L-type calcium channel through β-adrenergic stimulation increases the calcium transient further, preserving systolic calcium levels to be close to those normally observed in healthy mice. However, in the absence of SERCA this upregulation of the L-type calcium channel through multiple mechanisms causes net transmembrane removal of calcium through NCX and PMCA to be insufficient to maintain diastolic calcium at healthy levels (Louch et al., 2010). As the size of the calcium transient decreases with increasing diastolic calcium, either diastolic tension must increase, or systolic tension must decrease. Consistent with maintaining cardiac pump function and preventing systolic heart failure, systolic tension is maintained while diastolic tension increases significantly. Finally, the resulting higher diastolic tension is compensated for through higher minimum and end-diastolic pressure, which indicates a higher venous return pressure. Venous return is also known to be increased by β-adrenergic stimulation, through venodilation and lower splanchnic venous resistance (Green, 1977). This further ensures systolic tension can be maintained through effective length dependence of tension development, by maintaining end-diastolic volume even in the presence of this significantly higher diastolic active tension. From our modelling results and measurements of blood catecholamine and calcium transients, we can infer that there is not a loss of beta-adrenergic signalling or responsiveness at the 7 week point, but a limit on to what extent these effects can compensate for the failing calcium dynamics. Increasingly severe heart failure develops as the β-adrenergic state and venous return pressure can no longer be increased, while calcium cycling progressively declines, possibly further exacerbated by acidosis, Na^+ accumulation, and increased ATP consumption (Louch et al., 2010; Li et al., 2012). In this fragile state, further increases in diastolic calcium can quickly lead to decreased end-diastolic volume and reduced contractility, resulting in death from heart failure. In support of this view, preliminary experimental observations suggest that in vivo cardiac function rapidly and markedly declines in knockout mice following the 7-week time point.

The effects of β-adrenergic stimulation in these mice can also be contrasted with the use of β-blockers in humans. In humans, the effects of sympathetic stimulation are often blocked with β-blockers, making them an effective treatment for a range of heart diseases (Frishman and Saunders, 2011). By contrast, KO animals appear dependent on continuous β-adrenergic stimulation for survival. Importantly, through actions in the kidneys, β-adrenergic stimulation promotes fluid retention and increased venous return, which are traditionally considered deleterious in heart failure. However, in the KO mice such an increase in pre-load appears to be essential in enabling filling of the ventricle despite increased diastolic active tension. In heart failure, β-adrenergic stimulation is generally associated with arrhythmogenesis due to overloading of the SR, and thus spontaneous cal-

cium release (Venetucci et al., 2007). In the KO mice, such spontaneous release events are inhibited due to the low SR content, and thus the pro-arrhythmic danger of β-adrenergic stimulation appears to be avoided. Finally, a detrimental increase in heart rate expected with greater β-adrenergic tone does not occur in KO mice; in fact a mild decrease in heart rate was observed in these mice (Andersson et al., 2009a). This may be due to the role of SERCA2 in sinoatrial node cells (Maltsev and Lakatta, 2010), which are partially affected by the knockout. Thus, there appears to be several advantages to increased β-adrenergic stimulation in the Serca2 KO mice, without the largely negative effects associated with sympathetic stimulation in other types of chronic heart failure. However, these conclusions have to be seen in light of the limitations of animal models discussed in section 2.2.4. The possibility of specific side-effects on the sinoatrial node, combined with quantitative differences in the role of SERCA in calcium cycling, means it remains to be seen whether these discoveries are applicable to human heart disease.

A potential limitation of our study is that further effects of β-adrenergic stimulation on the myofilaments could play a role in this larger difference in relaxation kinetics remaining between simulations and measurements. However, doubling the rate constant for crossbridges k_{xb} did not improve relaxation, suggesting that relaxation is dominated by the calcium transient decay rate in simulations. A futher limitation derived from our experimental data is that we have only considered very high and no β-adrenergic stimulation. Although ejection predicted from KO4 +ISO calcium data is slightly higher compared to PV data, within the limits of uncertainty of the experimental data, it is difficult to say whether β-adrenergic stimulation is already near maximal in KO4 mice. Previously measured blood catecholamine levels are elevated in knockout mice, with norepinephrine levels of 84.4 ± 10.3 in KO7 mice compared to 54.8 ± 7.3 mg/g in FF controls, and epinephrine levels of 5.1 ± 1.8 mg/g in KO7 and 2.5 ± 5.1 mg/g in FF mice (Andersson et al., 2009a). As blood catecholamines are spillover from nerve terminals, these measurements can not be easily converted into equivalent stimulation at the single cell level. Furthermore, although the β-adrenergic response does not appear to be significant in FF mice, where control calcium transients adequately explain whole-organ ejection, this response may be easily missed in other experimental studies. Addition of isoproterenol to single cell experiments is common, but connecting this to the level of stimulation in vivo remains difficult.

Our results add significantly to a better understanding of Serca2 knockout, and thus allow us to reinterpret a significant amount of previous work. Firstly, the study in which the knockout mice are developed (Andersson et al., 2009b) cites previous work by Schultz et al. (2004) which shows that heterozygous knockout mice are generally healthy, though more sensitive to increased pressure. Furthermore, increased end-diastolic pressure was observed in heterozygous knockout mice. This suggests that β-adrenergic stimulation may also play an important role in heterozygous knockout mice.

Secondly, there was a follow-up study by Andersson et al. (2009a), which measured both cellular and whole-organ response to Serca2 knockout. They also note significant atrial dilation, which is likely related to the higher venous return pressure. Results further show low shortening in isolated myocytes, with FF and KO4 cells having equal fractional

shortening. Even at 1 Hz when calcium transients are larger, shortening is lower than consistent with ventricular ejection. From these results they conclude there was enhanced myofilament responsiveness, while our results demonstrate a small decrease in calcium sensitivity instead. They also show plasma norepinephrine is significantly increased. Furthermore, plasma epinephrine increased in KO, though this was not significant due to variability. However, only limited measurements of these effects at low pacing rates were performed, and future studies do not incorporate these results.

The study by Louch et al. (2010) confirmed the increasing left atrial diameter, maintained diastolic calcium and a fractional shortening of only 1.4% in KO7 cells. They furthermore observed increasing pulmonary congestion in knockout, which further explains the higher end-diastolic pressure which is necessary for effective length-dependent activation of the myofilaments. A major conclusion of their study is the decrease in calcium extrusion due to Na^+ accumulation and declining SERCA, which slows the decay of the calcium transient in their study. From our results we can see that this is likely to be a major factor in the increased diastolic calcium. Finally, the recent study by Swift et al. (2012) shows a decrease in SR volume, along with T-tubule in Serca2 knockout mice. This provides a further mechanism for increased L-type calcium influx underlying the maintained systolic calcium we observed.

In mathematical modelling, the study by Li et al. (2011) developed a model of the electrophysiology and calcium dynamics in FF and KO4 mice. This model still accurately represents the cellular data in FF mice. However, some of its key conclusions have to be adjusted in light of our research. The study contrasts the increase in diastolic calcium in failing human myocardium with a lack of increase in these mouse models, stresses the importance of NCX upregulation in maintaining diastolic calcium levels in KO mice equal to FF controls, and suggests the absence of hypertrophy is related to maintaining diastolic function. Our results show that diastolic function is indeed impaired, and diastolic tension and calcium are significantly elevated in vivo. However, these results do not diminish the importance of NCX upregulation in reaching this higher, but still viable, diastolic calcium. The study also suggests that changes in calcium sensitivity may be sufficient to compensate for the lower systolic calcium, which our modelling efforts have shown to be implausible, as calcium transients are too small. Their conclusions that cellular compensatory mechanisms maintain diastolic function can now be contrasted with our results, which demonstrate that in vivo, cellular response is maintaining systolic calcium. These contrasting results are indicative of complex genetic and regulatory systems in the cell that maintain aspects of calcium dynamics, and much work is required in this area before this can be fully understood.

The investigation of cellular electrophysiology using mathematical models was continued in the follow-up study by Li et al. (2012) which explored the progression of changes in electrophysiology and calcium dynamics from FF to KO4 to KO7 cells at 1 Hz, in an attempt to understand the transition point from healthy cellular function due to compensation, to a critical point of decreased cardiac function. In their conclusions these researchers suggest that KO4 control transients are sufficient to maintain diastolic and

systolic heart function, and systolic heart failure in KO7 mice is explained by a further decrease in systolic calcium. In practice under β-adrenergic stimulated KO7 mice there is a small decrease in the calcium transient combined with a small decrease in calcium sensitivity, which is likely to drive the decrease in ejection fraction, while there is major degeneration of healthy diastolic function. They also stress the role of ATP consumption and acidosis. Although their analysis is dependent on non-β-adrenergically stimulated calcium transients and likely to have large quantitative errors compared to the in-vivo state, actual ATP consumption is likely to be even higher in vivo.

The need for reinterpretation of previous research in light of the importance of the β-adrenergic response also raises questions for the use of cellular experimental data in multiscale modelling in general. In multi-scale modelling, cell models based on isolated cells are often assumed to perfectly describe whole-organ behaviour. As we have shown in the last two chapters, even when using a carefully species-specific model at a physiological temperature and pacing frequency, such an assumption may be incorrect. In this context, our experimental data also reveals some of the disadvantages of using isolated cell preparations. While the cell environment is carefully controlled, isolated cell behaviour can be significantly different in comparison to in vivo function, as important regulatory factors of calcium dynamics, such as β-adrenergic stimulation, changing sarcomere length and circulatory factors, are missing. Furthermore many such measurements are already known to be significantly different from in vivo cellular function, due to factors such as tension rundown and changes in cooperativity. Our results therefore show an important role for computational modelling in quantifying the connection between single cell and whole organ function. Whereas the decreased calcium transients seen in the knockout mice may initially seem compatible with the observed decrease in heart function, modelling results demonstrate that more significant changes are needed, which can only be induced by high β-adrenergic stimulation.

In conclusion, our results show that β-adrenergic stimulation is an essential factor in explaining the observed changes from FF to KO mice and the relatively slow development of heart failure after a major disruption in normal cellular function. Thus, the Serca2 knockout mice are kept alive by a constant state of 'fight-or-flight', much like the panicked mouse described by Robert Burns in the epigraph to this chapter.

Chapter 6

Conclusions and future directions

This thesis presented an integrative framework for computational modelling of electromechanics in the mouse, and its application to several physiological questions: the role of electromechanical coupling mechanisms in generating ventricular pressure, and the progression of heart failure progression after genetic knockout. To accomplish this, significant work was required both in implementation of a coupled multi-physics model, as well as mathematical model development in the mouse across cellular and tissue scales. This chapter summarizes the main conclusions, and discusses opportunities for improvement and other future work.

6.1 Computational methods

In Chapter 3, we developed a computational framework for electromechanics. This framework has proven to be especially suitable for our further research in electromechanical mouse models, due to the efficient mechanics solver. The combination of predicting the next solution, combined with a modified Newton method, results in a speed-up of up to approximately a factor 50. Whereas previous studies using electromechanical models have usually been based on a few results or required large supercomputing facilities, the development of efficient computational methods has allowed for large parameter variation studies consisting of many simulations to be performed on a standard desktop computer. Using such a large number of results we can look at the effect of a broader range of parameters, and obtain a better understanding of the important components in a ventricular model, thereby allowing us to identify or exclude other potential mechanisms which might also explain differences between experimental and simulation data.

The mechanics solver developed here is currently in use by several other researchers, including Xi et al. (2011, 2012) in mechanical parameter estimation studies and Øyvind Nordbø et al. in parameter variation studies. In both cases, an efficient implementation has proven to be very useful in running many simulations without the need for supercomputing facilities. However, the tools are currently still closed-source and not available for general use. An important step in future work is making the proposed methods more widely

available.

Some aspects of mechanical simulations remain challenging, and are open for improvement in future work. The optimal choice of boundary conditions is one of these. Extending mechanical simulations to include tissue up to the valve plane would allow for comparison of different types of boundary conditions in truncated ventricular models. However, there are significant challenges in performing such a comparison, as MRI data often does not include details of the valve plane, many current tools for mesh generation are optimized for truncated data, and the material properties of the collagen-rich valve plane are different from that of the myocardium. Another aspect is the numerical stability of nonlinear mechanics simulations, which can be highly dependent on both model parameters and the computational mesh used. Recent work by Lamata et al. (2013) has looked into this problem in more detail, but as of yet no clear answers are available.

6.2 Electromechanical model of the mouse

The main contribution resulting from this thesis is a novel species- and temperature specific framework for electromechanical modelling of mice based on a range of multimodal experimental data. This modelling framework is based on the computational methods developed and includes a cell contraction model based on a wide range of data from the literature, which accurately represents the dynamics of murine myocytes under physiological conditions.

At the basis of this electromechanical model is a novel cellular contraction model based primarily on existing data from the literature. To investigate parameter identifiability of the contraction model with respect to this experimental data, we developed a novel visualization method. This visualization shows which parameters in this model are already well determined, and where additional experimental data could help further model development. At the cellular scale we also found that the strongly biphasic force-pCa relation previously reported can be explained by cooperative binding of calcium to troponin C. Specifically, while a single cooperative mechanisms can reproduce a biphasic force-pCa curve, the combination of two cooperative processes interacting is what leads to quantitative agreement with previously published experimental data.

A natural extension of this work in the future is the application of this modelling framework to represent cardiac cellular contraction in other species. We are currently working on the development of a human contraction model, using human cells that have recently become available to our collaborators. This will allow us to test the effect of electromechanical coupling mechanisms in human heart models, and creates opportunities for investigating similarities and differences between human and mouse cellular contraction.

The cellular contraction model was embedded in a model of the left ventricle of a mouse, parametrized using new multimodal experimental data, including MRI data, pressure-volume loops, and passive inflation experiments. In study of electromechanical coupling mechanisms in this Chapter, we have shown that running whole-organ simulations can

assist in the inference of aspects of length- and velocity dependent feedback at the cellular scale, for which data are still insufficient or contradictory. Investigating the effects of different length-dependent mechanisms on the dynamics of ejection and isovolumetric relaxation in the ventricle strongly suggest that length-dependent activation factors are dominant, considering their relative effect on ejection and relaxation. Perhaps more importantly, we were able to use emergent function in whole-organ simulations to show the importance of a strong velocity-dependent effect on tension in reproducing pressure transients seen in vivo. Introducing a stronger velocity dependence resulted in a longer duration of ejection, with a lower and extended pressure plateau during ejection, rather than a pressure transient which is similar to single-cell tension transients. Results from an extensive parameter variation study show that this is a necessary change to explain pressure transients, as other parameters in the model are either constrained from experimental data or do not explain differences between model results and experimental data.

The detailed whole-organ simulations uncovered significant effects of the electrical propagation on the calcium transient in our tissue model, as the L-type calcium current is significantly increased just after the upstroke, when cells are driving action potential propagation and act as a source for neighbouring tissue. This raises questions about the extent these mechanism play a role in vivo as well as the effects of isolating boundary conditions in models and experiments. However, using newer electrophysiology models (Li et al., 2012), these effects do not appear. This is most likely due to differences in modelling calcium-induced deactivation of L-type calcium channels, which are highly dependent on the parametrization and use of calcium subspaces, which differ in their formulations between the different models. It is still unclear which of these models is more realistic, although the lack of effect in more detailed models, combined with the fact that directly using cellular calcium transients in Chapter 5 matches experimental data well, suggests that the increase in the L-type calcium current may be an artefact of older models. A potential direction for future work in this area is to assess the predictive value of electrophysiological cell models in a tissue environment more generally, as the electrical stimulus a cell receives in vivo can be very different from that usually applied during in vitro experiments.

There are currently still some differences between the predictions of the whole-organ model and experimental measurements during late isovolumetric relaxation. The predicted rate of relaxation is slower in whole-organ models compared to experiments, whereas isometric tension development in our contraction model matches experimental single cell data well due to the cooperative term in unbinding. Although these differences are on the 1/100 second scale, such differences can be significant in mice. In Chapter 5 we found this difference to be especially significant when looking at estimated tension transients in KO7 mice. These discrepancies are still not fully explained, and may point to other coupling mechanisms. A potential explanation is the shortening-induced cooperative deactivation mentioned in the literature (Hanft et al., 2008), which is not included in the contraction model as this mechanism remains difficult to quantify. As future work in this area progresses, our model should be updated to include such mechanisms.

The initial stimulus for electrical activation in our electromechanical model was based on the end-points of the specialized conduction system. This stimulus pattern was a simplified representation, which could be further refined in future work. However, due to fast murine electrical activation, it was not significantly different from homogeneous activation, and may not significantly impact the predictive value of a ventricular mechanics model of the mouse. Nevertheless, the impact of the specialized conduction system on the timing of electrical activation is often neglected in electromechanical models of all species. These effects are likely to be more significant than the small changes in conduction velocity that have been the focus of much research in numerical methods for the monodomain and bidomain models. Finding an appropriate balance between accuracy, speed, and complexity for models of cardiac electrical activation is likely to remain important for future work in electromechanical modelling.

6.3 Genetic knockout model

In Chapter 5 we used our electromechanical modelling framework to investigate the progression of heart failure in genetically modified mice, which have an induced cardiomyocyte specific knockout of the Serca2 gene. This particular genetic knockout is lethal in utero, and only inducing a knockout in adult mice allows for investigating the effects of such a drastic change in cellular function. Mice with an induced knockout can live for seven to ten weeks after introduction of tamoxifen, staying alive with large reduction in SERCA pump function.

Measurements of calcium transients were used as input for our mouse modelling framework, in the absence and presence of isoproterenol. The modelling efforts described in Chapter 5 demonstrated the importance of β-adrenergic stimulation for maintaining heart function in Serca2 knockout mice. More detailed work on changes in myofilament properties also confirmed the implausibility of alternate mechanisms.

The newer electrophysiology models for knockout mice developed by Li et al. (2012) were not extended to reproduce calcium dynamics at 6 Hz, or the effects of β-adrenergic stimulation on calcium dynamics, making them of limited use for making connections to whole-organ data in our study. Thus, as a result of limitations we discovered in these models of cellular electrophysiology, we used direct measurements of calcium transients as input to our electromechanical model simulations instead. These particular limitations have motivated collaborators in Oslo to consider a reparametrization of the electrophysiology model using the metamodelling techniques developed in Tøndel et al. (2011, 2012), Vik et al. (2011).

Our work also makes several novel experimental predictions, which could be tested in future work. Firstly, an interesting opportunity for future work would be to characterize the effect of β-blockers on the progression of heart function in Serca2 knockout mice. According to our model predictions, Serca2 knockout mice will likely die before the 4 week time point in the absence of high β-adrenergic stimulation.

We have also suggested that heterozygous knockout animals are able to fully com-

pensate for their knockout by a lower level of β-adrenergic stimulation. Measurements of catecholamine levels, or experiments with β-blockers could confirm these predictions.

As we have shown, computational modelling can play an important role in making connections between cellular and whole-organ measurements. In doing so it can compensate for the lack of a few specific experimental measurements, such as the level of β-adrenergic stimulation in vivo or the magnitude of velocity-dependent effects. This observation is likely to guide us in future work, as we continue to use multiscale modelling to integrate experimental data between spatial scales and different species.

6.4 Summary

In this thesis we have developed an integrative framework for computational modelling of cardiac electromechanics in the mouse, allowing in-silico investigation of many experiments done in these animals. This framework has already shown potential for improving our understanding of cardiac function at both the single-cell and whole-organ level, by revealing the role of coupling mechanisms in explaining the striking differences between the shapes of cellular tension and ventricular pressure transients. Furthermore, through combining novel experimental data and our modelling framework we have sought to explain the progression of heart failure in Serca2 knockout mice, and identified increased β-adrenergic stimulation as the major compensatory mechanism. The development of this framework opens up many opportunities for future work, including improvements to models, applications to other mouse studies, and translation across species.

Appendix A

List of publications

The following publications contain material directly related to this thesis.

Research paper	**Sander Land**, Steven Niederer and Nicolas Smith. *Efficient computational methods for strongly coupled cardiac electromechanics*. IEEE Transactions on Biomedical Engineering, 2012
Conference poster	**Sander Land**, Steven Niederer, Øyvind Nordbø, Emil Espe, Ivar Sjaastad, William Louch, Stig Omholt, Ole Sejersted and Nicolas Smith *An electromechanical model of the mouse heart* Cardiac physiome meeting, Oxford, 2011
Research paper	**Sander Land**, Steven Niederer, Jan Magnus Aronsen, Emil Espe, Lili Zhang, William Louch, Ivar Sjaastad, Ole Sejersted and Nicolas Smith. *An analysis of deformation dependent electromechanical coupling in the mouse heart* Journal of Physiology, 2012
Conference abstract	**Sander Land**, Steven Niederer, Jan Magnus Aronsen, Emil Espe, Lili Zhang, William Louch, Ivar Sjaastad, Ole Sejersted and Nicolas Smith. *Developing a Virtual Physiological Mouse model of the heart: Multi-scale coupling is key for controlling ventricular pressure.* Virtual Physiological Human Conference, London, 2012
Research paper	**Sander Land**, William Louch, Steven Niederer, Jan Magnus Aronsen, Geir Christensen, Ivar Sjaastad, Ole Sejersted, Nicolas Smith. *Beta-adrenergic stimulation maintains cardiac function in Serca2 knockout mice* Biophysical Journal, 2013

The following work is the result of collaborations with other researchers, mostly related to aspects of the computational framework and mouse models developed in this thesis.

Research paper	S. A. Niederer, E. Kerfoot, A. P. Benson, M. O. Bernabeu, O. Bernus, C. P. Bradley, E. M. Cherry, R. H. Clayton, F. H. Fenton, A. Garny, E. Heidenreich, **S. Land**, M. Maleckar, P. Pathmanathan, G. Plank, J. F. Rodríguez, I. Roy, F. B. Sachse, G. Seemann, O. Skavhaug and N. P. Smith. *Verification of cardiac tissue electrophysiology simulators using an N-version benchmark.* Philosophical Transactions of the Royal Society A, 2011
Conference paper	Jiahe Xi, Pablo Lamata, Wenzhe Shi, Steven Niederer, **Sander Land**, Daniel Rueckert, Simon G. Duckett, Anoop K. Shetty, C. Aldo Rinaldi, Reza Razavi and Nic Smith. *An automatic data assimilation framework for patient-specific myocardial mechanical parameter estimation* Functional Imaging and Modeling of the Heart, 2011
Conference poster	Jiahe Xi, Pablo Lamata, Wenzhe Shi, Xiahai Zhyang, Steven Niederer, **Sander Land**, Daniel Rueckert, Sebastien Ourselin, Simon G. Duckett, Anoop K. Shett, C. Aldo Rinaldi, Reza Razavi and Nic Smith. *Patient-specific myocardial mechanical parameter estimation using an automatic data assimilation framework.* Cardiac physiome meeting, Oxford, 2011
Research paper	Steven Niederer, **Sander Land**, Stig Omholt, Nicolas Smith. *Interpreting cardiac genetics through models of cardiac electromechanics* American Journal of Physiology - Heart and Circulatory Physiology, 2012.
Research paper	Pablo Lamata, Ishani Roy, Bojan Blazevic, Andrew Crozier, **Sander Land**, Steven Niederer, Rod Hose, Nic Smith. *Quality metrics for high order meshes: analysis of the mechanical simulation of the heart beat* IEEE Transactions on Medical Imaging, 2013
Research paper	Jiahe Xi, Pablo Lamata, Steven Niederer, **Sander Land**, Wenzhe Sho, Xiahai Zhuang, Simon G. Duckett, Daniel Ruekcert, Reza Razavi, Nic Smith. *The estimation of patient-specific cardiac diastolic functions from clinical measurements* Journal of Medical Image Analysis, 2012

Appendix B

Experimental methods

The experiments on isolated myocytes described in Chapters 4 and 5 were performed by collaborators at Ullevål University Hospital in Oslo, Norway. The description of experimental methods was provided by Magnus Aronsen, William Louch and Emil Espe, and is duplicated here from (Land et al., 2012b, 2013) for completeness.

B.1 Ethics statement

Experiments were performed in accordance with the Norwegian Animal Welfare Act, which conforms to NIH guidelines (NIH publication No 85-23, revised 1996). Mice were housed at 55% humidity on a 12 h light/dark cycle, with food pellets (RM1, 801151, Scanbur BK) and water freely available.

B.2 Genetic background

Serca2$^{wt/flox}$ mice were generated by standard gene targeting strategies and backcrossed onto B6/J mice for at least 8 generations (Andersson et al., 2009b). Serca2$^{flox/flox}$ mice were then generated and interbred with MerCreMer transgenic mice (Sohal et al., 2001), which were also backcrossed onto B6/J mice, to create Serca2$^{flox/flox}$ Tg(αMHC-MerCreMer) knockout mice ('KO'). These mice allow for inducible, cardiomyocyte- specific disruption of the Serca2 gene in adult mice (Andersson et al., 2009a). Gene excision was accomplished in 8-10 week old mice by intraperitoneal injection of 1.0 mg of tamoxifen base (Sigma-Aldrich, Oslo, Norway) in peanut oil. Age matched Serca2$^{flox/flox}$ mice ('FF') served as controls.

B.3 Cell methods

FF and KO mice were sedated with a mixture of oxygen and 4.5% and 2.0% isoflurane, respectively, and then euthanized by neck dislocation. For cardiomyocyte isolation, hearts were rapidly excised and placed in cold isolation buffer containing (in mmol/L): 130 NaCl, 25 Hepes, 22 D-glucose, 5.4 KCl, 0.5 $MgCl_2$, 0.4 NaH_2PO_4, 0.01 µg/ml insulin (pH 7.4). Each heart was then cannulated via the aorta, mounted on a Langendorff apparatus, and perfused with isolation buffer supplemented with 200 U/ml collagenase Type II (Worthington Biochemical Corporation, Lakewood, NJ, USA) and 0.1 mmol/L Ca^{2+} at 30°C. Adequate digestion of the ventricles was generally achieved after 15 min of enzyme perfusion, at which point hearts were cut from the Langendorff aparatus. The left ventricular was then removed, mince, and gently shaken at 37°C for 3-4 min in the perfusion solution with the addition of 1% BSA and 0.02 U ml/L deoxyribonuclease I (Worthington). Following filtration (200 µm nylon mesh) and sedimentation, the cell pellet was washed in isolation buffer supplemented with 1% BSA and progressively increasing [Ca2+] (0.1, 0.2 and 0.5 mmol/L). Isolated cardiomyocytes were stored at room temperature until use.

For measurement of Ca^{2+} transients, cells were incubated with fluo-4 AM (20 µmol/L for 10 min, Molecular Probes, Eugene, OR), plated on laminin-coated coverslips, and mounted on the stage of an inverted microscope. Cells were then superfused with HEPES Tyrodes solution containing (in mmol/L): 140 NaCl, 1.0 $CaCl_2$, 0.5 $MgCl_2$, 5.0 HEPES, 5.5 glucose, 0.4 NaH_2PO_4, 5.4 KCl, pH 7.4, 37°C. Ca^{2+} transients were elicited by field stimulation at 6 Hz through platinum wires with a 3 ms biphasic pulse. Fluo-4 was excited at 485 nm, and whole-cell fluorescence at 535 nm was recorded by a photomultiplier tube (Photon Technology International, Monmouth Junction, NJ, USA). β-adrenergic stimulation was attained by exposing cells to 200 nmol/L isoproteronol, which we have observed is a maximal dose in other experiments.

B.4 In vivo pressure and volume measurements

Mice were sedated and anesthetized with a mixture of oxygen and 4.5% and 2.0% isoflurane, respectively. The right common carotid artery and right jugular vein were dissected, and the right jugular vein was cannulated for later saline injection. A 1.4F Millar PV-catheter was inserted retrogradely into the right common carotid artery and the aorta. Aortic blood pressure was recorded, before the catheter was further inserted into the left ventricular cavity (LV). LV PV-loops were recorded and later calibrated based on obtained values for stroke volume and parallel conductance (Pacher et al., 2008). Cardiac stroke volume was measured as blood flow through the aortic valve using echocardiography (Vevo 2100, VisualSonics, Canada), while the parallel conductance was obtained by injection of hypertonic (30%) saline into the right jugular vein and subsequently recordings of the displacement of the conductance signal. ECG was recorded simultaneously. Euthanasia was induced by an overdose of anesthesia followed by neck dislocation at the end of the

experiment.

B.5 Passive inflation experiments

Passive inflation was assessed by cannulating excised hearts and retrogradely perfusing via the aorta with a HEPES Tyrode buffer containing in (mM): 140 NaCl, 1.0 CaCl2, 0.5 MgCl2, 5.0 HEPES, 5.5 glucose, 0.4 NaH2PO4, 5.4 KCl, pH 7.4. The perfusion pressure was increased from 0 to 10 mmHg by elevating the perfusion buffer. Left ventricular dimensions were simultaneously assessed by echocardiography (VEVO 2100). Short axis images were obtained at the mid-ventricular level of the heart, and left ventricular length was assessed in apical 4-chamber view.

B.6 MRI experiments

The phase contrast MRI experiments were performed on a 9.4T/210mm/ASR horizontal bore magnet (Agilent/Varian Inc., US) with a high-performance actively shielded gradient coil (rise time 130 μs; max strength 1000 mT/m). Velocity encoding was performed by incorporating bipolar motion encoding gradients into an RF-spoiled, three-directional motion compensated gradient echo sequence (Herold et al., 2006).

Several mid-ventricular short-axis cardiac cine loops were recorded, covering the whole heart from base to apex. Slice planning was performed as described by Schneider et al. (2006). Acquisition was prospectively double-triggered by ECG and respiration. Anesthesia was induced in an anesthesia chamber with a mixture of O_2 and 4% isoflurane, and were further maintained by administration of a mixture of O_2 and 1.5-2.0% isoflurane in freely breathing animals. Heart rate, body temperature and respiration rate were constantly monitored during experiments. The level of anesthesia was regulated to keep the heart rate as close to 450 bpm as practically possible, and the body temperature was maintained by heated air. The imaging parameters were as follows: TE/TR = 2.7/3.8 ms; FOV = 25.6 × 25.6 mm; acquisition matrix 128 × 128; slice thickness = 1.00 mm; flip angle 7 degrees; receiver bandwidth = 156.25 kHz; venc = 11.5 cm/s; NA=4.

The resulting data sets were semi-automatically segmented and analyzed in a purpose-written Matlab (The MathWorks, Natick, USA) software. The segmentation masks were temporal dynamic, following in-plane motion of the myocardium.

Volume was estimated using a simple voxel count of the segmented cavity.

Appendix C

Image sources

- The cover image was programmatically generated using mathematical symbols from this thesis.
- Figure 2.1. obtained from Wikimedia Commons. See page for author(s).
  `http://commons.wikimedia.org/wiki/File:Diagram_of_the_human_heart_%28cropped%29.svg`
  Licensed under the Creative Commons Attribution-Share Alike 3.0 Unported license
  `http://creativecommons.org/licenses/by-sa/3.0/deed.en`
- Figure 2.3 was reproduced with permission from D. Bers. "Calcium Fluxes Involved in Control of Cardiac Myocyte Contraction." Circ. Res. 2000;87;p276" with permission from Wolters Kluwer Health.
- Figure 2.4 was reprinted from Trends in Cardiovascular Medicine, Volume 14, Issue 3, J.M. Nerbonne, "Studying Cardiac Arrhythmias in the MouseA Reasonable Model for Probing Mechanisms?" pages 83–93, Copyright (2004), with permission from Elsevier.
- Figure 2.5 was adapted from an image obtained from Wikimedia Commons. See page for author(s).
  `http://commons.wikimedia.org/wiki/File:Skeletal_muscle.jpg`
  Licensed under the Creative Commons Attribution-Share Alike 3.0 Unported license
  `http://creativecommons.org/licenses/by-sa/3.0/deed.en`
- Figure 2.6, available under the Creative Commons Attribution License, was reproduced from (Marcucci and Yanagida, 2012).
- Figure 2.7 was reproduced from David P. Dobesh, John P. Konhilas, Pieter P. de Tombe, "Cooperative activation in cardiac muscle: impact of sarcomere length" Am J Physiol - Heart and Circulatory Physiology, 2002 vol. 282 no. 3 H1055-H1062. 'Permission is not required for this type of use.'

Bibliography

J. Aguado-Sierra, A. Krishnamurthy, C. Villongco, J. Chuang, E. Howard, M. J. Gonzales, J. Omens, D. E. Krummen, S. Narayan, R. C. Kerckhoffs, and A. D. McCulloch. Patient-specific modeling of dyssynchronous heart failure: A case study. *Progress in Biophysics and Molecular Biology*, 107(1):147–155, October 2011.

D. Allen and J. Kentish. The cellular basis of the length-tension relation in cardiac muscle. *Journal of Molecular and Cellular Cardiology*, 17(9):821–840, September 1985.

R. H. Anderson, M. Smerup, D. Sanchez-Quintana, M. Loukas, and P. P. Lunkenheimer. The three-dimensional arrangement of the myocytes in the ventricular walls. *Clinical Anatomy*, 22(1):64–76, January 2009.

K. Andersson, J. Birkeland, A. Finsen, W. Louch, I. Sjaastad, Y. Wang, J. Chen, J. Molkentin, K. Chien, O. Sejersted, and G. Christensen. Moderate heart dysfunction in mice with inducible cardiomyocyte-specific excision of the Serca2 gene. *Journal of Molecular and Cellular Cardiology*, 47(2):180–187, 2009a.

K. B. Andersson, A. V. Finsen, C. Sjåland, L. H. Winer, I. Sjaastad, A. Odegaard, W. E. Louch, Y. Wang, J. Chen, K. R. Chien, O. M. Sejersted, and G. Christensen. Mice carrying a conditional Serca2$^{\text{flox}}$ allele for the generation of Ca^{2+} handling-deficient mouse models. *Cell Calcium*, 46(3):219–225, September 2009b.

A. Babu, E. Sonnenblick, and J. Gulati. Molecular basis for the influence of muscle length on myocardial performance. *Science*, 240(4848):74–76, January 1988.

L. C. Baker, B. London, B.-R. Choi, G. Koren, and G. Salama. Enhanced dispersion of repolarization and refractoriness in transgenic mouse hearts promotes reentrant ventricular tachycardia. *Circulation Research*, 86(4):396 –407, March 2000.

G. W. Beeler and H. Reuter. Reconstruction of the action potential of ventricular myocardial fibres. *The Journal of Physiology*, 268(1):177, 1977.

D. A. Bergel and P. J. Hunter. The mechanics of the heart. *Quantitative Cardiovascular Studies, Clinical and Research Applications of Engineering Principles, University Park Press, Baltimore*, pages 151–213, 1979.

D. Bers. *Excitation-Contraction Coupling and Cardiac Contractile Force*. Springer, 2nd ed. edition, August 2001. ISBN 0792371585.

D. M. Bers. Calcium fluxes involved in control of cardiac myocyte contraction. *Circulation Research*, 87(4):275–281, August 2000.

D. M. Bers. Cardiac excitation-contraction coupling. *Nature*, 415(6868):198–205, January 2002.

E. Blanchard, C. Seidman, J. G. Seidman, M. LeWinter, and D. Maughan. Altered cross-bridge kinetics in the αMHC403/+ mouse model of familial hypertrophic cardiomyopathy. *Circulation Research*, 84(4):475–483, March 1999.

W. F. Bluhm, M. Meyer, M. Sayen, E. A. Swanson, and W. H. Dillmann. Overexpression of sarcoplasmic reticulum Ca^{2+}-ATPase improves cardiac contractile function in hypothyroid mice. *Cardiovascular Research*, 43(2):382 –388, 1999.

W. F. Bluhm, E. G. Kranias, W. H. Dillmann, and M. Meyer. Phospholamban: a major determinant of the cardiac force-frequency relationship. *American Journal of Physiology - Heart and Circulatory Physiology*, 278(1):H249 –H255, January 2000.

V. E. Bondarenko, G. P. Szigeti, G. C. L. Bett, S.-J. Kim, and R. L. Rasmusson. Computer model of action potential of mouse ventricular myocytes. *American Journal of Physiology - Heart and Circulatory Physiology*, 287(3):H1378–1403, September 2004.

J. Bonet and R. D. Wood. *Nonlinear Continuum Mechanics for Finite Element Analysis*. Cambridge University Press, 2 edition, March 2008. ISBN 0521838703.

C. Bradley, A. Pullan, and P. Hunter. Geometric modeling of the human torso using cubic hermite elements. *Annals of Biomedical Engineering*, 25(1):96–111, January 1997.

P. Broemser and O. F. Ranke. *Ueber die Messung des Schlagvolumens des Herzens auf unblutigem Weg*. Lehmann, 1930.

A. Bueno-Orovio, E. M. Cherry, and F. H. Fenton. Minimal model for human ventricular action potentials in tissue. *Journal of Theoretical Biology*, 253(3):544–560, August 2008.

K. B. Campbell, M. V. Razumova, R. D. Kirkpatrick, and B. K. Slinker. Nonlinear myofilament regulatory processes affect frequency-dependent muscle fiber stiffness. *Biophysical Journal*, 81(4):2278–2296, October 2001.

K. Campbell. Impact of myocyte strain on cardiac myofilament activation. *Pflugers Archiv European Journal of Physiology*, 462(1):3–14, 2011.

S. G. Campbell, E. Howard, J. Aguado-Sierra, B. A. Coppola, J. H. Omens, L. J. Mulligan, A. D. McCulloch, and R. C. P. Kerckhoffs. Effect of transmurally heterogeneous myocyte excitation-contraction coupling on canine left ventricular electromechanics. *Experimental Physiology*, 94(5):541–552, December 2008a.

S. G. Campbell, S. N. Flaim, C. H. Leem, and A. D. McCulloch. Mechanisms of transmurally varying myocyte electromechanics in an integrated computational model. *Philosophical Transactions. Series A, Mathematical, Physical, and Engineering Sciences*, 366 (1879):3361–3380, September 2008b.

S. G. Campbell, P. C. Hatfield, and K. S. Campbell. A mathematical model of muscle containing heterogeneous half-sarcomeres exhibits residual force enhancement. *PLoS Computational Biology*, 7(9):e1002156, September 2011.

O. Cazorla, Y. Wu, T. C. Irving, and H. Granzier. Titin-based modulation of calcium sensitivity of active tension in mouse skinned cardiac myocytes. *Circulation Research*, 88(10):1028–1035, May 2001.

R. Chabiniok, P. Moireau, P.-F. Lesault, A. Rahmouni, J.-F. Deux, and D. Chapelle. Estimation of tissue contractility from cardiac cine-MRI using a biomechanical heart model. *Biomechanics and Modeling in Mechanobiology*, 11(5):609–630, May 2012.

R. H. Clayton and A. V. Panfilov. A guide to modelling cardiac electrical activity in anatomically detailed ventricles. *Progress in Biophysics and Molecular Biology*, 96(1-3): 19–43, 2008.

R. Clayton, O. Bernus, E. Cherry, H. Dierckx, F. Fenton, L. Mirabella, A. Panfilov, F. Sachse, G. Seemann, and H. Zhang. Models of cardiac tissue electrophysiology: Progress, challenges and open questions. *Progress in Biophysics and Molecular Biology*, 104(1–3):22–48, January 2011.

P. Colli Franzone, L. F. Pavarino, and B. Taccardi. Simulating patterns of excitation, repolarization and action potential duration with cardiac bidomain and monodomain models. *Mathematical Biosciences*, 197(1):35–66, 2005.

K. D. Costa, J. W. Holmes, and A. D. McCulloch. Modelling cardiac mechanical properties in three dimensions. *Philosophical Transactions of the Royal Society A: Mathematical, Physical and Engineering Sciences*, 359(1783):1233–1250, 2001.

M. Daniels, M. I. Noble, H. E. ter Keurs, and B. Wohlfart. Velocity of sarcomere shortening in rat cardiac muscle: relationship to force, sarcomere length, calcium and time. *The Journal of Physiology*, 355(1):367–381, October 1984.

J. P. Davis, C. Norman, T. Kobayashi, R. J. Solaro, D. R. Swartz, and S. B. Tikunova. Effects of thin and thick filament proteins on calcium binding and exchange with cardiac troponin C. *Biophysical Journal*, 92(9):3195–3206, May 2007.

T. A. Davis. Algorithm 832: UMFPACK v4.3—an unsymmetric-pattern multifrontal method. *ACM Transactions on Mathematical Software*, 30(2):196–199, 2004.

P. P. de Tombe and H. E. ter Keurs. An internal viscous element limits unloaded velocity of sarcomere shortening in rat myocardium. *The Journal of Physiology*, 454:619–642, August 1992.

P. P. de Tombe, R. D. Mateja, K. Tachampa, Y. Ait Mou, G. P. Farman, and T. C. Irving. Myofilament length dependent activation. *Journal of Molecular and Cellular Cardiology*, 48(5):851–858, May 2010.

H. Delingette, F. Billet, K. C. L. Wong, M. Sermesant, K. Rhode, M. Ginks, C. A. Rinaldi, R. Razavi, and N. Ayache. Personalization of cardiac motion and contractility from images using variational data assimilation. *IEEE Transactions on Biomedical Engineering*, 59(1):20–24, January 2012.

M. H. Dickinson, C. J. Hyatt, F. O. Lehmann, J. R. Moore, M. C. Reedy, A. Simcox, R. Tohtong, J. O. Vigoreaux, H. Yamashita, and D. W. Maughan. Phosphorylation-dependent power output of transgenic flies: an integrated study. *Biophysical Journal*, 73(6):3122–3134, December 1997.

D. DiFrancesco and D. Noble. A model of cardiac electrical activity incorporating ionic pumps and concentration changes. *Philosophical Transactions of the Royal Society of London. Series B, Biological Sciences*, 307(1133):353–398, 1985.

K. W. Dilly, C. F. Rossow, V. S. Votaw, J. S. Meabon, J. L. Cabarrus, and L. F. Santana. Mechanisms underlying variations in excitation–contraction coupling across the mouse left ventricular free wall. *The Journal of Physiology*, 572(1):227–241, January 2006.

D. P. Dobesh, J. P. Konhilas, and P. P. de Tombe. Cooperative activation in cardiac muscle: impact of sarcomere length. *American Journal of Physiology - Heart and Circulatory Physiology*, 282(3):H1055 –H1062, March 2002.

Y. Doi, G. Watanabe, K. Kotoh, K. Ueyama, and T. Misaki. Myocardial ischemic preconditioning during minimally invasive direct coronary artery bypass grafting attenuates ischemia-induced electrophysiological changes in human ventricle. *The Japanese Journal of Thoracic and Cardiovascular Surgery*, 51(4):144–150, April 2003.

H. C. Elman, D. J. Silvester, and A. J. Wathen. *Finite Elements and Fast Iterative Solvers: with Applications in Incompressible Fluid Dynamics*. Oxford University Press, USA, August 2005. ISBN 019852868X.

A. Eriksson. On improved predictions for structural equilibrium path evaluations. *International Journal for Numerical Methods in Engineering*, 36(2):201–220, January 1993.

A. Evangelista, P. Nardinocchi, P. E. Puddu, L. Teresi, C. Torromeo, and V. Varano. Torsion of the human left ventricle: Experimental analysis and computational modeling. *Progress in Biophysics and Molecular Biology*, 107(1):112–121, 2011.

G. P. Farman, D. Gore, E. Allen, K. Schoenfelt, T. C. Irving, and P. P. de Tombe. Myosin head orientation: a structural determinant for the Frank-Starling relationship. *American Journal of Physiology - Heart and Circulatory Physiology*, 300(6):H2155 –H2160, June 2011.

G. Farman, E. Allen, K. Schoenfelt, P. Backx, and P. de Tombe. The role of thin filament cooperativity in cardiac length-dependent calcium activation. *Biophysical Journal*, 99 (9):2978–2986, 2010.

F. Fenton and A. Karma. Vortex dynamics in three-dimensional continuous myocardium with fiber rotation: filament instability and fibrillation. *Chaos: An Interdisciplinary Journal of Nonlinear Science*, 8:20, 1998.

T. C. Foster, R. A. DeFazio, and J. L. Bizon. Characterizing cognitive aging of spatial and contextual memory in animal models. *Frontiers in Aging Neuroscience*, 4:12, 2012.

O. Frank. Die grundform des arteriellen pulses: Mathematische analyse. *Zeitschrift für Biologie*, 37, 1899.

O. Frank. Zur dynamik des herzmuskels. *Zeitschrift für Biologie*, 32:370–447, 1895.

W. H. Frishman and E. Saunders. β-adrenergic blockers. *The Journal of Clinical Hypertension*, 13(9):649–653, 2011.

N. Fukuda and H. L. Granzier. Titin/connectin-based modulation of the Frank-Starling mechanism of the heart. *Journal of Muscle Research and Cell Motility*, 26(6-8):319–323, February 2006.

N. Fukuda, T. Terui, I. Ohtsuki, S. Ishiwata, and S. Kurihara. Titin and troponin: Central players in the Frank-Starling mechanism of the heart. *Current Cardiology Reviews*, 5 (2):119–124, May 2009.

Y. C. Fung. *Biomechanics: Mechanical Properties of Living Tissues*. Springer, 2nd ed. edition, June 1993. ISBN 0387979476.

M. A. Geeves and K. C. Holmes. The molecular mechanism of muscle contraction. In J. M. Squire and D. A. D. Parry, editors, *Advances in Protein Chemistry*, volume Volume 71, pages 161–193. Academic Press, 2005. ISBN 0065-3233.

S. H. Gilbert, D. Benoist, A. P. Benson, E. White, S. F. Tanner, A. V. Holden, H. Dobrzynski, O. Bernus, and A. Radjenovic. Visualization and quantification of whole rat heart laminar structure using high-spatial resolution contrast-enhanced MRI. *American Journal of Physiology - Heart and Circulatory Physiology*, 302(1):H287–H298, January 2012.

T. E. Gillis, C. R. Marshall, X.-H. Xue, T. J. Borgford, and G. F. Tibbits. Ca^{2+} binding to cardiac troponin C: effects of temperature and pH on mammalian and salmonid isoforms. *American Journal of Physiology - Regulatory, Integrative and Comparative Physiology*, 279(5):R1707 –R1715, November 2000.

S. Göktepe and E. Kuhl. Computational modeling of cardiac electrophysiology: A novel finite element approach. *International Journal for Numerical Methods in Engineering*, 79(2):156–178, July 2009.

S. Göktepe and E. Kuhl. Electromechanics of the heart: a unified approach to the strongly coupled excitation–contraction problem. *Computational Mechanics*, 45(2):227–243, January 2010.

A. M. Gordon, A. F. Huxley, and F. J. Julian. The variation in isometric tension with sarcomere length in vertebrate muscle fibres. *The Journal of Physiology*, 184(1):170–192, May 1966.

E. Grandi, F. S. Pasqualini, and D. M. Bers. A novel computational model of the human ventricular action potential and Ca transient. *Journal of Molecular and Cellular Cardiology*, 48(1):112–121, January 2010.

J. F. Green. Mechanism of action of isoproterenol on venous return. *The American Journal of Physiology*, 232(2):H152–156, February 1977.

J. M. Guccione, A. D. McCulloch, and L. K. Waldman. Passive material properties of intact ventricular myocardium determined from a cylindrical model. *Journal of Biomechanical Engineering*, 113(1):42–55, February 1991.

J. Gulati, E. Sonnenblick, and A. Babu. The role of troponin C in the length dependence of Ca^{2+}-sensitive force of mammalian skeletal and cardiac muscles. *The Journal of Physiology*, 441:305–324, September 1991.

V. Gurev, T. Lee, J. Constantino, H. Arevalo, and N. A. Trayanova. Models of cardiac electromechanics based on individual hearts imaging data: image-based electromechanical models of the heart. *Biomechanics and Modeling in Mechanobiology*, 10(3):295–306, June 2011.

J. K. Gwathmey and R. J. Hajjar. Effect of protein kinase c activation on sarcoplasmic reticulum function and apparent myofibrillar Ca^{2+} sensitivity in intact and skinned muscles from normal and diseased human myocardium. *Circulation Research*, 67(3): 744–752, September 1990.

L. M. Hanft, F. S. Korte, and K. S. McDonald. Cardiac function and modulation of sarcomeric function by length. *Cardiovascular Research*, 77(4):627 –636, March 2008.

L. J. Healy, Y. Jiang, and E. W. Hsu. Quantitative comparison of myocardial fiber structure between mice, rabbit, and sheep using diffusion tensor cardiovascular magnetic resonance. *Journal of Cardiovascular Magnetic Resonance*, 13(1):74, 2011.

V. Herold, P. Mörchel, C. Faber, E. Rommel, A. Haase, and P. M. Jakob. In vivo quantitative three-dimensional motion mapping of the murine myocardium with PC-MRI at 17.6 T. *Magnetic Resonance in Medicine*, 55(5):1058–1064, May 2006.

A. V. Hill. The heat of shortening and the dynamic constants of muscle. *Proceedings of the Royal Society of London. Series B - Biological Sciences*, 126(843):136 –195, October 1938.

A. L. Hodgkin and A. F. Huxley. A quantitative description of membrane current and its application to conduction and excitation in nerve. *Journal of Physiology*, 117:500–544, 1952.

G. A. Holzapfel and R. W. Ogden. Constitutive modelling of passive myocardium: a structurally based framework for material characterization. *Philosophical Transactions of the Royal Society of London. Series A, Mathematical and Physical Sciences*, 367 (1902):3445, 2009.

D. A. Hooks, K. A. Tomlinson, S. G. Marsden, I. J. LeGrice, B. H. Smaill, A. J. Pullan, and P. J. Hunter. Cardiac microstructure: Implications for electrical propagation and defibrillation in the heart. *Circulation Research*, 91(4):331–338, August 2002.

P. J. Hunter, A. D. McCulloch, and H. Ter Keurs. Modelling the mechanical properties of cardiac muscle. *Progress in Biophysics and Molecular Biology*, 69(2-3):289–331, 1998.

A. F. Huxley. Mechanics and models of the myosin motor. *Philosophical Transactions of the Royal Society of London. Series B: Biological Sciences*, 355(1396):433–440, April 2000.

A. F. Huxley. Muscle structure and theories of contraction. *Progress in Biophysics and Biophysical Chemistry*, 7:255–318, 1957.

V. Iyer, R. Mazhari, and R. L. Winslow. A computational model of the human left-ventricular epicardial myocyte. *Biophysical Journal*, 87(3):1507–1525, 2004.

P. Janssen. Myocardial contraction-relaxation coupling. *American Journal of Physiology - Heart and Circulatory Physiology*, 299(6):H1741–H1749, 2010.

Y. Jiang, K. Pandya, O. Smithies, and E. Hsu. Three-dimensional diffusion tensor microscopy of fixed mouse hearts. *Magnetic Resonance in Medicine*, 52(3):453–460, 2004.

S. Joho, S. Ishizaka, R. Sievers, E. Foster, P. Simpson, and W. Grossman. Left ventricular pressure-volume relationship in conscious mice. *American Journal of Physiology - Heart and Circulatory Physiology*, 292(1):H369–H377, 2007.

A. M. Katz. *Physiology of the Heart*. Lippincott Williams and Wilkins, 4th revised edition edition, November 2005. ISBN 0781755018.

M. Kawai, Y. Saeki, and Y. Zhao. Crossbridge scheme and the kinetic constants of elementary steps deduced from chemically skinned papillary and trabecular muscles of the ferret. *Circulation Research*, 73(1):35–50, July 1993.

M. Kawai and P. W. Brandt. Sinusoidal analysis: a high resolution method for correlating biochemical reactions with physiological processes in activated skeletal muscles of rabbit, frog and crayfish. *Journal of Muscle Research and Cell Motility*, 1(3):279–303, September 1980.

J. Keener and J. Sneyd. *Mathematical Physiology*. Springer, 1998. ISBN 0387983813.

R. H. Keldermann, M. P. Nash, H. Gelderblom, V. Y. Wang, and A. V. Panfilov. Electromechanical wavebreak in a model of the human left ventricle. *American Journal of Physiology - Heart and Circulatory Physiology*, April 2010.

R. C. P. Kerckhoffs, P. H. M. Bovendeerd, J. C. S. Kotte, F. W. Prinzen, K. Smits, and T. Arts. Homogeneity of cardiac contraction despite physiological asynchrony of depolarization: A model study. *Annals of Biomedical Engineering*, 31(5):536–547, May 2003a.

R. C. P. Kerckhoffs, P. H. M. Bovendeerd, F. W. Prinzen, K. Smits, and T. Arts. Intra- and interventricular asynchrony of electromechanics in the ventricularly paced heart. *Journal of Engineering Mathematics*, 47(3/4):201–216, December 2003b.

R. C. P. Kerckhoffs, O. P. Faris, P. H. M. Bovendeerd, F. W. Prinzen, K. Smits, E. R. McVeigh, and T. Arts. Electromechanics of paced left ventricle simulated by straightforward mathematical model: comparison with experiments. *American Journal of Physiology - Heart and Circulatory Physiology*, 289(5):H1889, 2005.

R. C. P. Kerckhoffs, S. N. Healy, T. P. Usyk, and A. D. McCulloch. Computational methods for cardiac electromechanics. *Proceedings of the IEEE*, 94(4):769–783, 2006.

R. C. P. Kerckhoffs, O. P. Faris, P. H. M. Bovendeerd, F. W. Prinzen, K. Smits, E. R. McVeigh, and T. Arts. Timing of depolarization and contraction in the paced canine left ventricle:. model and experiment. *Journal of Cardiovascular Electrophysiology*, 14 (s10):S188–S195, October 2003c.

R. C. P. Kerckhoffs, A. D. McCulloch, J. H. Omens, and L. J. Mulligan. Effects of biventricular pacing and scar size in a computational model of the failing heart with left bundle branch block. *Medical Image Analysis*, 13(2):362–369, April 2009.

R. C. P. Kerckhoffs, J. H. Omens, A. D. McCulloch, and L. J. Mulligan. Ventricular dilation and electrical dyssynchrony synergistically increase regional mechanical nonuniformity but not mechanical dyssynchrony: A computational model. *Circulation Heart Failure*, 3(4):528–536, July 2010.

D. A. Knoll and D. E. Keyes. Jacobian-free newton-krylov methods: a survey of approaches and applications. *Journal of Computational Physics*, 193(2):357–397, January 2004.

P. Kohl and F. Sachs. Mechanoelectric feedback in cardiac cells. *Philosophical Transactions of the Royal Society A: Mathematical, Physical and Engineering Sciences*, 359(1783): 1173–1185, 2001.

J. P. Konhilas, T. C. Irving, and P. P. de Tombe. Myofilament calcium sensitivity in skinned rat cardiac trabeculae: Role of interfilament spacing. *Circulation Research*, 90 (1):59–65, January 2002.

E. G. Kranias and D. M. Bers. Calcium and cardiomyopathies. *Sub-Cellular Biochemistry*, 45:523–537, 2007.

K. Kreutziger, N. Piroddi, J. McMichael, C. Tesi, C. Poggesi, and M. Regnier. Calcium binding kinetics of troponin C strongly modulate cooperative activation and tension kinetics in cardiac muscle. *Journal of Molecular and Cellular Cardiology*, 50(1):165–174, 2011.

P. Lafortune, R. Arís, M. Vázquez, and G. Houzeaux. Coupled electromechanical model of the heart: Parallel finite element formulation. *International Journal for Numerical Methods in Biomedical Engineering*, 28(1):72–86, 2012.

P. Lamata, S. Niederer, D. Barber, D. Norsletten, J. Lee, R. Hose, and N. Smith. Personalization of cubic hermite meshes for efficient biomechanical simulations. *MICCAI: International Conference on Medical Image Computing and Computer-Assisted Intervention*, 13(Pt 2):380–387, 2010.

P. Lamata, S. Niederer, D. Nordsletten, D. C. Barber, I. Roy, D. R. Hose, and N. Smith. An accurate, fast and robust method to generate patient-specific cubic hermite meshes. *Medical Image Analysis*, 15(6):801–813, December 2011.

P. Lamata, I. Roy, B. Blazevic, A. Crozier, S. Land, S. A. Niederer, D. R. Hose, and N. P. Smith. Quality metrics for high order meshes: analysis of the mechanical simulation of the heart beat. *IEEE Transactions on Medical Imaging*, 32(1):130–138, January 2013.

S. Land, S. A. Niederer, and N. P. Smith. Efficient computational methods for strongly coupled cardiac electromechanics. *IEEE Transactions on Biomedical Engineering*, 59 (5):1219 –1228, May 2012a.

S. Land, S. A. Niederer, J. M. Aronsen, E. K. S. Espe, L. Zhang, W. E. Louch, I. Sjaastad, O. M. Sejersted, and N. P. Smith. An analysis of deformation-dependent electromechanical coupling in the mouse heart. *The Journal of Physiology*, 590(18):4553–4569, September 2012b.

S. Land, W. E. Louch, S. A. Niederer, J. M. Aronsen, G. Christensen, I. Sjaastad, O. M. Sejersted, and N. P. Smith. Beta-adrenergic stimulation maintains cardiac function in Serca2 knockout mice. *Biophysical Journal*, 2013.

E. J. Lee, J. Peng, M. Radke, M. Gotthardt, and H. L. Granzier. Calcium sensitivity and the Frank-Starling mechanism of the heart are increased in titin N2B region-deficient mice. *Journal of Molecular and Cellular Cardiology*, 49(3):449–458, 2010.

I. J. LeGrice, B. H. Smaill, L. Z. Chai, S. G. Edgar, J. B. Gavin, and P. J. Hunter. Laminar structure of the heart: ventricular myocyte arrangement and connective tissue architecture in the dog. *The American Journal of Physiology*, 269(2 Pt 2):H571–582, August 1995.

I. J. Legrice, P. J. Hunter, and B. H. Smaill. Laminar structure of the heart: a mathematical model. *American Journal of Physiology - Heart and Circulatory Physiology*, 272(5): H2466–2476, May 1997.

C. Levy and A. Landesberg. Cross-bridge dependent cooperativity determines the cardiac force-length relationship. *Journal of Molecular and Cellular Cardiology*, 40(5):639–647, May 2006.

L. Li, S. A. Niederer, W. Idigo, Y. H. Zhang, P. Swietach, B. Casadei, and N. P. Smith. A mathematical model of the murine ventricular myocyte: a data-driven biophysically based approach applied to mice overexpressing the canine NCX isoform. *American Journal of Physiology - Heart and Circulatory Physiology*, 299(4):H1045–1063, October 2010.

L. Li, W. E. Louch, S. A. Niederer, K. B. Andersson, G. Christensen, O. M. Sejersted, and N. P. Smith. Calcium dynamics in the ventricular myocytes of SERCA2 knockout mice: A modeling study. *Biophysical Journal*, 100(2):322–331, 2011.

L. Li, W. E. Louch, S. A. Niederer, J. M. Aronsen, G. Christensen, O. M. Sejersted, and N. P. Smith. Sodium accumulation in SERCA knockout-induced heart failure. *Biophysical Journal*, 102(9):2039–2048, May 2012.

S. Linge, J. Sundnes, M. Hanslien, G. Lines, and A. Tveito. Numerical solution of the bidomain equations. *Philosophical Transactions of the Royal Society A: Mathematical, Physical and Engineering Sciences*, 367(1895):1931–1950, May 2009.

S. Linge, G. Lines, and J. Sundnes. Solving the heart mechanics equations with Newton and quasi Newton methods - a comparison. *Computer Methods in Biomechanics and Biomedical Engineering*, 8(1):31–38, February 2005.

S. C. Little, B. J. Biesiadecki, A. Kilic, R. S. D. Higgins, P. M. L. Janssen, and J. P. Davis. The rates of Ca^{2+} dissociation and cross-bridge detachment from ventricular myofibrils as reported by a fluorescent cardiac troponin C. *Journal of Biological Chemistry*, 287 (33):27930–27940, October 2012.

T. D. Littlewood, D. C. Hancock, P. S. Danielian, M. G. Parker, and G. I. Evan. A modified oestrogen receptor ligand-binding domain as an improved switch for the regulation of heterologous proteins. *Nucleic Acids Research*, 23(10):1686 –1690, May 1995.

W. E. Louch, K. Hougen, H. K. Mørk, F. Swift, J. M. Aronsen, I. Sjaastad, H. M. Reims, B. Roald, K. B. Andersson, G. Christensen, and O. M. Sejersted. Sodium accumulation promotes diastolic dysfunction in end-stage heart failure following Serca2 knockout. *The Journal of Physiology*, 588(3):465–478, January 2010.

C. H. Luo and Y. Rudy. A dynamic model of the cardiac ventricular action potential. I. simulations of ionic currents and concentration changes. *Circulation Research*, 74(6): 1071, 1994a.

C. H. Luo and Y. Rudy. A dynamic model of the cardiac ventricular action potential. II. afterdepolarizations, triggered activity, and potentiation. *Circulation Research*, 74(6): 1097, 1994b.

C. H. Luo and Y. Rudy. A model of the ventricular cardiac action potential. depolarization, repolarization, and their interaction. *Circulation Research*, 68(6):1501, 1991.

V. A. Maltsev and E. G. Lakatta. Yin and yang of the cardiac pacemaker clock system in health and disease. *Heart Rhythm*, 7(1):96–98, January 2010.

L. Marcucci and T. Yanagida. From single molecule fluctuations to muscle contraction: A Brownian model of A.F. Huxley's hypotheses. *PLoS ONE*, 7(7):e40042, July 2012.

R. L. Mayden, K. L. Tang, K. W. Conway, J. Freyhof, S. Chamberlain, M. Haskins, L. Schneider, M. Sudkamp, R. M. Wood, M. Agnew, A. Bufalino, Z. Sulaiman, M. Miya, K. Saitoh, and S. He. Phylogenetic relationships of Danio within the order Cypriniformes: a framework for comparative and evolutionary studies of a model species. *Journal of Experimental Zoology Part B: Molecular and Developmental Evolution*, 308B(5): 642–654, 2007.

K. S. McDonald and R. L. Moss. Osmotic compression of single cardiac myocytes eliminates the reduction in Ca^{2+} sensitivity of tension at short sarcomere length. *Circulation Research*, 77(1):199–205, July 1995.

K. S. McDowell, F. Vadakkumpadan, R. Blake, J. Blauer, G. Plank, R. S. MacLeod, and N. A. Trayanova. Methodology for patient-specific modeling of atrial fibrosis as a substrate for atrial fibrillation. *Journal of Electrocardiology*, 45(6):640–645, December 2012.

D. F. McKillop and M. A. Geeves. Regulation of the interaction between actin and myosin subfragment 1: evidence for three states of the thin filament. *Biophysical Journal*, 65 (2):693–701, 1993.

J. M. Metzger and M. V. Westfall. Covalent and noncovalent modification of thin filament action the essential role of troponin in cardiac muscle regulation. *Circulation Research*, 94(2):146–158, June 2004.

R. W. Mills, S. M. Narayan, and A. D. McCulloch. Mechanisms of conduction slowing during myocardial stretch by ventricular volume loading in the rabbit. *American Journal of Physiology - Heart and Circulatory Physiology*, 295(3):H1270–1278, September 2008.

G. R. Mirams, Y. Cui, A. Sher, M. Fink, J. Cooper, B. M. Heath, N. C. McMahon, D. J. Gavaghan, and D. Noble. Simulation of multiple ion channel block provides improved early prediction of compounds' clinical torsadogenic risk. *Cardiovascular Research*, 91 (1):53–61, July 2011.

R. L. Moss, L. O. Nwoye, and M. L. Greaser. Substitution of cardiac troponin C into rabbit muscle does not alter the length dependence of Ca^{2+} sensitivity of tension. *The Journal of Physiology*, 440(1):273–289, January 1991.

R. L. Moss and D. P. Fitzsimons. Frank-starling relationship: Long on importance, short on mechanism. *Circulation Research*, 90(1):11–13, January 2002.

L. A. Mulieri, G. Hasenfuss, B. Leavitt, P. D. Allen, and N. R. Alpert. Altered myocardial force-frequency relation in human heart failure. *Circulation*, 85(5):1743, 1992.

L. J. Mullins and J. J. Mullins. Transgenesis in the rat and larger mammals. *Journal of Clinical Investigation*, 97(7):1557, 1996.

M. P. Nash and P. J. Hunter. Computational mechanics of the heart. *Journal of Elasticity*, 61(1):113–141, 2000.

M. P. Nash and A. V. Panfilov. Electromechanical model of excitable tissue to study reentrant cardiac arrhythmias. *Progress in Biophysics and Molecular Biology*, 85(2-3): 501–522, 2004.

J. Nerbonne. Studying cardiac arrhythmias in the Mouse—A reasonable model for probing mechanisms? *Trends in Cardiovascular Medicine*, 14(3):83–93, April 2004.

D. Nickerson, N. Smith, and P. Hunter. New developments in a strongly coupled cardiac electromechanical model. *Europace*, 7(s2):S118, 2005.

D. P. Nickerson. *Cardiac Electro-Mechanics: From cellML to the Whole Heart*. PhD thesis, The University of Auckland, March 2005.

S. A. Niederer and N. P. Smith. An improved numerical method for strong coupling of excitation and contraction models in the heart. *Progress in Biophysics and Molecular Biology*, 96(1-3):90–111, 2008.

S. A. Niederer, P. J. Hunter, and N. P. Smith. A quantitative analysis of cardiac myocyte relaxation: a simulation study. *Biophysical Journal*, 90(5):1697–1722, 2006.

S. A. Niederer, M. Fink, D. Noble, and N. P. Smith. A meta-analysis of cardiac electrophysiology computational models. *Experimental Physiology*, 94(5):486–495, 2009a.

S. A. Niederer, H. E. D. J. Ter Keurs, and N. P. Smith. Modelling and measuring electromechanical coupling in the rat heart. *Experimental Physiology*, 94(5):529–540, 2009b.

S. A. Niederer, G. Plank, P. Chinchapatnam, M. Ginks, P. Lamata, K. S. Rhode, C. A. Rinaldi, R. Razavi, and N. P. Smith. Length-dependent tension in the failing heart and the efficacy of cardiac resynchronization therapy. *Cardiovascular Research*, 89(2):336, 2011a.

S. Niederer and N. Smith. The role of the Frank-Starling law in the transduction of cellular work to whole organ pump function: A computational modeling analysis. *PLoS Computational Biology*, 5(4), 2009.

S. Niederer, P. Lamata, G. Plank, P. Chinchapatnam, M. Ginks, K. Rhode, C. Rinaldi, R. Razavi, and N. Smith. Analyses of the redistribution of work following cardiac resynchronisation therapy in a patient specific model. *PLoS ONE*, 7(8), 2012a.

S. A. Niederer, E. Kerfoot, A. P. Benson, M. O. Bernabeu, O. Bernus, C. Bradley, E. M. Cherry, R. Clayton, F. H. Fenton, A. Garny, E. Heidenreich, S. Land, M. Maleckar, P. Pathmanathan, G. Plank, J. F. Rodríguez, I. Roy, F. B. Sachse, G. Seemann, O. Skavhaug, N. P. Smith, S. A. Niederer, E. Kerfoot, A. P. Benson, M. O. Bernabeu, O. Bernus, C. Bradley, E. M. Cherry, R. Clayton, F. H. Fenton, A. Garny, E. Heidenreich, S. Land, M. Maleckar, P. Pathmanathan, G. Plank, J. F. Rodríguez, I. Roy, F. B. Sachse, G. Seemann, O. Skavhaug, and N. P. Smith. Verification of cardiac tissue electrophysiology simulators using an N-version benchmark. *Philosophical Transactions of the Royal Society A: Mathematical, Physical and Engineering Sciences*, 369(1954): 4331–4351, November 2011b.

S. A. Niederer, A. K. Shetty, G. Plank, J. Bostock, R. Razavi, N. P. Smith, and C. A. Rinaldi. Biophysical modeling to simulate the response to multisite left ventricular stimulation using a quadripolar pacing lead. *Pacing and Clinical Electrophysiology: PACE*, 35(2):204–214, February 2012b.

P. M. Nielsen, I. J. Le Grice, B. H. Smaill, and P. J. Hunter. Mathematical model of geometry and fibrous structure of the heart. *American Journal of Physiology - Heart and Circulatory Physiology*, 260(4):H1365 –H1378, April 1991.

K. C. Nishikawa, J. A. Monroy, T. E. Uyeno, S. H. Yeo, D. K. Pai, and S. L. Lindstedt. Is titin a 'winding filament'? A new twist on muscle contraction. *Philosophical Transactions of the Royal Society B: Biological Sciences*, 279(1730):981–990, March 2012.

F. Nobile, A. Quarteroni, and R. Ruiz-Baier. An active strain electromechanical model for cardiac tissue. *International Journal for Numerical Methods in Biomedical Engineering*, 28(1):52–71, 2012.

D. Noble. A modification of the Hodgkin-Huxley equations applicable to Purkinje fibre action and pacemaker potentials. *The Journal of Physiology*, 160(2):317–352, February 1962.

D. Noble and Y. Rudy. Models of cardiac ventricular action potentials: iterative interaction between experiment and simulation. *Philosophical Transactions of the Royal Society of London. Series A: Mathematical, Physical and Engineering Sciences*, 359(1783):1127 –1142, June 2001.

D. Noble, S. J. Noble, G. C. L. Bett, Y. E. Earm, W. K. Ho, and I. K. So. The role of sodium-calcium exchange during the cardiac action potential. *Annals of the New York Academy of Sciences*, 639:334–353, 1991.

D. Noble, A. Varghese, P. Kohl, and P. Noble. Improved guinea-pig ventricular cell model incorporating a diadic space, I_{Kr} and I_{Ks}, and length-and tension-dependent processes. *The Canadian Journal of Cardiology*, 14(1):123, 1998.

D. Noble, A. Garny, and P. J. Noble. How the Hodgkin–Huxley equations inspired the cardiac physiome project. *The Journal of Physiology*, 590(11):2613–2628, January 2012.

D. Nordsletten, S. Niederer, M. Nash, P. Hunter, and N. Smith. Coupling multi-physics models to cardiac mechanics. *Progress in Biophysics and Molecular Biology*, 104(1–3): 77–88, January 2011.

T. O'Hara, L. Virág, A. Varró, and Y. Rudy. Simulation of the undiseased human cardiac ventricular action potential: Model formulation and experimental validation. *PLoS Computational Biology*, 7(5):e1002061, May 2011.

J. H. Omens, H. A. Rockman, and J. W. Covell. Passive ventricular mechanics in tight-skin mice. *American Journal of Physiology - Heart and Circulatory Physiology*, 266(3): H1169 –H1176, March 1994.

L. H. Opie. *Heart Physiology: From Cell to Circulation*. Lippincott Williams and Wilkins, 4th revised edition edition, December 2003. ISBN 0781742781.

C. A. Opitz, M. Kulke, M. C. Leake, C. Neagoe, H. Hinssen, R. J. Hajjar, and W. A. Linke. Damped elastic recoil of the titin spring in myofibrils of human myocardium. *Proceedings of the National Academy of Sciences of the United States of America*, 100 (22):12688–12693, 2003.

P. Pacher, T. Nagayama, P. Mukhopadhyay, S. Batkai, and D. A. Kass. Measurement of cardiac function using pressure-volume conductance catheter technique in mice and rats. *Nature Protocols*, 3(9):1422–1434, 2008.

B. M. Palmer. A strain-dependency of myosin off-rate must be sensitive to frequency to predict the b-process of sinusoidal analysis. *Muscle Biophysics*, pages 57–75, 2010.

B. M. Palmer, D. E. Fishbaugher, J. P. Schmitt, Y. Wang, N. R. Alpert, C. E. Seidman, J. G. Seidman, P. VanBuren, and D. W. Maughan. Differential cross-bridge kinetics of FHC myosin mutations R403Q and R453C in heterozygous mouse myocardium. *American Journal of Physiology - Heart and Circulatory Physiology*, 287(1):H91 –H99, July 2004a.

B. M. Palmer, D. Georgakopoulos, P. M. Janssen, Y. Wang, N. R. Alpert, D. F. Belardi, S. P. Harris, R. L. Moss, P. G. Burgon, C. E. Seidman, J. G. Seidman, D. W. Maughan, and D. A. Kass. Role of cardiac myosin binding protein c in sustaining left ventricular systolic stiffening. *Circulation Research*, 94(9):1249–1255, May 2004b.

B. M. Palmer, T. Suzuki, Y. Wang, W. D. Barnes, M. S. Miller, and D. W. Maughan. Two-state model of acto-myosin attachment-detachment predicts c-process of sinusoidal analysis. *Biophysical Journal*, 93(3):760–769, August 2007.

A. V. Panfilov. Is heart size a factor in ventricular fibrillation? or how close are rabbit and human hearts? *Heart Rhythm*, 3(7):862–864, 2006.

J. Patel, J. Pleitner, R. Moss, and M. Greaser. Magnitude of length-dependent changes in contractile properties varies with titin isoform in rat ventricles. *American Journal of Physiology - Heart and Circulatory Physiology*, 302(3):H697–H708, 2012.

P. Pathmanathan, S. J. Chapman, D. J. Gavaghan, and J. P. Whiteley. Cardiac electromechanics: the effect of contraction model on the mathematical problem and accuracy of the numerical scheme. *The Quarterly Journal of Mechanics and Applied Mathematics*, 63(3):375–399, 2010.

P. Pathmanathan, M. O. Bernabeu, S. A. Niederer, D. J. Gavaghan, and D. Kay. Computational modelling of cardiac electrophysiology: explanation of the variability of results from different numerical solvers. *International Journal for Numerical Methods in Biomedical Engineering*, 28(8):890–903, 2012.

P. Pathmanathan and J. Whiteley. A numerical method for cardiac mechanoelectric simulations. *Annals of Biomedical Engineering*, 37(5):860–873, May 2009.

M. Periasamy, T. D. Reed, L. H. Liu, Y. Ji, E. Loukianov, R. J. Paul, M. L. Nieman, T. Riddle, J. J. Duffy, T. Doetschman, J. N. Lorenz, and G. E. Shull. Impaired cardiac performance in heterozygous mice with a null mutation in the sarco(endo)plasmic reticulum Ca^{2+}-ATPase isoform 2 (SERCA2) gene. *Journal of Biological Chemistry*, 274(4): 2556–2562, January 1999.

D. Picard, S. D. E. Jeremy Thorner, and J. N. Abelson. Posttranslational regulation of proteins by fusions to steroid-binding domains. In *Applications of Chimeric Genes and Hybrid Proteins - Part B: Cell Biology and Physiology*, volume Volume 327, pages 385–401. Academic Press, 2000. ISBN 0076-6879.

B. Pieske, M. Sütterlin, S. Schmidt-Schweda, K. Minami, M. Meyer, M. Olschewski, C. Holubarsch, H. Just, and G. Hasenfuss. Diminished post-rest potentiation of contractile force in human dilated cardiomyopathy. functional evidence for alterations in intracellular Ca^{2+} handling. *Journal of Clinical Investigation*, 98(3):764–776, August 1996.

J. Pitt-Francis, P. Pathmanathan, M. O. Bernabeu, R. Bordas, J. Cooper, A. G. Fletcher, G. R. Mirams, P. Murray, J. M. Osborne, A. Walter, S. J. Chapman, A. Garny, I. M. van Leeuwen, P. K. Maini, B. Rodríguez, S. L. Waters, J. P. Whiteley, H. M. Byrne, and D. J. Gavaghan. Chaste: A test-driven approach to software development for biological modelling. *Computer Physics Communications*, 180(12):2452–2471, December 2009.

Z. Qu and A. Garfinkel. An advanced algorithm for solving partial differential equation in cardiac conduction. *IEEE Transactions on Biomedical Engineering*, 46(9):1166–1168, 1999.

V. S. Rao, E. N. Marongelli, and W. H. Guilford. Phosphorylation of tropomyosin extends cooperative binding of myosin beyond a single regulatory unit. *Cell Motility and the Cytoskeleton*, 66(1):10–23, 2009.

M. V. Razumova, A. E. Bukatina, and K. B. Campbell. Stiffness-distortion sarcomere model for muscle simulation. *Journal of Applied Physiology*, 87(5):1861–1876, November 1999.

J. J. Rice and P. P. de Tombe. Approaches to modeling crossbridges and calcium-dependent activation in cardiac muscle. *Progress in Biophysics and Molecular Biology*, 85(2-3):179–195, 2004.

J. J. Rice, F. Wang, D. M. Bers, and P. P. de Tombe. Approximate model of cooperative activation and crossbridge cycling in cardiac muscle using ordinary differential equations. *Biophysical Journal*, 95(5):2368–2390, 2008a.

J. J. Rice, Y. Tu, C. Poggesi, and P. P. de Tombe. Spatially-compressed cardiac myofilament models generate hysteresis that is not found in real muscle. *Pacific Symposium on Biocomputing.*, pages 366–377, 2008b.

B. J. Roth. Electrical conductivity values used with the bidomain model of cardiac tissue. *IEEE Transactions on Biomedical Engineering*, 44(4):326–328, April 1997.

S. Rush and H. Larsen. A practical algorithm for solving dynamic membrane equations. *IEEE Transactions on Biomedical Engineering*, BME-25(4):389–392, 1978.

F. B. Sachse, G. Seemann, and M. B. Mohr. Electro-mechanics in biventricular models. In *Computers in Cardiology*, volume 31, pages 537–540, 2004.

J. J. Saucerman and A. D. McCulloch. Cardiac β-adrenergic signaling. *Annals of the New York Academy of Sciences*, 1080(1):348–361, 2006.

B. Sauer and N. Henderson. Site-specific DNA recombination in mammalian cells by the Cre recombinase of bacteriophage P1. *Proceedings of the National Academy of Sciences*, 85(14):5166 –5170, July 1988.

H. Schmid, M. P. Nash, A. A. Young, and P. J. Hunter. Myocardial material parameter estimation - a comparative study for simple shear. *Journal of Biomechanical Engineering*, 128:742, 2006.

J. E. Schneider, F. Wiesmann, C. A. Lygate, and S. Neubauer. How to perform an accurate assessment of cardiac function in mice using high-resolution magnetic resonance imaging. *Journal of Cardiovascular Magnetic Resonance*, 8(5):693–701, 2006.

J. E. J. Schultz, B. J. Glascock, S. A. Witt, M. L. Nieman, K. J. Nattamai, L. H. Liu, J. N. Lorenz, G. E. Shull, T. R. Kimball, and M. Periasamy. Accelerated onset of heart failure in mice during pressure overload with chronically decreased SERCA2 calcium pump activity. *American Journal of Physiology - Heart and Circulatory Physiology*, 286 (3):H1146–H1153, January 2004.

C. J. Schwiening. A brief historical perspective: Hodgkin and Huxley. *The Journal of Physiology*, 590(11):2571–2575, 2012.

P. Segers, E. R. Rietzschel, M. L. De Buyzere, N. Stergiopulos, N. Westerhof, L. M. Van Bortel, T. Gillebert, and P. R. Verdonck. Three-and four-element windkessel models: assessment of their fitting performance in a large cohort of healthy middle-aged individuals. *Proceedings of the Institution of Mechanical Engineers, Part H: Journal of Engineering in Medicine*, 222(4):417–428, 2008.

P. Segers, D. Georgakopoulos, M. Afanasyeva, H. C. Champion, D. P. Judge, H. D. Millar, P. Verdonck, D. A. Kass, N. Stergiopulos, and N. Westerhof. Conductance catheter-based assessment of arterial input impedance, arterial function, and ventricular-vascular interaction in mice. *American Journal of Physiology - Heart and Circulatory Physiology*, 288(3):H1157 –H1164, March 2005.

M. Sermesant, H. Delingette, and N. Ayache. An electromechanical model of the heart for image analysis and simulation. *IEEE Transactions on Medical Imaging*, 25(5):612–625, 2006.

M. Sermesant, F. Billet, R. Chabiniok, T. Mansi, P. Chinchapatnam, P. Moireau, J.-M. Peyrat, K. Rhode, M. Ginks, P. Lambiase, S. Arridge, H. Delingette, M. Sorine, C. Rinaldi, D. Chapelle, R. Razavi, and N. Ayache. Personalised electromechanical

model of the heart for the prediction of the acute effects of cardiac resynchronisation therapy. In *Functional Imaging and Modeling of the Heart*, volume 5528, pages 239–248. Springer Berlin Heidelberg, 2009.

W. C. Skarnes, B. Rosen, A. P. West, M. Koutsourakis, W. Bushell, V. Iyer, A. O. Mujica, M. Thomas, J. Harrow, T. Cox, D. Jackson, J. Severin, P. Biggs, J. Fu, M. Nefedov, P. J. de Jong, A. F. Stewart, and A. Bradley. A conditional knockout resource for the genome-wide study of mouse gene function. *Nature*, 474(7351):337–342, June 2011.

L. Smith, C. Tainter, M. Regnier, and D. Martyn. Cooperative cross-bridge activation of thin filaments contributes to the Frank-Starling mechanism in cardiac muscle. *Biophysical Journal*, 96(9):3692–3702, May 2009.

N. P. Smith, M. L. Buist, and A. J. Pullan. Altered T wave dynamics in a contracting cardiac model. *Journal of Cardiovascular Electrophysiology*, 14(10):203, 2003.

N. P. Smith, D. P. Nickerson, E. J. Crampin, and P. J. Hunter. Multiscale computational modelling of the heart. *Acta Numerica*, 13:371–431, 2004.

D. S. Sohal, M. Nghiem, M. A. Crackower, S. A. Witt, T. R. Kimball, K. M. Tymitz, J. M. Penninger, and J. D. Molkentin. Temporally regulated and tissue-specific gene manipulations in the adult and embryonic heart using a tamoxifen-inducible cre protein. *Circulation Research*, 89(1):20–25, July 2001.

R. J. Solaro. Maintaining cooperation among cardiac myofilament proteins through thick and thin. *The Journal of Physiology*, 587(1):3, January 2009.

R. J. Solaro. Mechanisms of the Frank-Starling law of the heart: The beat goes on. *Biophysical Journal*, 93(12):4095–4096, December 2007.

R. J. Solaro. Sarcomere control mechanisms and the dynamics of the cardiac cycle. *Journal of Biomedicine and Biotechnology*, 2010:1–9, 2010.

M. S. Springer, R. W. Meredith, J. E. Janecka, and W. J. Murphy. The historical biogeography of mammalia. *Philosophical Transactions of the Royal Society B: Biological Sciences*, 366(1577):2478–2502, December 2011.

J. A. Spudich and S. Sivaramakrishnan. Myosin VI: an innovative motor that challenged the swinging lever arm hypothesis. *Nature Reviews. Molecular cell Biology*, 11(2):128–137, February 2010.

E. H. Starling. *The Linacre lecture on the law of the heart.* Longmans, Green, & co, London, 1918.

R. Stehle and B. Iorga. Kinetics of cardiac sarcomeric processes and rate-limiting steps in contraction and relaxation. *Journal of Molecular and Cellular Cardiology*, 48(5): 843–850, May 2010.

N. Stergiopulos, B. E. Westerhof, and N. Westerhof. Total arterial inertance as the fourth element of the windkessel model. *American Journal of Physiology - Heart and Circulatory Physiology*, 276(1):H81 –H88, January 1999.

G. Strang. On the construction and comparison of difference schemes. *SIAM Journal on Numerical Analysis*, 5(3):506–517, September 1968.

L. B. Stull, M. K. Leppo, E. Marbán, and P. M. L. Janssen. Physiological determinants of contractile force generation and calcium handling in mouse myocardium. *Journal of Molecular and Cellular Cardiology*, 34(10):1367–1376, October 2002.

L. B. Stull, N. Hiranandani, M. A. Kelley, M. K. Leppo, E. Marbán, and P. M. L. Janssen. Murine strain differences in contractile function are temperature- and frequency-dependent. *Pflügers Archiv - European Journal of Physiology*, 452(2):140–145, January 2006.

B. D. Stuyvers, A. D. McCulloch, J. Guo, H. J. Duff, and H. E. D. J. ter Keurs. Effect of stimulation rate, sarcomere length and Ca^{2+} on force generation by mouse cardiac muscle. *The Journal of Physiology*, 544(3):817–830, November 2002.

Y.-B. Sun and M. Irving. The molecular basis of the steep force-calcium relation in heart muscle. *Journal of Molecular and Cellular Cardiology*, 48(5):859–865, May 2010.

Y. Sun, F. Lou, and M. Irving. Calcium- and myosin-dependent changes in troponin structure during activation of heart muscle. *The Journal of Physiology*, 587(1):155–163, January 2009.

F. Swift, C. Franzini-Armstrong, L. Øyehaug, U. H. Enger, K. B. Andersson, G. Christensen, O. M. Sejersted, and W. E. Louch. Extreme sarcoplasmic reticulum volume loss and compensatory T-tubule remodeling after Serca2 knockout. *Proceedings of the National Academy of Sciences*, February 2012.

M. Takano, T. P. Terada, and M. Sasai. Unidirectional Brownian motion observed in an in silico single molecule experiment of an actomyosin motor. *Proceedings of the National Academy of Sciences of the United States of America*, 107(17):7769–7774, 2010.

H. S. Tamaddon, D. Vaidya, A. M. Simon, D. L. Paul, J. Jalife, and G. E. Morley. High-resolution optical mapping of the right bundle branch in connexin40 knockout mice reveals slow conduction in the specialized conduction system. *Circulation Research*, 87 (10):929 –936, November 2000.

K. H. W. J. ten Tusscher and A. V. Panfilov. Alternans and spiral breakup in a human ventricular tissue model. *American Journal of Physiology - Heart and Circulatory Physiology*, 291(3):H1088, 2006.

K. H. W. J. ten Tusscher, D. Noble, P. J. Noble, and A. V. Panfilov. A model for human ventricular tissue. *American Journal of Physiology - Heart and Circulatory Physiology*, 286(4):H1573, 2004.

T. Terui, M. Sodnomtseren, D. Matsuba, J. Udaka, S. Ishiwata, I. Ohtsuki, S. Kurihara, and N. Fukuda. Troponin and titin coordinately regulate length-dependent activation in skinned porcine ventricular muscle. *The Journal of General Physiology*, 131(3):275 –283, March 2008.

L. S. Tobacman. Cooperative binding of tropomyosin to actin. *Advances in Experimental Medicine and Biology*, 644:85–94, 2008.

L. S. Tobacman and D. Sawyer. Calcium binds cooperatively to the regulatory sites of the cardiac thin filament. *Journal of Biological Chemistry*, 265(2):931 –939, January 1990.

K. Tøndel, U. G. Indahl, A. B. Gjuvsland, J. O. Vik, P. Hunter, S. W. Omholt, and H. Martens. Hierarchical cluster-based partial least squares regression (HC-PLSR) is an efficient tool for metamodelling of nonlinear dynamic models. *BMC Systems Biology*, 5 (1):90, June 2011.

K. Tøndel, U. G. Indahl, A. B. Gjuvsland, S. W. Omholt, and H. Martens. Multi-way metamodelling facilitates insight into the complex input-output maps of nonlinear dynamic models. *BMC Systems Biology*, 6(1):88, July 2012.

G. P. Toorop, N. Westerhof, and G. Elzinga. Beat-to-beat estimation of peripheral resistance and arterial compliance during pressure transients. *American Journal of Physiology - Heart and Circulatory Physiology*, 252(6):H1275 –H1283, June 1987.

J. Tranquillo and A. Sunkara. Can we trust the transgenic mouse? Insights from computer simulations. In F. B. Sachse and G. Seemann, editors, *Functional Imaging and Modeling of the Heart*, number 4466 in Lecture Notes in Computer Science, pages 210–219. Springer Berlin Heidelberg, January 2007. ISBN 978-3-540-72906-8, 978-3-540-72907-5.

N. A. Trayanova, J. Constantino, and V. Gurev. Electromechanical models of the ventricles. *American Journal of Physiology - Heart and Circulatory Physiology*, May 2011.

T. P. Usyk and A. D. McCulloch. Electromechanical model of cardiac resynchronization in the dilated failing heart with left bundle branch block. *Journal of Electrocardiology*, 36:57–61, 2003a.

T. P. Usyk, R. Mazhari, and A. D. McCulloch. Effect of laminar orthotropic myofiber architecture on regional stress and strain in the canine left ventricle. *Journal of Elasticity*, 61(1):143–164, 2000.

T. P. Usyk, I. J. LeGrice, and A. D. McCulloch. Computational model of three-dimensional cardiac electromechanics. *Computing and Visualization in Science*, 4(4):249–257, 2002.

T. P. Usyk and A. D. McCulloch. Relationship between regional shortening and asynchronous electrical activation in a three-dimensional model of ventricular electromechanics. *Journal of Cardiovascular Electrophysiology*, 14:S196–S202, 2003b.

L. A. Venetucci, A. W. Trafford, and D. A. Eisner. Increasing ryanodine receptor open probability alone does not produce arrhythmogenic calcium waves threshold sarcoplasmic reticulum calcium content is required. *Circulation Research*, 100(1):105–111, May 2007.

J. O. Vik, A. B. Gjuvsland, L. Li, K. Tøndel, S. Niederer, N. P. Smith, P. J. Hunter, and S. W. Omholt. Genotype-phenotype map characteristics of an in silico heart cell. *Frontiers in Physiology*, 2:106, 2011.

S. T. Wall, J. M. Guccione, M. B. Ratcliffe, and J. S. Sundnes. Electromechanical feedback with reduced cellular connectivity alters electrical activity in an infarct injured left ventricle: a finite element model study. *American Journal of Physiology. Heart and Circulatory Physiology*, 302(1):H206–214, January 2012.

R. A. Walsh. The hierarchical approach to analysis of cardiovascular function in mice: An overview. In B. D. Hoit and R. A. Walsh, editors, *Cardiovascular Physiology in the Genetically Engineered Mouse*, number 238 in Developments in Cardiovascular Medicine, pages 1–16. Springer US, January 2001. ISBN 978-0-7923-7536-4, 978-1-4615-1653-8.

V. Y. Wang, H. I. Lam, D. B. Ennis, B. R. Cowan, A. A. Young, and M. P. Nash. Modelling passive diastolic mechanics with quantitative MRI of cardiac structure and function. *Medical Image Analysis*, 2009.

H. Watanabe, S. Sugiura, H. Kafuku, and T. Hisada. Multiphysics simulation of left ventricular filling dynamics using fluid-structure interaction finite element method. *Biophysical Journal*, 87(3):2074–2085, 2004.

H. Watanabe, S. Sugiura, and T. Hisada. The looped heart does not save energy by maintaining the momentum of blood flowing in the ventricle. *American Journal of Physiology - Heart and Circulatory Physiology*, 294(5):H2191–2196, May 2008.

R. H. Waterston, K. Lindblad-Toh, E. Birney, J. Rogers, J. F. Abril, P. Agarwal, R. Agarwala, R. Ainscough, M. Alexandersson, P. An, S. E. Antonarakis, J. Attwood, R. Baertsch, J. Bailey, K. Barlow, S. Beck, E. Berry, B. Birren, T. Bloom, P. Bork, M. Botcherby, N. Bray, M. R. Brent, D. G. Brown, S. D. Brown, C. Bult, J. Burton, J. Butler, R. D. Campbell, P. Carninci, S. Cawley, F. Chiaromonte, A. T. Chinwalla, D. M. Church, M. Clamp, C. Clee, F. S. Collins, L. L. Cook, R. R. Copley, A. Coulson, O. Couronne, J. Cuff, V. Curwen, T. Cutts, M. Daly, R. David, J. Davies, K. D. Delehaunty, J. Deri, E. T. Dermitzakis, C. Dewey, N. J. Dickens, M. Diekhans, S. Dodge, I. Dubchak, D. M. Dunn, S. R. Eddy, L. Elnitski, R. D. Emes, P. Eswara, E. Eyras, A. Felsenfeld, G. A. Fewell, P. Flicek, K. Foley, W. N. Frankel, L. A. Fulton, R. S. Fulton, T. S. Furey, D. Gage, R. A. Gibbs, G. Glusman, S. Gnerre, N. Goldman, L. Goodstadt, D. Grafham, T. A. Graves, E. D. Green, S. Gregory, R. Guigó, M. Guyer, R. C. Hardison, D. Haussler, Y. Hayashizaki, L. W. Hillier, A. Hinrichs, W. Hlavina, T. Holzer, F. Hsu, A. Hua, T. Hubbard, A. Hunt, I. Jackson, D. B. Jaffe, L. S. Johnson, M. Jones, T. A. Jones, A. Joy, M. Kamal, E. K. Karlsson, D. Karolchik, A. Kasprzyk, J. Kawai, E. Keibler, C. Kells, W. J. Kent, A. Kirby, D. L. Kolbe, I. Korf, R. S. Kucherlapati, E. J. Kulbokas, D. Kulp, T. Landers, J. P. Leger, S. Leonard, I. Letunic, R. Levine, J. Li, M. Li, C. Lloyd, S. Lucas, B. Ma, D. R. Maglott, E. R. Mardis, L. Matthews, E. Mauceli, J. H. Mayer, M. McCarthy, W. R. McCombie, S. McLaren, K. McLay, J. D. McPherson, J. Meldrim, B. Meredith, J. P. Mesirov, W. Miller, T. L. Miner, E. Mongin, K. T. Montgomery, M. Morgan, R. Mott, J. C. Mullikin, D. M. Muzny, W. E. Nash, J. O. Nelson, M. N. Nhan, R. Nicol, Z. Ning, C. Nusbaum, M. J. O'Connor, Y. Okazaki, K. Oliver, E. Overton-Larty, L. Pachter, G. Parra, K. H. Pepin, J. Peterson, P. Pevzner, R. Plumb, C. S. Pohl, A. Poliakov, T. C. Ponce, C. P. Ponting, S. Potter, M. Quail, A. Reymond, B. A. Roe, K. M. Roskin, E. M. Rubin, A. G. Rust, R. Santos, V. Sapojnikov, B. Schultz, J. Schultz, M. S. Schwartz, S. Schwartz, C. Scott, S. Seaman, S. Searle, T. Sharpe, A. Sheridan, R. Shownkeen, S. Sims, J. B. Singer, G. Slater, A. Smit, D. R. Smith, B. Spencer, A. Stabenau, N. Stange-Thomann, C. Sugnet, M. Suyama, G. Tesler, J. Thompson, D. Torrents, E. Trevaskis, J. Tromp, C. Ucla, A. Ureta-Vidal, J. P. Vinson, A. C. Von Niederhausern, C. M. Wade, M. Wall, R. J. Weber, R. B. Weiss, M. C. Wendl, A. P. West, K. Wetterstrand, R. Wheeler, S. Whelan, J. Wierzbowski, D. Willey, S. Williams, R. K. Wilson, E. Winter, K. C. Worley, D. Wyman, S. Yang, S.-P. Yang, E. M. Zdobnov, M. C. Zody, and E. S. Lander. Initial sequencing and comparative analysis of the mouse genome. *Nature*, 420 (6915):520–562, December 2002.

J. Weiss. The Hill equation revisited: Uses and misuses. *FASEB Journal*, 11(11):835–841, 1997.

N. Westerhof and G. Elzinga. Normalized input impedance and arterial decay time over heart period are independent of animal size. *American Journal of Physiology - Regulatory, Integrative and Comparative Physiology*, 261(1):R126–133, July 1991.

J. P. Whiteley. An efficient technique for the numerical solution of the bidomain equations. *Annals of Biomedical Engineering*, 36(8):1398–1408, 2008.

J. P. Whiteley, M. J. Bishop, and D. J. Gavaghan. Soft tissue modelling of cardiac fibres for use in coupled mechano-electric simulations. *Bulletin of Mathematical Biology*, 69 (7):2199–2225, 2007.

K. C. L. Wong, L. Wang, H. Zhang, H. Liu, and P. Shi. Meshfree implementation of individualized active cardiac dynamics. *Computerized Medical Imaging and Graphics*, 34(1):91–103, January 2010.

J. Xi, P. Lamata, W. Shi, S. Niederer, S. Land, D. Rueckert, S. Duckett, A. Shetty, C. Rinaldi, R. Razavi, et al. An automatic data assimilation framework for patient-specific myocardial mechanical parameter estimation. *Functional Imaging and Modeling of the Heart*, pages 392–400, 2011.

J. Xi, P. Lamata, S. Niederer, S. Land, W. Shi, X. Zhuang, S. Ourselin, S. Duckett, and A. Shetty. The estimation of patient-specific cardiac diastolic functions from clinical measurements. *Medical Image Analysis*, 2012.

M. Yadid and A. Landesberg. Stretch increases the force by decreasing cross-bridge weakening rate in the rat cardiac trabeculae. *Journal of Molecular and Cellular Cardiology*, 49(6):962–971, 2010.

T. Yanagida, K. Kitamura, H. Tanaka, A. Hikikoshi Iwane, and S. Esaki. Single molecule analysis of the actomyosin motor. *Current Opinion in Cell Biology*, 12(1):20–25, February 2000.

D. T. Yue, E. Marban, and W. G. Wier. Relationship between force and intracellular [Ca^{2+}] in tetanized mammalian heart muscle. *Journal of General Physiology*, 87(2):223, 1986.

Y. Zhang, C. Riesterer, A. M. Ayrall, F. Sablitzky, T. D. Littlewood, and M. Reth. Inducible site-directed recombination in mouse embryonic stem cells. *Nucleic Acids Research*, 24(4):543–548, February 1996.